FAR-INFRARED ABSORPTION

IN InSb

FAR-INFRARED ABSORPTION IN InSb

by

EMIL STEVE KOTELES, M.Sc.

A Thesis

Submitted to the Faculty of Graduate Studies

in Partial Fulfilment of the Requirements

for the Degree

Doctor of Philosophy

McMaster University

March, 1973

DOCTOR OF PHILOSOPHY
(Physics)

McMASTER UNIVERSITY
Hamilton, Ontario.

TITLE: Far-infrared absorption in InSb

AUTHOR: Emil Steve Koteles, B.Sc. (Assumption University)
M.Sc. (University of Windsor)

SUPERVISOR: Dr. W. R. Datars

NUMBER OF PAGES: xii, 151

SCOPE AND CONTENTS:

Far-infrared absorption in the semiconductor InSb was studied with a high resolution Fourier transform spectrometer. The effective mass of the electron in the conduction band was determined, using cyclotron resonance techniques, as a function of magnetic field and temperature and compared with the theory of E. O. Kane (1957). Resonant polaron coupling effects were also observed and an accurate value of the electron-LO phonon coupling constant derived.

Far-infrared absorption attributable to single and two-phonon processes was studied under high resolution conditions and as a function of temperature. Two-phonon absorption was compared with two-phonon density of states curves calculated employing parameters derived from inelastic neutron scattering experiments. Combination phonon modes and their location in the Brillouin zone which give rise to strong features in the two-phonon density of states curves were identified. The shift of phonon frequencies as a function of temperature was analyzed as the sum of a quasi-harmonic lattice dilation term and an anharmonic term.

ABSTRACT

A high-resolution, low-noise far-infrared Fourier transform spectrometer system has been developed and utilized to study optical absorption in the III-V compound semiconductor InSb.

Its electron effective mass was investigated, using cyclotron resonance absorption, as a function of magnetic field and compared with a theory originated by Kane (1957). The agreement was good and accurate values of the band edge effective mass and effective g factors were determined. Resonant electron-LO phonon coupling between the $n = 2$ and $n = 0 + \omega_{LO}$ Landau levels was observed and the polaron effective mass enhancement measured as a function of magnetic field. Comparison with Larsen's theory (1966), permitted an accurate value of the coupling constant to be derived. The temperature dependence of the electron effective mass was shown to be primarily due to dilation of the crystal lattice in confirmation of other workers' suggestions. However, some discrepancy, whose origin is unknown, was found to exist between experiment and theory.

Single phonon absorption by the longitudinal optic phonon mode at the zone center was observed on the side of the main Reststrahl band in a thin sample. The shapes, frequencies and intensities of far-infrared absorptions attributable to two-phonon processes were found to compare favourably with a theoretical two-phonon density of states curve calcu-

lated by G. Dolling (1972). The parameters used in the theory were derived from inelastic neutron scattering experiments. Two-phonon combinations and their locations in the Brillouin zone which give rise to strong features in the two-phonon density of states were identified by comparing theory and experiment. Important critical points were discovered to be located on or near the zone boundary and not only at the symmetry points X and L as previously suggested. The frequency shifts of some two-phonon features were measured as a function of temperature and analyzed in terms of a quasi-harmonic lattice dilation component and an anharmonic component. The two terms were found to be mirror images as a function of temperature.

ACKNOWLEDGEMENTS

I should like to thank my supervisor, Dr. W. R. Datars for his advise and assistance, especially during the writing of this thesis. Many others have aided me in this work. In particular I should like to thank Dr. G. Dolling for his generosity in providing the two-phonon density of states calculation and Dr. T. Timusk for his suggestions on the interpretation of the phonon absorption results. I should also like to acknowledge useful co-operation in instrumentation techniques with Dr. Timusk's far-infrared spectroscopy group. Mr. Rob Douglas was instrumental in the development of the spectrometer system and Mr. W. Scott provided a more than adequate supply of liquid helium. Mr. Clarence Verge provided excellent technical assistance in the design and construction of most of the electronics for the interferometer and its data acquisition system. I should also like to thank Mrs. H. Kennelly for her swift and accurate typing of this thesis. Finally I must acknowledge the assistance and love of my wife, Betty, through these long years.

This research was supported through grants from the National Research Council of Canada. Personal financial support from the Government of the Province of Ontario and McMaster University is gratefully acknowledged.

TABLE OF CONTENTS

LIST OF FIGURES

LIST OF TABLES

CHAPTER I

INTRODUCTION

Most of the fundamental physical properties of solids result from processes involving lattice modes of vibration and the motion of electrons. In semiconductors, far-infrared optical absorption offers an opportunity to investigate these particles individually and the interactions between them with high accuracy.

Recent advances in far-infrared technology have made this energy starved region of the electro-magnetic spectrum readily accessible to experimentation. The far-infrared interferometer, the Fast Fourier Transform (FFT) algorithm, high-speed and high-capacity computers and high-sensitivity detectors have combined to make this progress possible. A detailed account of the design, theory and operation of the Fourier transform spectrometer employed in these experiments is given in Chapter II along with information about the peripheral equipment.

Resonant absorption of electro-magnetic radiation by charge carriers in the presence of a D.C. magnetic field is termed cyclotron resonance. It is the most direct and accurate method of determining the effective mass of carriers

which gives information concerning the electronic energy band structure in semiconductors. Microwave frequencies have been employed in these studies but, since the cyclotron resonance absorption linewidth is inversely related to the frequency, it is advantageous to increase the frequency as much as possible. The reduction in linewidths resulting from operation in the far-infrared region of the electro-magnetic spectrum makes possible the resolution of fine structure connected with energy band anisotropy and non-parabolicity. Higher frequencies necessitate larger magnetic fields. However the required field is proportional to the charge carrier effective mass so that materials with small effective masses are more amenable to study. Indium antimonide (InSb) possesses one of the smallest electron effective masses of any compound semiconductor and has the added advantage of being readily available in pure, single-crystal form. Furthermore, extensive experimental and theoretical studies on its electronic energy bands have been performed in recent years. The high precision possible with Fourier transform spectrosopy permits a more detailed investigation of theory.

According to first order theory, the effect of electron-phonon interactions on the effective mass of charge carriers in semiconductors is expected to be negligible. Only changes in the static lattice, such as those induced by temperature or pressure, will modulate the magnitude of the

effective mass. A study of the temperature dependence of the electron effective mass in InSb verifies this assumption although a slight discrepancy between experiment and theory does exist. The theory, results and a discussion of this investigation are given in Chapter III.

For the case of polar semiconductors such as InSb, a particular type of interaction between individual charge carriers and longitudinal optical (LO) phonons at the center of the Brillouin zone is possible. Generally this results in a small, constant polaron correction to the effective mass. Under certain conditions however, such as occur when the cyclotron frequency and the LO phonon frequency are equal, a resonant coupling takes place which produces a large, frequency dependent change in the effective mass. Such a resonant coupling was observed in InSb with enough precision that its small electron-LO phonon coupling constant could be determined with accuracy. The theory and results of this resonant electron-LO phonon coupling are detailed in Chapter III.

Frequencies of the lattice modes of vibration (phonons) of most solids are such that they occur in the far-infrared region of the spectrum. In particular, the phonon energies of InSb are small enough so that all two-phonon absorption processes fall conveniently within the range of the far-infrared spectrometer employed here. High resolution two-

phonon absorption spectroscopy permits identification of locations on the dispersion curves in the Brillouin zone which contribute significantly to the phonon density of states. This provides information about the nature of interatomic forces. The high resolution possible with Fourier transform spectroscopy also enables temperature dependent energy shifts of phonons to be measured with accuracy. Such changes in phonon energy are related to fundamental processes involving the anharmonicity of the lattice potential. The identification of all the major features of the two-phonon absorption spectra with combination phonon modes at certain points in the Brillouin zone is outlined in Chapter IV. This is accomplished with the aid of a calculated two-phonon density of states curve obtained employing parameters derived from inelastic neutron scattering experiments. The temperature dependence of some of the features of the spectra is also discussed.

Chapter V contains a summary of the results and conclusions.

CHAPTER II

INSTRUMENTATION

A - FAR-INFRARED INTERFEROMETER

i Introduction

Interferometry has had a long and relatively uneventful history until recently. Loewenstein (1966) has presented an interesting review of the early history of this subject. In simplified terms, interferometry is a method of deducing the electromagnetic spectra of a source by analyzing the interference of two coherent beams from the source. An interferogram,which is in reality a Fourier transform of the spectrum, is the result when the intensities are measured as a function of the difference in optical path between the two beams. Fizeau (1862) was the first to put this technique to practical application when he used Newton's rings to show that yellow sodium light was a doublet.

Michelson (1891), whose interest lay in precision measurements, invented the interferometer that bears his name in order to define the meter in terms of the wavelength of light and to perform the series of ether drift experiments that laid the experimental foundation for the special theory of relativity. In his work, although he lacked the sophisticated computers and data acquisition systems of to-day, he performed

crude Fourier transforms of his visibility curves. Later, in 1911, Rubens and Wood published the first true interferogram which was of the infrared radiation emitted by a Welsbach mantle.

In general, interferometry remained a specialized tool for high resolution work until approximately twenty years ago when the two dominent advantages of interferometry over classical spectroscopy were discovered. It was Jacquinot and Dufour (1948) who pointed out that, unlike the case of a dispersive instrument, it is not necessary, in an interferometer, to limit the aperture to work at high resolutions. At some given resolution then, the energy throughout the interferometer is greater than that of a dispersive monochromator which, in effect, reduces the time required for a spectrum with a given signal-to-noise ratio. A few years later Fellgett (1951) showed the advantages of the multiplex principle which the interferometer employs. Unlike classical monochromators which record information from each resolution element in a spectral band sequentially, the detector of an interferometer has incident upon it radiation from all spectral elements simultaneously. The multiplex principle is a real advantage only if the noise is detector limited. It is evident then that both the multiplex and throughput advantages have their greatest impact in energy starved regions of the spectrum such as the far infrared. With the addition, in recent years, of low-noise, high-sensitivity detectors, high-capacity,

high-speed computers and Fourier-transform algorithms, a veritable explosion in the number of studies and uses of interferometers has taken place.

The Fourier spectrometer used in these experiments is a commercial instrument, FS-720, built by Research and Industrial Instruments Company of England. It is essentially similar to a Michelson interferometer with the notable difference being the size of the optical components. The mirrors and beamsplitter are three inches in diameter so that they may function more efficiently in the far infrared region of the spectrum.

A schematic diagram of the optical system is given in Figure 2.1. Energy from the source, S, a high pressure mercury lamp, is collimated by an off-axis parabolic mirror, M_1, which directs the radiation to a beamsplitter, B. Ideally this beamsplitter divides the light into two beams with the same amplitude, sending one beam to a moving mirror, M_m, and the other to a fixed mirror, M_s. The light is reflected from these mirrors and recombines at the beamsplitter where half of the energy returns toward the source and is lost while the other half exits toward the condensing mirrors, M_2 and M_3, and the sample assembly. The recombination is either constructive or destructive depending upon the wavelength of light and the optical path difference between the two beams. Since the beamsplitter is an unsupported single-layer dielec-

Figure 2.1: Top view of the optical system of the far-infrared Fourier transform spectrometer. The chopper blade is pictured in a horizontal position.

S - Source

C - Chopper blade

B - beamsplitter

M_1 - collimating mirror

M_m - moving mirror

M_s - stationary mirror

M_2 and M_3 - condensing mirrors.

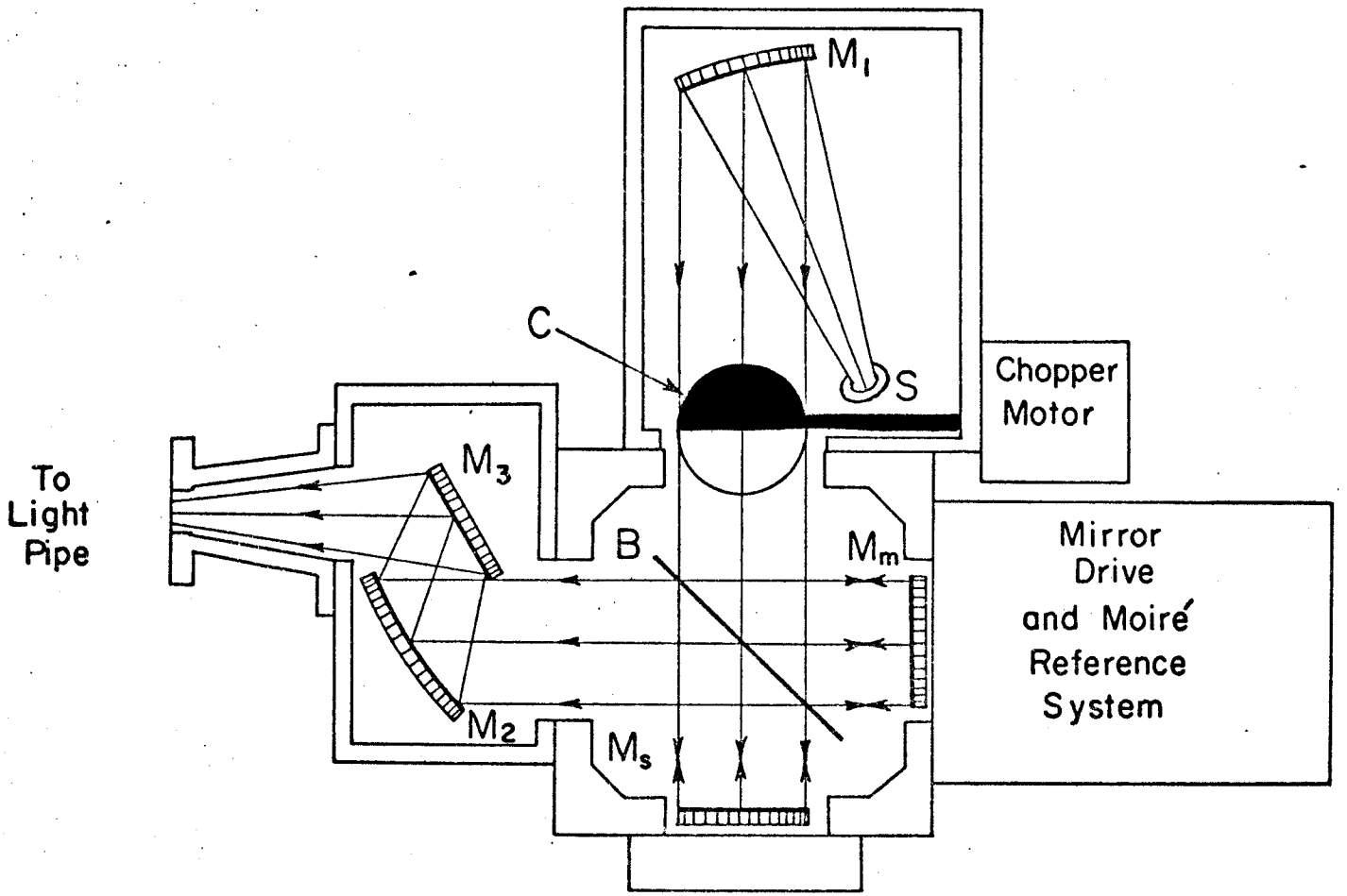

10 cm

TOP VIEW

tric film (Mylar) it is completely symmetric and so no compensating plate is required.

ii - Theory

The interferogram of a monochromatic source (ie. assuming a delta function in the frequency domain, Figure 2.2a) is simply a cosine function extending from plus to minus infinity in path difference. This is illustrated in Figure 2.2b. The intensity as a function of path difference, x, is given by

$$I(x) = S_o(1 + \cos 2\pi\omega x) \qquad (2.1)$$

where S_o is the intensity of the monochromatic light and ω is the frequency measured in units of reciprocal length (cm^{-1}).

An arbitrary spectral input (Figure 2.2c) can be pictured as consisting of a series of delta functions, each contributing a cosine wave of different wavelength to the interferogram. Only at one path difference (x=0) are all the constituent cosine waves simultaneously in constructive interference. At path differences other than zero, the different components combine to construct the interferogram shown in Figure 2.2d. Mathematically, for an arbitrary spectral input, $S(\omega)$,

$$I(x) = \int_o^\infty S(\omega)[1 + \cos 2\pi\omega x]d\omega$$

$$= \frac{1}{2} I(o) + \int_o^\infty S(\omega)\cos 2\pi\omega x d\omega \qquad (2.2)$$

Figure 2.2a: Delta Function Spectrum

Figure 2.2b: Interferogram of a Delta Function Spectrum

Figure 2.2c: Broadband Spectrum

Figure 2.2d: Interferogram of a Broadband Spectrum

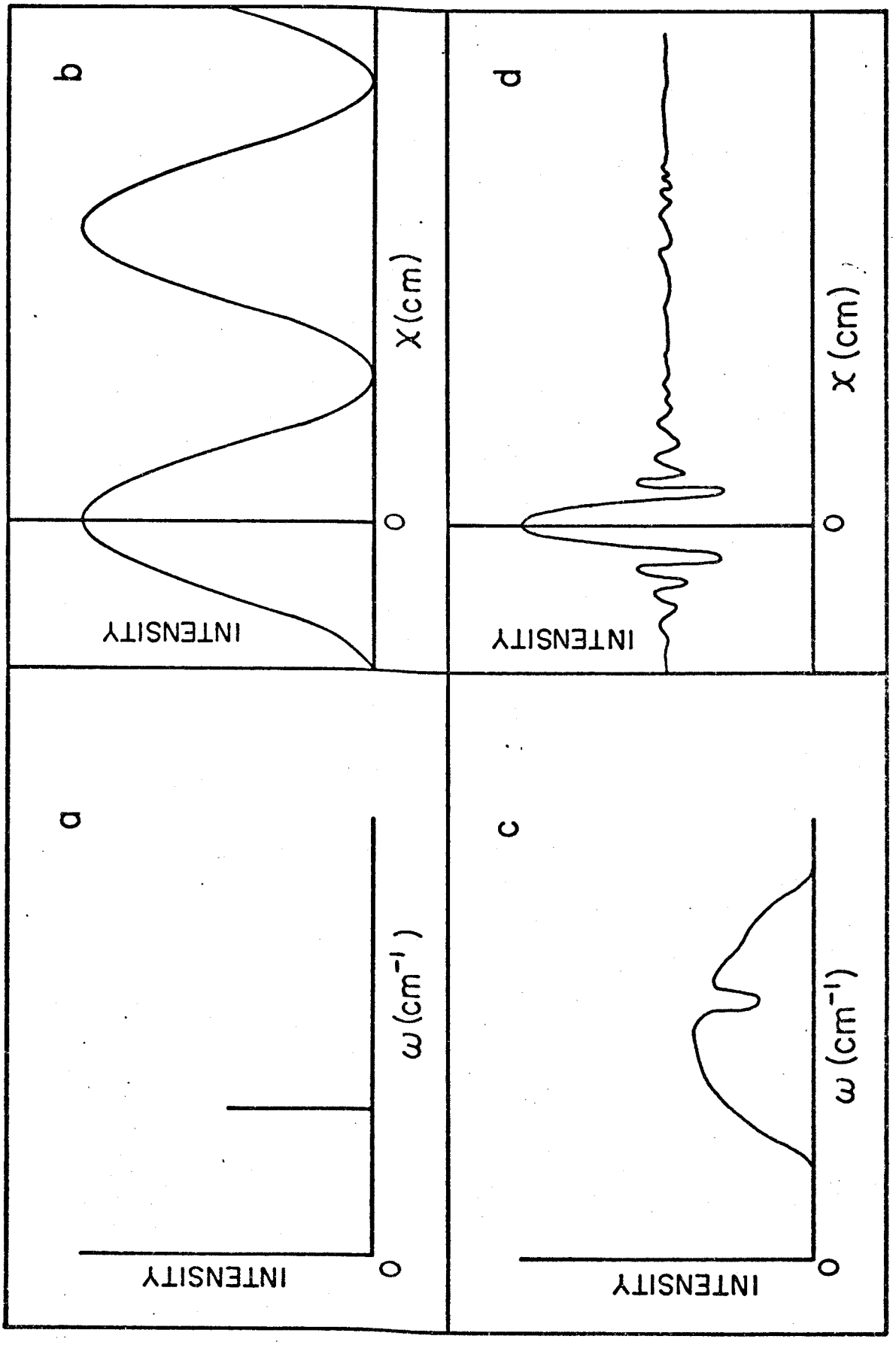
b
INTENSITY
0
x(cm)
d
INTENSITY
0
x (cm)
a
INTENSITY
0
ω (cm⁻¹)
c
INTENSITY
0
ω (cm⁻¹)

where I(o) is the intensity at zero path difference. Application of the Fourier integral theorem for the even function I(x) results in the desired spectrum,

$$S(\omega) = 4 \int_{o}^{\infty} [I(x) - \frac{1}{2} I(o)] \cos 2\pi\omega x dx \qquad (2.3)$$

in terms of the measured quantity I(x). This is the fundamental relation of Fourier transform spectroscopy. The interferogram is measured as a function of path difference and the spectrum is computed using equation (2.3) by analog or digital means. I(o) is easily obtained from measurements of the interferogram far removed from zero path difference where, in practice, oscillations in intensity are small.

Complications arise, however, from the fact that no interferogram is measured to infinite path difference and, if digital means are used for the transformation as is usually the case, the interferogram is sampled only at a finite number of points. In the first case, the truncation of I(x) at some maximum path difference, x_{max}, limits the resolution of the computed spectrum. The effect of this abrupt cut-off may be studied by substituting equation (2.2) into the truncated integral (2.3) to obtain the approximate spectrum, $S_c(\omega)$.

$$S_c(\omega) = 4 \int_{o}^{x_{max}} [\int_{o}^{\infty} S(\omega') \cos 2\pi\omega' x d\omega'] \cos 2\pi\omega x dx \; . \qquad (2.4)$$

Integrating over x gives

$$S_c(\omega) = \int_{o}^{\infty} S(\omega') R(\omega, \omega', x_{max}) d\omega' \qquad (2.5)$$

where

$$R = \left[\frac{\sin 2\pi(\omega-\omega')x_{max}}{2\pi(\omega-\omega')x_{max}} + \frac{\sin 2\pi(\omega+\omega')x_{max}}{2\pi(\omega+\omega')x_{max}}\right] 2x_{max} \qquad (2.6)$$

is the scanning or instrumental function. This is analogous to the slit function of classical spectrometers. It is simply the spectrum produced when the input is a delta function. The computed spectrum, $S_c(\omega)$, is thus the convolution of the actual spectrum, $S(\omega')$, with the instrumental function, R. If $\omega' >> 1/x_{max}$, then R reduces to

$$R = 2x_{max}\,\mathrm{sinc}[2\pi(\omega-\omega')x_{max}] \qquad (2.7)$$

where

$$\mathrm{sinc}[2\pi(\omega-\omega')x_{max}] = \frac{\sin[2\pi(\omega-\omega')x_{max}]}{2\pi(\omega-\omega')x_{max}} . \qquad (2.8)$$

This function has a width at half height of $\delta\omega \simeq 0.7/x_{max}$, so that the smallest frequency interval resolved is approximately the reciprocal of x_{max}. Also, the criterion that $\omega' >> 1/x_{max}$ is valid if the resolving power $\omega/\delta\omega$ is large in the region of interest.

Not only does the abrupt cut-off of x broaden the delta function but large sideband oscillations are generated which can cause serious problems if the spectrum being studied contains sharp lines. The size of these oscillations may be reduced by introducing a smooth cut-off function A(x) into the truncated integral, so that

$$S_c(\omega) = 4\int_0^{x_{max}} [I(x) - \tfrac{1}{2} I(o)]A(x)\cos 2\pi\omega x\, dx \qquad (2.9)$$

The undesirable side effectof this process, called apodization (Jacquinot and Roizen Dossier, 1964),is to widen the instrumental function half width. Any function which varies smoothly to a value of zero at $x = x_{max}$ from a value of unity at x=0 can be used although the two apodizing functions commonly in use are

$$A(x) = 1 - \frac{x}{x_{max}} \qquad |x| \leq x_{max} \qquad (2.10)$$

$$A(x) = [1 - (\frac{x}{x_{max}})^2]^2 \qquad |x| \leq x_{max} \qquad (2.11)$$

which have corresponding instrumental functions of

$$R = x_{max}\ \mathrm{sinc}^2[\pi(\omega-\omega')x_{max}] \qquad (2.12)$$

$$R = 1.066\ x_{max}[2\pi(\omega-\omega')x_{max}]^{-5/2}J_{5/2}(2\pi(\omega-\omega)x_{max}) \qquad (2.13)$$

$J_{5/2}(2\pi(\omega-\omega')x_{max})$ is a Bessel function. The second apodizing function dampens the secondary oscillations slightly better than the first but, in these experiments, since few sharp spectral features were studied, the triangular apodization function (equation (2.10)) was used for the sake of simplicity. The instrumental function then has the Rayleigh form and so Rayleigh's criterion for resolution may be used to state that two spectral lines separated by the frequenty interval $\delta\omega = 1/x_{max}$ are resolved. It should also be mentioned that since the apodizing function weights the interferogram more strongly near zero path difference, where the signal to noise ratio is largest, than near the maximum path difference, where the signal to noise is poorest, the signal to noise ratio

on the spectrum is improved when apodization is performed.

The second complication introduced by the consideration of practical interferograms occurs because of the necessity of sampling the interferogram at a finite number of points equally spaced in path difference. "Ghosts" may be introduced into the spectrum if there are systematic errors in path difference increments. Random errors produce scattered ripples (Connes and Connes,1966). Furthermore, the sampling theorem of information theory (Goldman, 1953) states that in order to retrieve all of the information in the spectrum from $0 < \omega < \omega_{max}$, it is necessary to sample I(x) at intervals of $\Delta x = 1/2\omega_{max}$ or smaller. As Richards (1964) points out, the computed spectrum at frequency ω, will contain extra energy of frequencies $2n\omega_{max} - \omega$ and $2(n-1)\omega_{max} + \omega$ where $n = 1,2,3,\ldots$. The consequence of periodic sampling is a one dimensional analog of the reduced zone scheme in the Brillouin zone theory of solids. That is, spectral intensities at frequencies $\omega > \omega_{max}$ are folded back onto the region $0 < \omega < \omega_{max}$. Thus, in order to obtain an unambiguous spectrum, it is necessary to use filters to reduce the spectral intensities to zero at ω_{max} and all higher frequencies. This is not too difficult to accomplish in practice and it does not compete in seriousness with the phase error problem which also arises from digital sampling.

Equation (2.3) was derived under the assumption that I(x) was an even function of x, thus permitting the use of a

cosine Fourier transform to produce the spectrum. If, however, one of the experimental samples does not occur precisely at zero path difference, the interferogram

$$I(x) = \frac{1}{2} I(\varepsilon) + \int_0^\infty S(\omega)\cos 2\pi\omega(x-\varepsilon)d \qquad (2.14)$$

where ε is the error in the zero path difference point, is no longer an even function of x. The resulting instrumental function will be asymmetric and its convolution with the true spectrum may even cause the computed spectrum to become negative at higher frequencies. Even a small zero path difference error can lead to serious distortions of the spectrum, if "one-sided" interferograms are used (x extends from zero to x_{max}). The most successful method of dealing with this problem involves the use of phase spectra (Forman et al, 1966; Mertz, 1967) to correct the measured data. More detail on this procedure will be given later.

Finally, the effect of the finite aperture of the optical system on the resolving power must be considered. Jacquinot (1960) has shown, for collimated light and circular apertures, that if the limiting aperture subtends a solid angle $\Omega = \pi\theta^2$ at a collimating mirror, an extremal off-axis ray through the interferometer has a path difference $1/\cos\theta \simeq 1 + \Omega/2\pi$ times that of an axial ray. The spread in values $\delta x/x$ of the path differences corresponds to a spread in frequency of $\delta\omega/\omega = \delta x/x = \Omega/2\pi$, thus limiting the resolving power to values less than $\omega/\delta\omega = 2\pi/\Omega$ or

$$\frac{\omega}{\delta\omega} = 8\left(\frac{f}{d}\right)^2 \qquad (2.15)$$

where d is the source diameter and f is the focal length of the collimating mirror. In this interferometer, $\omega/\delta\omega \simeq 10^3$ to 10^4. Furthermore, since the mean path difference for all rays passing through the interferometer is $1 + \Omega/4\pi$ times that of an axial ray, the frequencies of all spectral elements are overestimated by this factor if the axial path difference is used in the computation of the spectrum. Thus, for example, all the frequencies must be reduced by 5×10^{-4} if $\omega/\delta\omega \simeq 10^3$ as is generally the case.

iii - Instrument Optimization

a - Noise

The noise on an interferogram can be subdivided into two classes that are related to its origin; path difference errors and intensity errors.

1 - Path Difference Errors

The tacit assumption has been made that the interferogram is sampled at constant path difference increments, ie. at $0, \Delta x, 2\Delta x, 3\Delta x,$ etc. If this is not the case noise and distortions can be generated on the computed spectrum. Periodic errors in the magnitude of Δx produce "ghosts"; a slow progressive error reduces the resolving power; a random error produces scattered ripples (Connes and Connes, 1966).

The mirror drive in the present instrument consists of a synchronous motor which is coupled, via a gear box, to a

finely machined screw which, in turn, drives a carriage. The gear box permits the velocity of the carriage to be varied, in steps, from a nominal 0.5 microns per second to 500 microns per second. The moving mirror is mounted on this carriage which advances along a highly precise lapped cylinder. In spite of all these precautions there are indications of jitter and hesitation in the mirror movement. Fortunately, these errors in mirror displacement do not translate directly into errors in path difference as the displacement measuring system is not dependent, to first order, on smooth mirror movement. The reference system consists of two diffraction gratings, one mounted on the carriage and the other fixed to the interferometer base with a spacing of about 25 microns between them. White light from a small incandescent lamp forms Moiré interference fringes as it passes through the gratings and these fringes fall on a photocell. As the carriage moves, the 4 micron ruling of the Moiré gratings produces peaks in the photocell signal spaced 8 microns apart in path difference. This signal is fed through a differential operational amplifier (Philbrick P85AU) to a Schmidt trigger circuit. The pulse produced every 8 microns is used to command the data acquisition system to read and record an interferogram intensity. Since the minimum sampling interval is given by $\Delta x = 1/2\ \omega_{max}$, the upper permissible frequency limit for this sampling system is 625 cm^{-1} (77.49 meV, 18.74×10^{12} Hz or a wavelength of 16

microns). The maximum possible mirror movement is 5 cm (10 cm in path difference) and so the theoretical resolution is 0.1 cm^{-1}.

The absence of "ghosts" in the computed spectrum indicates the absence of systematic errors in the path difference reference system. The effect of random errors is much more difficult to isolate but noise definitely attributable to random path difference errors has not been found.

2 - Intensity Errors

Systematic intensity errors such as those introduced by non-linearities in the data acquisition system introduce zero level distortions in the spectrum and harmonic and cross-modulation terms in sharp line spectra. No evidence that this type of distortion is present in this system has been found.

Random intensity fluctuations due to source intensity, detector sensitivity or data acquisition system gain variations add noise to the interferogram and thus to the spectrum. The major component of this type of noise in this apparatus has been found to be the light source. The broadband source which emits the greatest intensity in the far infrared is the high pressure mercury lamp. A 125 watt Philips lamp (HPK 125W) was used in the early stages of these investigations and replaced later with a 200 watt Gates lamp (UA-2) which had better arc stability. In both cases the total far infrared power incident on the detector was of the order of 10^{-8} watts. The D.C. lamp

power was produced by a current regulated power supply which utilized a commercial A.C. ballast to supply the raw power which was then rectified and controlled. The output current passed through a low-resistance, low-temperature-coefficient resistor. The voltage developed across this element was monitored and used to supply a feedback signal which controlled the operation of a pass-bank. The current was stable to 1 part in 10^5 over an hour. However, controlling the current did not ensure power stabilization in the lamp since voltage fluctuations were still possible. Furthermore, the total spectral output from the lamp is the sum of contributions from the mercury plasma and the hot lamp envelope (Cano and Mattioli, 1967). Variation in the plasma arc position can generate serious intensity fluctuations on the interferogram. The fringing field from a small (2 kilo-oersteds) permanent magnet was used to lock the arc in a stable position. However the procedure was not always reproducible or reliable.

In an effort to reduce the effect of intensity fluctuation from the source, a novel double beam chopping system was devised (Douglas and Timusk,1970). An ordinary chopping system generates a square wave which is synchronously rectified with the aid of a reference signal (Figure 2.3a). This rectified signal is then integrated by an RC filter to produce a D.C. level proportional to the original signal amplitude. The chopped signal oscillates between a zero level (light completely blocked off) and a signal level (no blockage). In the new system

Figure 2.3a: Bolometer signal - single beam operation

Figure 2.3b: Bolometer signal - double beam operation. The reference and signal levels are pictured unbalanced for clarity.

Figure 2.3c: Bandwidth, resolution and noise in a spectrum.

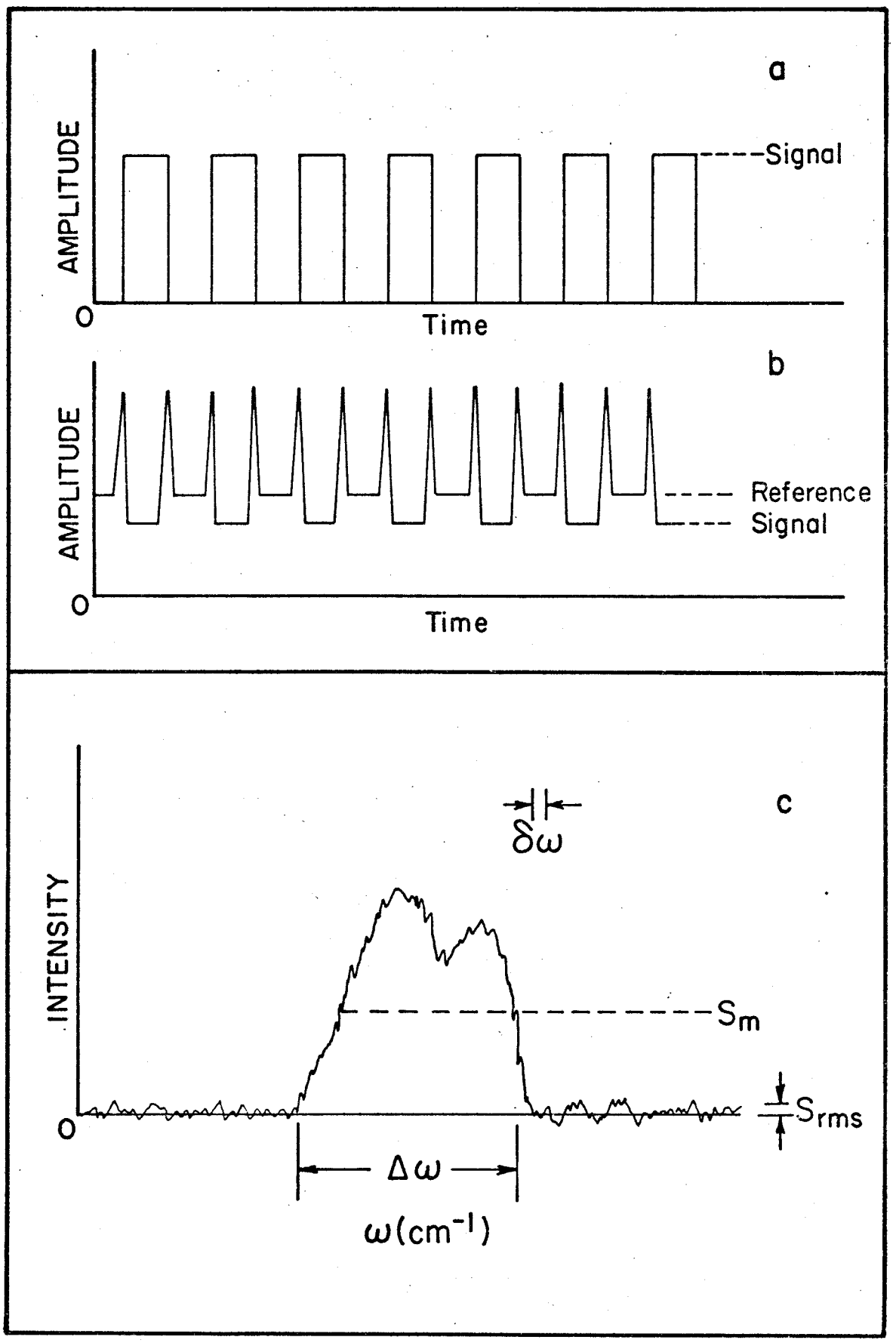
a
AMPLITUDE
Signal
0
Time
b
AMPLITUDE
Reference
Signal
0
Time
c
δω
INTENSITY
Sm
Srms
0
Δω
ω(cm⁻¹)

The signal oscillates between a signal and a lamp reference level (Figure 2.3b). The lamp reference is provided by a fixed mirror mounted so that it covers one half of the moving mirror area. A half circle vane rotating horizontally in the beam between the collimating mirror of the source and the beamsplitter acts as a chopper. The half circle covers first the fixed mirror and then the moving mirror as it executes a half rotation. The detector alternatively receives energy from the moving mirror and the fixed mirror. Uniform intensity fluctuations in the source lead to equivalent changes in the signal and lamp reference levels which then cancel when the signal is rectified and integrated. Cancellation is maximized when the two levels are exactly balanced. Fluctuations in the D.C. output, which is proportional to the difference between the signal and lamp reference levels are thus reduced. The double beam system has the added advantage of eliminating any variations in the signal level that can be correlated with similar variations in the lamp reference level. For example, both levels are affected by changes in the detector sensitivity produced by bath temperature changes. Thus this chopping system tends to suppress long term sensitivity drifts in the bolometer, a problem common to a temperature sensitive detector. However, it has the disadvantage of reducing the throughput by half,and uncorrelated intensity fluctuations such as those produced by mercury arc movement, are not cancelled. Even though both beams are eventually incident on the same detector, their optical paths are not coincident. In fact, moving

the arc about with the stabilizing magnet can cause wide variation in the balance between the signal and lamp reference levels. Nevertheless, the difficulties of lamp intensity fluctuations should not be exaggerated. Using a combination of double beam chopping and magnet stabilization it was usually possible to reduce the lamp noise to a level comparable to the detector noise for periods of time longer than an interferogram scan time.

Another very important factor in the achievement of a high performance system is a low-noise detector. The details of the fabrication and the method of operation of the bolometer used will be discussed later but it is relevant to give an indication of its performance now. Operating at about 2°K, the sensitivity of this detector was such that an absorbed electromagnetic flux of from 10^{-12} to 10^{-13} watts produced a signal equal to the noise level. The bolometer was not a major source of noise in the system. The same can be said of the data acquisition system.

b - Other Considerations

In order to eliminate the sharp absorption lines in the far infrared produced by rotational levels in water molecules, the interferometer and light pipe were kept under a vacuum. The vacuum systems of the interferometer and the sample assembly were separated at the exit of the condensing cone (Figure 2.1) by a 75 micron black polyethylene film. The light pipe in the sample assembly was pumped to a pressure of 10^{-4} torr by a rotary

and diffusion pump assembly. Initially, the interferometer was evacuated with a rotary pump which was then valved off and replaced by a sorption pump (Varian model 941-6001) which held the pressure at 0.2 torr. The latter pump was employed so as to eliminate the vibrations inherent in rotary pump operation.

The elimination of spectral intensities at frequencies greater than ω_{max} was accomplished by a combination of filters and beamsplitters. Because of interference effects between the front and back surfaces of the beamsplitter, the spectrum had minima at frequencies, ω, given by Cano and Mattioli (1967)

$$\omega = \frac{m}{2d(n^2-1/2)^{1/2}} \qquad (2.16)$$

where m = 0, 1, 2, 3, ...

d = beamsplitter thickness

and n = index of refraction of the beamsplitter.

This effect was used to good advantage by choosing a beamsplitter of thickness such that the spectrum had its first minimum just beyond the highest frequency of interest. Then, the addition of high frequency cut-off filters completed the filtering. Table 2.1 lists the beamsplitters and filters used in these experiments for operation in various spectral regions of the far infrared.

c - Quality Factor

A useful measure of the performance of the entire system (source plus interferometer) as far as intensity fluctuations

Table 2.1: Interferometer filtering for various spectral regions in the far-infrared

Region (cm^{-1})	Beam Splitter thickness (microns)	Filters	Temperature of filter (°K)
5-50	50	black polyethylene KBr	300 2
10-100	25	black polyethylene crystal quartz	300 2
20-220	12	black polyethylene crystal quartz or sapphire	300 2 2
40-480	6	black polyethylene sapphire	300 2
80-625	3.5	black polyethylene black polyethylene	300 2

are concerned has been proposed by J. Connes and P. Connes (1966). They define a quality factor, q, such that

$$q = m \frac{S_m}{S_{rms}} \tag{2.17}$$

where

$$m = \frac{\Delta\omega}{\delta\omega} . \tag{2.18}$$

$\Delta\omega$ is the spectral width outside of which the intensity is zero (Figure 2.3c), $\delta\omega$ is the resolution and so m is the total number of spectral elements. S_m is the mean spectral intensity and S_{rms} is the root-mean-square of the noise on the spectrum in a region where the spectral intensity is zero. q is a measure not only of the signal-to-noise ratio on the spectrum but also of the difficulty involved in obtaining the signal-to-noise ratio which is related to the number of spectral elements, m. The larger q is,the better the performance of the system. Generally, in the experiments to be described later, broad-band spectra were studied with $\delta\omega$ = 0.2 cm^{-1}, $\Delta\omega$ = 500-200 = 300 cm^{-1} and S_m/S_{rms} typically from 10^2 to 10^3. Thus q was of the order of 10^5 to 10^6. Since this parameter is not yet in wide use it is not possible to compare the above values with other workers' results although there are indications that they are comparable.

B - PERIPHERAL EQUIPMENT

i - Sample Assembly

a - Description

The sample assembly was designed to permit transmission spectra to be taken of a sample in a magnetic field as a function of temperature (Figure 2.4). The lower portion of the assembly

Figure 2.4: Schematic cross-sectional view of sample assembly.

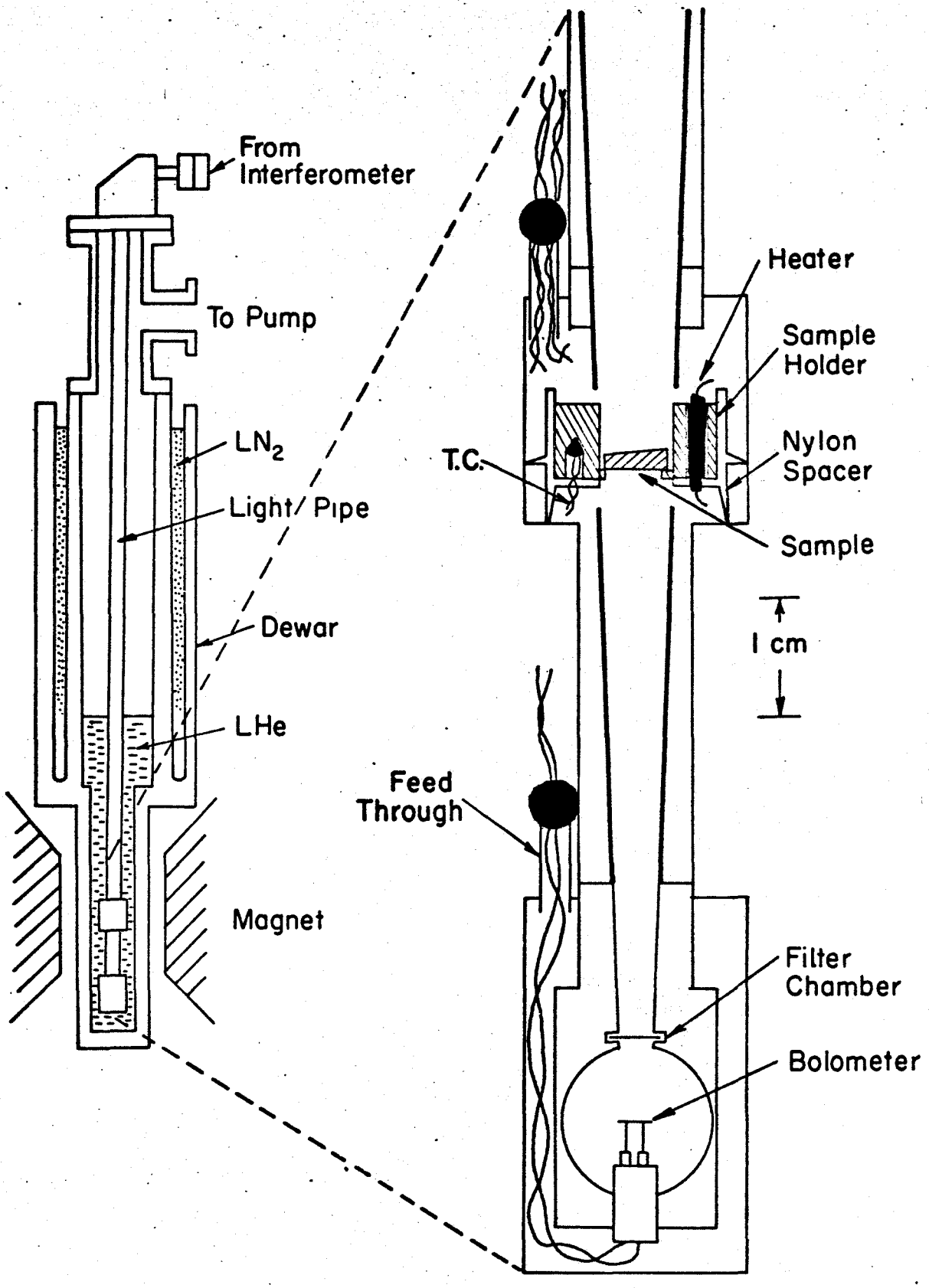
From Interferometer
To Pump
LN_2
Light Pipe
Dewar
LHe
Magnet
Heater
Sample Holder
T.C.
Nylon Spacer
Sample
1 cm
Feed Through
Filter Chamber
Bolometer

was situated in a stainless steel dewar containing the pumped liquid helium bath which kept the detector at its operating temperature of 2°K. Provision was made for the sample's temperature to be increased without seriously affecting the operation of the bolometer located 2-1/2 inches below it.

Light reached the sample chamber by proceeding through about 4 feet of light pipe after exiting the interferometer. Travelling horizontally from the interferometer the light was reflected by a 45° mirror and passed vertically down 3-1/2 feet of light pipe to the sample. The light pipe was constructed of thin wall (0.01 inches thick to minimize thermal conduction) 1/2 inch I.D. brass tubing polished to a high finish on the inside. It is estimated that only about 20% of the total energy entering the pipe is lost along the way (Richards, 1964). Just above the sample chamber a long condensing cone reduced the aperture. The sample holder, a copper cylinder with a 1/4 inch diameter hole in the center, was situated at the exit of this cone. The sample was seated on a lip in the hole held in place with silver paste. Two holes, 180° apart, were drilled in the copper block to accommodate a heater, a 1/8 watt carbon resistor, and a copper-constantan thermocouple. The mass of the sample holder worked to equalize the temperature of the thermocouple, sample holder and sample. To reduce heat loss by the sample holder to the walls of the chamber, which were at liquid helium bath temperatures, the copper block was held away from the walls by a nylon spacer. The fact that the major heat

leak to the helium bath was found to be via the electrical leads to the thermocouple and heater can be attributed to the effectiveness of the nylon spacer.

The light, after passing through the sample, passed through another condensing cone which further reduced the aperture. After crossing a filter chamber, the light then entered a 1/2 inch integrating sphere which contained the detector. The sample chamber and the detector chamber were connected by a thin wall stainless steel tube to reduce heat flow between them. Vacuum tight electrical leads into these chambers were provided by feedthroughs constructed using an epoxy (Stycast 2850 GT) chosen for the similarity of its coefficient of thermal expansion to that of metals.

The success of the design may be judged by the fact that it was possible to obtain useable spectra, which necessitates the bolometer being at or near 2°K, when the sample temperature exceeded 200°K.

b - Temperature Control

Utilizing a negative feedback system, the temperature of the thermocouple was stabilized to within one degree Kelvin over most of the temperature range used. The sample holder thermocouple voltage was compared with the output from a voltage divider (a ten turn potentiometer with a 1.5 volt mercury cell across it) which was used to set the temperature desired. The voltage difference was amplified (Hewlett-PAckard 419A) and

used to bias a transistor which controlled the current supplied to the heater from a D.C. power supply. A D.C. null voltmeter monitored the thermocouple voltage.

Calibration of the thermocouple was achieved using another copper-constantan thermocouple in direct contact with the sample. The leads of the second thermocouple exited via the light pipe. The difference between the readings of the two thermocouples was approximately 18°K over most of the temperature range.

c - Sample Preparation

The InSb studied in these experiments was obtained from the Consolidated Mining and Smelting Company of Canada Limited. The n-type single crystal material possessed a nominal electron mobility of 6 to 7×10^{5} V^{-1} sec^{-1} and a typical net carrier concentration of about 10^{14} cm^{-3} at liquid nitrogen temperature. It was cut into the required shape with a spark cutter and then lapped with various grades of sandpaper until the proper thickness and wedging were achieved. The surface was not treated in any special way as the absorptions studied in these experiments were due to bulk effects.

ii - Detector

The broadband detector employed in these experiments was a gallium-doped germanium bolometer. A very detailed account of the theory of operation of this temperature sensitive resistor has been published by Zwerdling, Smith and Theriault (1968). Intrinsically the responsivity of a bolometer (signal out for power in) rests on its temperature sensitivity and

absorptivity, both of which depend on impurity concentration. A high concentration improves the absorption of radiation but degrades temperature sensitivity while the opposite occurs for low concentrations. In the "hopping" impurity conduction mode, the resistance,R, of a bolometer may be expressed as

$$R = R_o \exp\left(\frac{\varepsilon}{k_B T}\right) \qquad (2.19)$$

where k_B is Boltzmann's constant, R_o is a constant and ε is the thermal activation energy. ε/k_B values in the literature range from 4 to about 20°K compared with about 30°K for the bolometers fabricated here.

For a given bolometric material, the responsivity is maximized by minimizing the heat capacity of the element, C, and its thermal conductivity to the surroundings, G. Both of these may be accomplished by reducing the operating temperature. The bolometer response time which is a function of the ratio of C to G is only weakly affected by the temperature change. (The time constants of the bolometers were typically a few milliseconds.) It is a rule of thumb that bolometers operate most satisfactory at chopping frequencies from 10 to 20 Hz. The chopper used in this system was driven by a synchronous motor powered by an amplified oscillator signal. The chopping frequency was chosen so that it was far removed from any natural resonances in the system.

The bolometer was designed for pumped helium temperatures to benefit from low temperature operation. The helium bath

containing the sample and detector chambers was pumped by a large capacity Edwards rotary pump (ISC 3000) which was located in an adjoining room in order to diminish pressure and mechanical vibrations. The temperature attained in the bath was approximately 1.2°K but the static bolometer temperature was perhaps twice as large as it was relatively weakly coupled to the bath.

The bolometers were constructed following a procedure developed by A. Tumber (1968). Slices of gallium-doped germanium (with a resistivity of 0.07 ohm-cm at room temperature). purchased from Sylvania, were cut into 1/8 inch cylinders with an ultrasonic drill and then etched to a thickness of 100 microns with CP-4. This geometry maximized the area available for light absorption while minimizing the thermal mass. These discs were then placed on a molybdenum heater strip in a hydrogen atmosphere. Two gallium-doped gold wires were held vertically in a special holder while resting on the bolometer element. Current was passed through the heater strip until the temperature was sufficient to melt the gold wires into the germanium. Ohmic alloyed contacts were formed. After a quick etch in CP-4 to remove any alloying damage, the bolometer was soldered to a feedthrough and mounted in the integrating sphere.

A field effect transistor, operating in the pinch-off mode, acted as a constant current source of approximately 0.9 μA. The use of a quiet F.E.T. resulted in a negligible contribution by the bias circuit to the total noise of the bolometer.

The noise equivalent power (the signal power which produces unity signal to noise ratio for unity bandwidth) of these bolometers was determined by measuring the noise on the signal and calculating the zero frequency responsivity from the D. C. voltage-current characteristic of the bolometer (Jones, 1953). The responsivity obtained in this manner, 5×10^{5} V/W, is probably within a factor of two of the actual value since the absortivity is not 100%. The noise on the signal was usually of the order of 3×10^{-7} volts r.m.s measured in a bandwidth of one Hz. Thus the typical N.E.P. was 6×10^{-13} watts/$(Hz)^{1/2}$.

iii - Data Acquisition

A schematic diagram of the data acquisition system is given in Figure 2.5. The bolometer signal received an initial power gain of about 10^{8} in the preamplifier. This low noise unit was a modified version of a preamplifier designed by Zwerdling, Theriault and Reichard (1968). It featured a high input impedance for proper matching to the bolometer's resistance, a low noise, silicon N-channel junction field effect transistor (2N5592) input stage and an output impedance of one ohm. Testing verified a negligible contribution by the preamplifier to the bolometer noise.

The output from the preamplifier was coupled to the input stage of a laboratory designed and built lock-in amplifier through a 100 to 1 step-up transformer. The input amplifier could be operated in a wideband mode (Q=0) or a narrow band mode (Q=10). The amplifier signal was synchronously rectified

Figure 2.5: Block schematic diagram of data acquisition system

M - magnet

S - sample

B - bolometer

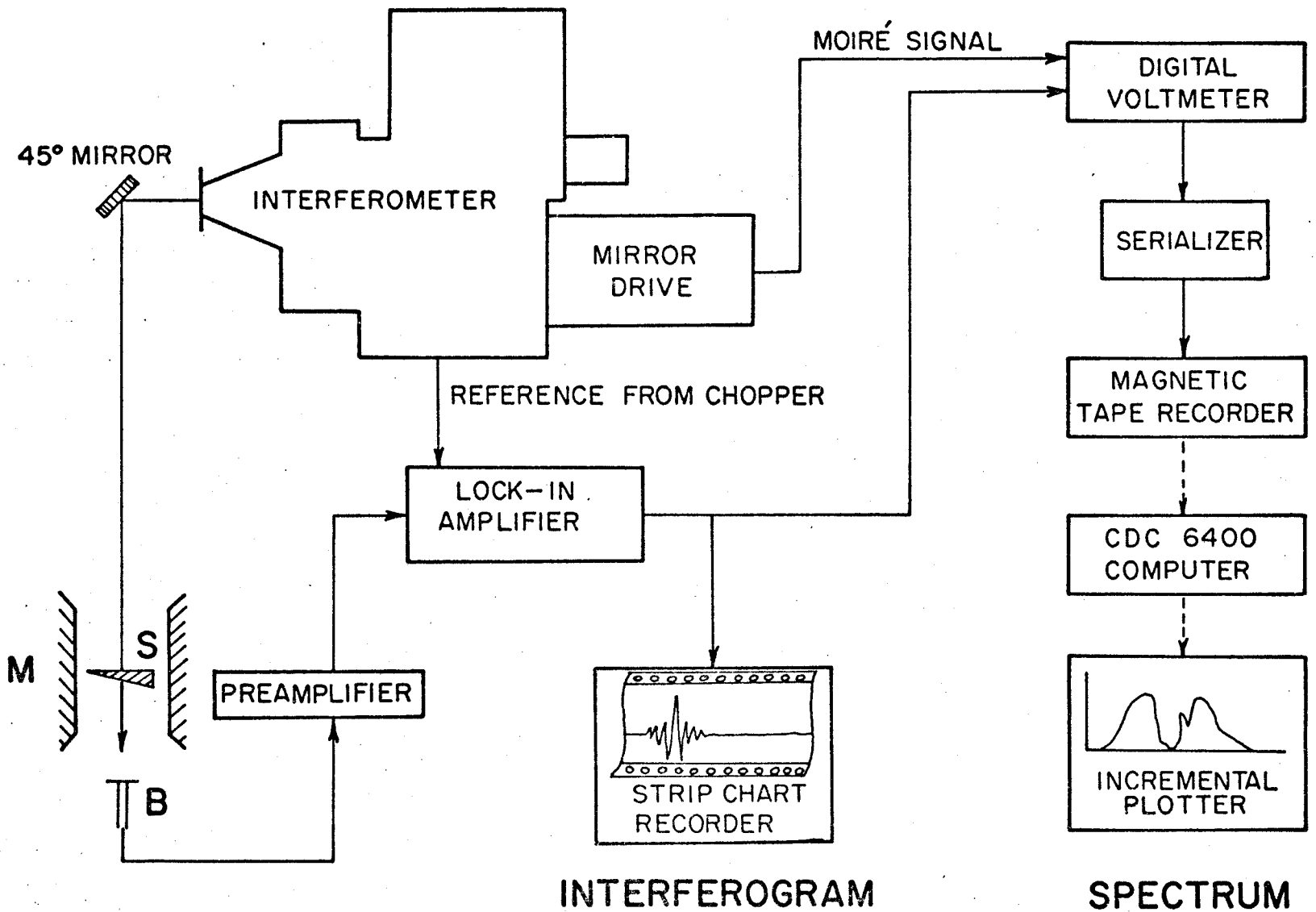
45° MIRROR
INTERFEROMETER
MIRROR DRIVE
MOIRÉ SIGNAL
DIGITAL VOLTMETER
SERIALIZER
MAGNETIC TAPE RECORDER
CDC 6400 COMPUTER
INCREMENTAL PLOTTER
REFERENCE FROM CHOPPER
LOCK-IN AMPLIFIER
PREAMPLIFIER
M
S
B
STRIP CHART RECORDER
INTERFEROGRAM
SPECTRUM

with the aid of a reference signal obtained from the chopping system. A plastic disc, half opaque, half clear, was mounted on the axis of the chopping vane. The coupling of an infrared GaAs light emitting diode placed on one side of the disc with a phototransistor placed on the other side was interrupted by the passage of the opaque section of the disc as the chopper rotated. The signal generated, which was synchronous with the chopper rotation was amplified and fed into the reference channel of the lock-in amplifier.

The rectified bolometer signal was integrated by an RC filter (with a time constant typically 0.1 sec) and again increased with a D.C. output amplifier. The whole system was designed for low-noise operation and the output noise was about 50 μV r.m.s. on 10 volts DC. For typical input signal levels, the signal-to-noise ratio of the lock-in amplifier was 1 part in 10^5 or at least an order of magnitude better than the signal to noise ratio on the signal from the bolometer.

The output of the lock-in amplifier was continuously monitored with a strip chart recorder and digitized by a Hewlett Packard multi-meter (3450 A) capable of resolution of 1 part in 10^5. The parallel B.C.D. output from this digital voltmeter was sequentially fed to a Digi-Data 1337 incremental tape recorder through a serializer. This laboratory built serializer also had provision for entering manual records onto the tape. The data in the digital voltmeter was written on the magnetic tape whenever a pulse was received from the Moiré

reference system. With this data acquisiton system, it was possible to record about 8 interferogram points per second. The slowest component of the system was the digital voltmeter.

iv - Magnet

The electromagnet employed in these experiments was capable of attaining 19 k0e in a two inch gap. Control of the magnet power supply was achieved with a feedback signal generated by a solenoid in the gap. The field was monitored with a Rawson gaussmeter (model 501) which was frequently calibrated by comparison with an N.M.R. gaussmeter to maintain an accuracy of 0.1%.

C - COMPUTATION

The necessity of performing a Fourier transform of the interferogram in order to derive the spectrum has always been the major drawback of interferometry. However, the discovery of the Fast Fourier Transform (Cooley and Tukey, 1965) and the development of fast computers has diminished the problem considerably. Typically in these experiments, 6,250 interferogram points were transformed in about 12 seconds of central processor time on a Control Data 6400 computer.

The computer program was designed first to apodize the interferogram using a triangular function, and then to transform it. The Fourier transform subroutine included a procedure due to Forman et al (1966) for correcting zero path difference errors. This consisted of deriving the phase errors in the spectrum as a

function of frequency and then correcting the computed spectrum for them. A two-sided transform, performed on a very short section of the interferogram centered on zero path difference yielded the true phase spectrum, albeit with poor resolution. However the resolution was not important as the phase spectrum is usually a smooth, slow function of frequency. The true phase spectrum was then compared with the actual phase spectrum obtained from the transform of the complete one-sided interferogram in order to obtain the phase error spectrum. This was used to correct the computed spectrum. It is necessary for spectra to be corrected for zero path difference errors in this manner if averaging and ratioing are to be performed.

The computed and corrected spectrum was then either written on magnetic tape for the use of an incremental plotter, presented in the form of a graph by the line printer or punched on cards for use in averaging and ratioing programs.

Copies of all the interferograms were stored on library magnetic tapes for possible future use.

CHAPTER III

CYCLOTRON RESONANCE

A - THEORY

i - Background

Cyclotron resonance in a solid is a direct and accurate method of determining the effective masses of charge carriers. The significance of such a measurement lies in the fact that it provides information concerning the shape of the most important electronic energy bands in a solid, those containing charge carriers. The first successful cyclotron resonance experiment in a solid was accomplished by Dresselhaus, Kip and Kittel (1953) and since then a great deal of knowledge of the energy bands of semiconductors has been obtained using this technique.

Classically, it is possible to picture the free carriers of a semiconductor as executing spiral orbits in the presence of a steady magnetic field, H. The angular frequency of rotation, ω_c, can be readily calculated using the equality of the centripetal force and the Lorentz force,

$$\omega_c = \pm \frac{eH}{m^* c} \qquad (3.1)$$

e is the electronic charge on the carriers, c is the velocity of light and m* is the effective mass of the carriers. If

electro-magnetic radiation of the same frequency is incident on these rotating particles, resonant absorption of energy takes place. Usually cyclotron resonance experiments are performed by fixing the frequency of the incident radiation (generally in the microwave region) and scanning the magnetic field and therefore ω_c. Alternatively the field can be kept constant and the frequency of the incident radiation scanned with a spectrometer, as was done in these experiments.

Scattering processes limit the lifetime of the carriers in a particular orbit. In order for resonant absorption to occur the electron must be in its orbit for a time comparable to the period of the radiation, ie the electron's lifetime, τ, must be long enough to permit it to travel at least one radian of a circle between successive collisions. This is expressed mathematically as

$$\omega_c \tau > 1 . \qquad (3.2)$$

The larger this product is, the sharper the resonant linewidth. τ is generally of the order of 10^{-13} to 10^{-14} seconds at room temperature, necessitating the use of high purity crystals at low temperatures if cyclotron resonance is to be studed in the microwave region. Operation in the far infrared region of the spectrum increases ω_c and thus relaxes the requirements for a long τ. However, large magnetic fields are then necessary unless semiconductors with small effective masses, such as InSb are studied.

The effective mass, m*, as measured in cyclotron resonance experiments in a crystal differs from that of a free electron as a result of interactions between the electron and the static periodic lattice potential. (For simplicity, the only carriers discussed from now on will be electrons; holes will be ignored.) The effective mass of an electron determined in this manner can be related to the curvature of the conduction band dispersion curve (Kittel, 1968).

$$\left(\frac{1}{m^*}\right)_{ij} = \frac{1}{\hbar^2}\frac{\partial^2 E(k)}{\partial k_i \partial k_j} \qquad i,j = x,y,z \qquad (3.3)$$

where $\hbar$ is Planck's constant, E(k) is the electronic energy as a function of momentum and k_i, k_j are momentum components in the i and j-th directions. Thus cyclotron resonance can be used to determine the form of the energy surfaces of the conduction band. For the free electron case, $E(k) = \hbar^2 k^2/2m_e$ and so $m^* = m_e$, the free electron mass. If the conduction band is anisotropic, effective mass measurements as a function of crystal orientation map out the shape of the band. For an isotropic band, equation (3.3) reduces to

$$\frac{1}{m^*} = \frac{1}{\hbar^2}\frac{\partial^2 E(k)}{\partial k^2} \; . \qquad (3.4)$$

For more rigorous analysis of cyclotron resonance absorption in a semiconductor a quantum mechanical treatment is necessary. In the presence of a magnetic field, the electronic energies of electrons become, in the case of a simple parabolic

band (Ziman, 1964)

$$E(k) = (n + \frac{1}{2})\hbar\omega_c + \frac{\hbar^2 k_H^2}{2m^*} \qquad (3.5)$$

where $n = 0,1,2,\ldots$ and k_H is the momentum in the direction of the field. Conduction band energy levels for k values perpendicular to the field coalesce into discrete Landau states while the momentum component parallel to the field still possesses the free electron form (Figure 3.1). The density of electronic states has a maximum at $k = 0$. Thus for small electron concentrations and low temperatures, $k_H \simeq 0$.

From a quantum mechanical viewpoint, cyclotron resonance absorption is the result of radiation induced electric dipole transitions between adjacent Landau levels with similar spin. Figure 3.1 is a diagram of the first three spin-split Landau levels in InSb in a field of 15 k0e as a function of k_H. The The cyclotron resonance transitions, denoted by (a) were displaced horizontally from $k_H = 0$ for clarity. The selection rules for this intraband transition in a parabolic band permit only transitions that result in $\Delta n = \pm 1$. When large spin-orbit interactions are taken into account (McCombe, 1969) other transitions are possible such as spin resonance ($\Delta n = 0$, $\Delta s = \pm 1$; s is the spin quantum number, labelled (b) in Figure 3.1) and combination resonance ($\Delta n = \pm 1$, $\Delta s = \pm 1$; labelled (c)). Non-parabolicity in an energy band also modifies the selection rules so that harmonic cyclotron resonance transitions are allowed ($\Delta n = \pm 2, \pm 3 \ldots$; labelled (d)). Non-parabolicity also alters the even spacing of the Landau levels so that, say,

Figure 3-1: Landau levels in InSb at 15 k0e as a function of k_H. Four types of intraband transition are illustrated: cyclotron resonance, a; spin resonance, b; combined resonance, c; and harmonic cyclotron resonance, d. The transitions are pictured displaced horizontally for clarity.

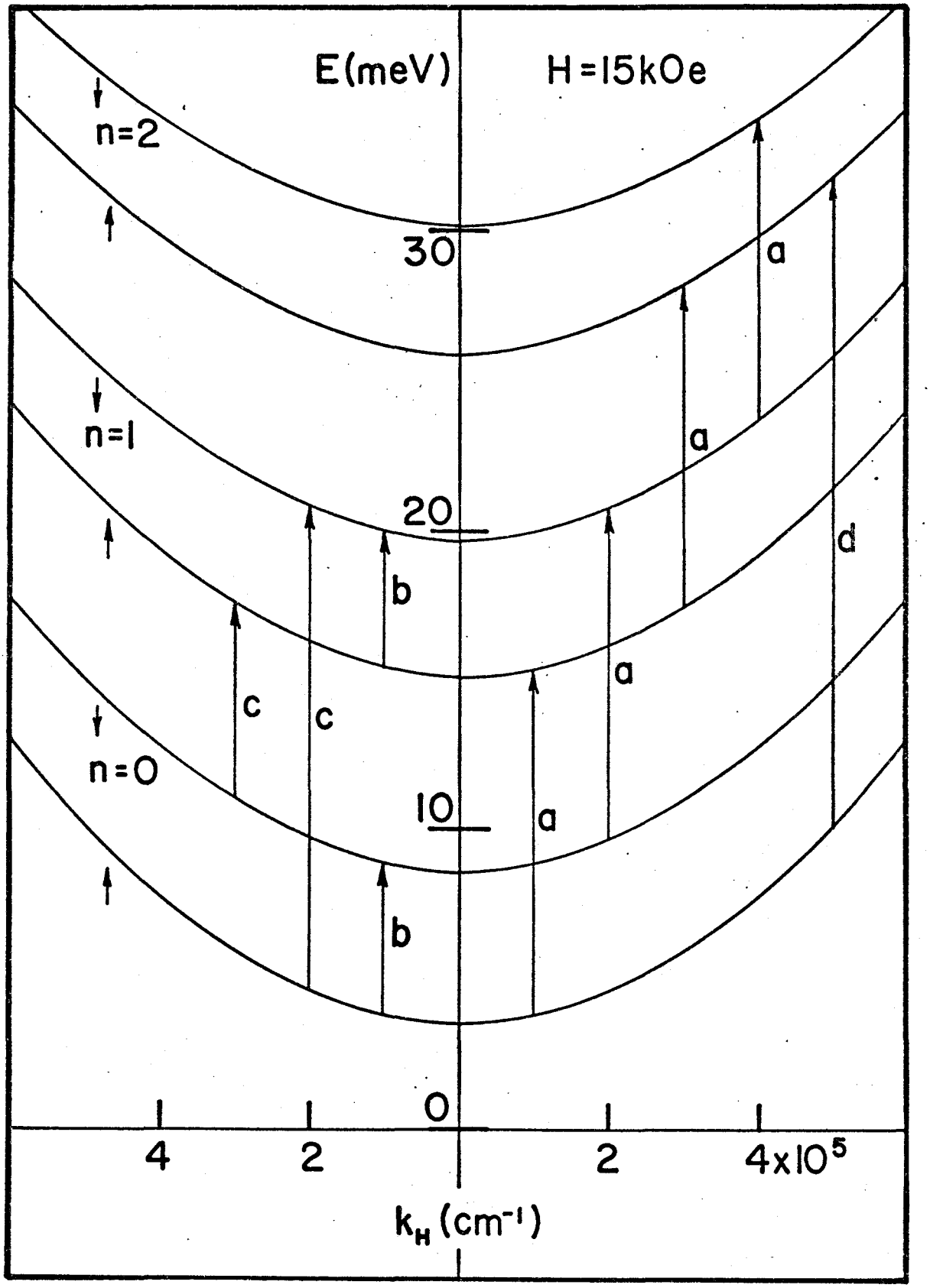
E(meV)
H=15kOe
n=2
n=1
n=0
30
20
10
0
a
a
a
a
b
b
c
c
d
4
2
2
4x10^5
k_H (cm^-1)

the cyclotron resonance transition energy band between states $n = 0$ and $n = 1$ with spin up is not equal to that of $n = 0$ and $n = 1$ with spin down. High resolution infrared spectroscopy is able to distinguish these two cyclotron resonance transitions.

Radiative absorption by electrons free to move throughout the crystal is not the only type of cyclotron resonance absorption possible in semiconductors. At low temperatures, some of the electrons become trapped at impurity sites. The Coulomb interaction responsible for localization is weak compared to the interaction with the magnetic field and so the localized electrons also experience cyclotron resonance transitions. Due to the energy of binding, their energies are slightly larger than that of the other electrons and so their cyclotron resonance absorptions occur at slightly higher frequencies in a fixed field. If the temperature of the sample is increased, ionization of these localized electrons reduces the intensity of this absorption very rapidly. This temperature dependence is a sensitive indication of the nature of the electrons contributing to a cyclotron resonance absorption.

In the Voigt configuration, the geometry employed in these experiments, both the magnetic field and the electric vector of the electromagnetic radiation are in the plane of the sample. Depolarization effects related to the sample geometry can shift the position of the cyclotron resonance absorption (Dresselhaus et al, 1955). For the shape of sample

used, the observed position ω_c'' and the true cyclotron frequency, ω_c are related by

$$\omega_c = \omega_c'' \left[1 - \left(\frac{\omega_p}{\omega_c}\right)^2\right]^{1/2} \tag{3.6}$$

or

$$\omega_c^2 = (\omega_c'')^2 - (\omega_p)^2 \tag{3.7}$$

where ω_p is the plasma frequency, the frequency at which a semiconductor becomes highly reflecting due to free carrier absorption. It is given by

$$\omega_p^2 = \frac{4\pi Ne^2}{m^*\varepsilon_o} \tag{3.8}$$

where N is the free carrier density and ε_o is the static dielectric constant of the host lattice. Generally this plasma shift becomes serious only when the magnitudes of ω_p and ω_c are comparable.

ii - Electronic Energy Bands in InSb

InSb is a III-V compound semiconductor which has a non-parabolic conduction band and an unusually small electron effective mass (about 0.138 of a free electron mass at zero temperature and momentum). Both of these characteristics stem from a small energy gap (about a quarter of an electron volt at 0°K) which leads to a strong interaction between the conduction and valence bands. With this in mind, E. O. Kane (1957) derived a band structure for InSb in the region of the Brillouin zone center ($k \simeq 0$) by treating exactly the mutual interaction of the conduction and valence bands via the $\underline{k}.\underline{p}$ interaction and the k-independent spin-orbit interaction. Second order

perturbation theory was used to estimate the effects of higher and lower bands. Neglecting higher bands, Kane obtained the following secular equation for the energy E of the electronic bands.

$$E(E-E_g)(E+\Delta) - k^2P^2(E + \frac{2}{3}\Delta) = 0 \qquad (3.9)$$

where E_g is the k = 0 energy gap, Δ is the spin orbit splitting, k is the momentum and P is the matrix element, $-\frac{i\hbar}{m_e}\langle S|p_z|z\rangle$ relating the unperturbed wave functions of the conduction and valence bands respectively (Figure 3.2).

For small values of k^2, the solution of equation (3.9) results in a parabolic conduction band

$$E = E_g + \frac{\hbar^2k^2}{2m_e} + \frac{P^2k^2}{3}\left(\frac{2}{E_g} + \frac{1}{E_g + \Delta}\right). \qquad (3.10)$$

Surfaces of constant energy are spheres centered on the Γ point (k = 0) and the effective mass for $k \simeq 0$, m_o^*, is simply (see equation (3.4))

$$\frac{m_e}{m_o^*} = 1 + \frac{2m_eP^2}{3\hbar^2}\left(\frac{2}{E_g} + \frac{1}{E_g + \Delta}\right) . \qquad (3.11)$$

Away from Γ the conduction band, although still isotropic, is strongly non-parabolic. Kane's model was developed for the case of zero magnetic field and so the conduction band is doubly degenerate.

Bowers and Yafet (1959) and Yafet (1959) were the first to consider the case of the energy levels of InSb in the presence of a D.C. magnetic field. Following Kane and neglecting

Figure 3.2: The electronic energy band structure of InSb. The dashed line illustrates the shape the conduction band would have if it were parabolic with a curvature given by the band edge effective mass.

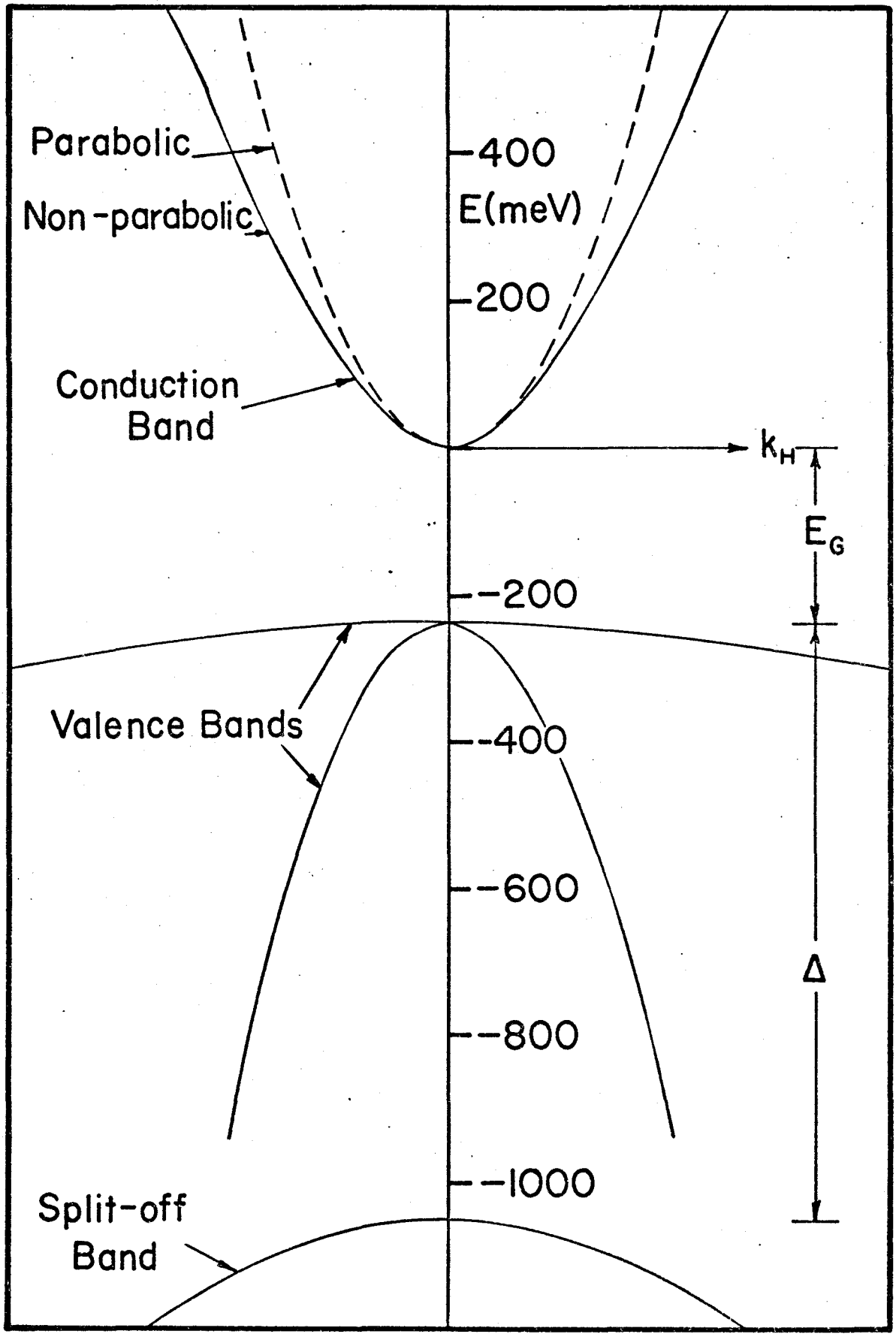
Parabolic
Non-parabolic
Conduction Band
400
E(meV)
200
k_H
E_G
-200
Valence Bands
-400
-600
Δ
-800
-1000
Split-off Band

higher band effects and certain second order terms, they derived the following expression for the conduction band Landau levels (Palik et al, 1961).

$$E(n,s) = \frac{1}{2} E_g\{1 + (1 + 2(2n+1) \mp \frac{1}{2}) \frac{h\omega_c}{E_g})^{1/2}\} \quad . \quad (3.12)$$

Here n is the Landau level quantum number and $s = \mp$ gives the spin splitting. The non-parabolicity of the conduction band is clearly evident in this equation (compare to equation (3.5)). Other workers seeking more precision, derived more elaborate equations by avoiding the use of simplifying assumptions. Thus, Lax et al (1961) obtained this implicit equation for E(n,s).

$$E(n,s) = \frac{2\beta m_e H}{m_o^*} \frac{E_g(E_g+\Delta)}{3E_g+2\Delta} (n + \frac{1}{2}) [\frac{2}{E(n,s)+E_g} + \frac{1}{E(n,s)+E_g+\Delta}]$$

$$\mp \frac{1}{2} \beta g_o^* H \frac{E_g(E_g+\Delta)}{\Delta} [\frac{1}{E(n,s)+E_g} - \frac{1}{E(n,s)+E_g+\Delta}] \quad (3.13)$$

where $\beta = eh/2m_e c$. m_o^* and g_o^* (the effective spectroscopic splitting factor) are the values for these quantities at the bottom of the conduction band (k=0). Johnson and Dickey (1970) derived an expression similar to equation (3.12).

$$E(n,s) = -\frac{1}{2} E_g + \frac{1}{2} E_g(1 + \frac{4f_1}{E_g}(2n+1)\frac{m_e}{m_o^*} \beta H \pm \frac{1}{2} g_o^* \beta H f_2))^{1/2} \quad (3.14)$$

where

$$f_1 = \frac{(E_g+\Delta)(E(n,s) + E_g + \frac{2}{3}\Delta)}{(E_g + \frac{2}{3}\Delta)(E(n,s) + E_g+\Delta)} \quad (3.15)$$

and

$$f_2 = \frac{E_g + \frac{2}{3}\Delta}{E(n,s) + E_g + \frac{2}{3}\Delta} \quad . \quad (3.16)$$

Both equations (3.13) and (3.14) were derived by neglecting higher band interactions. Calculations by Palik et al (1961) including these interactions indicated that the difference between their more exact theory and that given by equations (3.13) and (3.14) were insignificant for magnetic fields up to 70 kilo-oersteds. Higher band effects also become important for highly doped material ($N > 10^{17}$ cm^{-3}) (Kolodziejczak et al, 1966). In each of these instances, the conduction band is being probed in regions far removed from $k \simeq 0$. However the high resolution spectroscopic system developed here makes it possible to investigate the influence, if any, of higher band effects on the conduction band near $k \simeq 0$ with greater accuracy than before.

The measured cyclotron resonance frequency is equal to the energy difference between two adjacent Landau states with similar spin. Since g_o^* is negative (~ -51 at 4°K, McCombe and Wagner, 1971), the lowest lying level has spin up. The effective mass can be related to the energy levels by

$$\frac{1}{m^*} = \frac{c}{\hbar eH} \left(E(n+1,s) - E(n,s)\right). \qquad (3.17)$$

The non-parabolicity of the conduction band produces unequally spaced Landau levels to that

$$(E(1,+)-E(0,+)) > (E(1,-)-E(0,-)) > (E(2,+)-E(1,+)), \text{ etc.} \qquad (3.18)$$

If the sample temperature is raised other levels besides the lowest are populated, and higher level cyclotron resonance transitions become possible. A number of non-coincident absorptions are observed. Since the spacing of Landau levels decreases as n increases (Figure 3.1), the cyclotron frequency also decreases and the effective mass increases. In effect the curvature of the conduction band is being probed higher in the band. The simultaneous appearance of four such transitions (see Figure 3.6) can only be explained using quantum theory and so they are termed quantum effects. The relative strengths of these peaks are temperature dependent through a Boltzmann distribution function.

This decrease in curvature higher in the band can also be probed by measuring the effective mass as a function of magnetic field. In contrast to the case of a parabolic band in which the curvature and thus m* is independent of k and H, in InSb as H increases, m* increases. Effective mass versus magnetic field curves are a sensitive test of the theory.

Careful analysis of the basic theory employed to derive the equations above indicates that the inclusion of still higher order terms would result in a small anisotropy in m* and a larger one in g* (Pidgeon, Mitchell and Brown, 1967). For the magnitude of fields and concentrations used here, the anisotropy in g* is, at the most, 2%. For m* it is much less but, in any case, could be neglected as all the experiments were performed on one sample mounted in a fixed position relative to the field.

A great many experiments employing a variety of techniques have been performed in recent years to investigate the validity of Kane's model of the electronic energy band structure of InSb. Generally these studies, including the latest extensive one (Johnson and Dickey, 1970) have proven the theory to be quite satisfactory. The precision possible with the high resolution far-infrared spectrometer system developed here makes possible an extension of these studies. The effect, if any, of higher bands on the effective mass versus magnetic field curves was investigated and half an order of magnitude more accurate values of m_o^* and g_o^* determined. Once confidence was established that Kane's model predicted the effective mass versus magnetic field curves accurately for the magnetic fields employed here (up to 19 kOe), then anomalies in the effective mass versus magnetic field curves for higher transitions were investigated with great precision. These were predicted to result from resonant electron - LO phonon coupling (see section A-iii). A value of the coupling constant was determined that was a factor of five more precise than before.

Kane's theory was developed assuming a rigid lattice. Many workers have concluded that the only effect of temperature on the band edge effective mass would be through the change in crystal volume and therefore E_g caused by lattice dilation as expressed in equation (3.11). Stradling and Wood (1970) have investigated this contention in a number of semiconductors using magnetophonon resonance techniques. Although they showed

that the major contribution to the effective mass change with temperature was due to lattice dilation, the accuracy of their results (± 1%) precluded a definite conclusion that it was the only effect. These experiments provided an order of magnitude more accuracy in effective mass determination and so it was possible to search for any discrepancy between the theoretical and experimental temperature dependence that could be ascribed to electron-phonon effects or deficiencies in the theory (section A-iv).

iii - Resonant Electron-LO Phonon Coupling

In a polar semiconductor an electron in the conduction band, in addition to interacting with the static periodic lattice potential can also couple to polarization waves set up by phonons. In effect the electron induces a region of polarization charge around itself which interacts in turn, with the electron altering its motion through the rigid lattice. This excitation, comprised of the electron plus its polarization charge, is called a polaron. Since polarization charge is usually carried by longitudinal optical (LO) phonons, polaron theory is really a theory of electron-LO phonon interaction (for a recent extensive review, see Harper et al, 1973). The strength of this interaction is expressed by a dimensionless electron-phonon coupling constant defined by Fröhlich (1954) as

$$\alpha = \left(\frac{m_o^* e}{2\hbar^3 \omega_{LO}}\right)^{1/2} \left(\frac{1}{\varepsilon_\infty} - \frac{1}{\varepsilon_o}\right) \qquad (3.19)$$

where ε_∞ and ε_o are the high frequency and static dielectric

constants respectively and ω_{LO} is the longitudinal optical phonon frequency. α is approximately 0.02 for InSb. For the simplified case of a parabolic band in the presence of a weak magnetic field, the Landau level energies for the weak coupling case ($\alpha < 1$) may be determined from perturbation theory (Larsen, 1964).

$$E(n) \simeq (n + \tfrac{1}{2})\hbar\omega_c(1 - \tfrac{\alpha}{6}) - \alpha\hbar\omega_{LO} \qquad (3.20)$$

ω_c is the unperturbed cyclotron resonance frequency. The observed cyclotron frequency, ω_c', is related to the actual frequency, ω_c, by

$$\omega_c' = \omega_c(1 - \tfrac{\alpha}{6}). \qquad (3.21)$$

Thus the effect of polaron coupling in this case is to shift all the Landau levels by a fixed amount and to increase the effective mass (by 0.3% in the case of InSb). In the absence of a highly accurate theoretical estimate of the effective mass, the magnitude of this change is impossible to determine. A much more direct method of observing polaron effects is to perform polaron level-crossing experiments which resonantly enhances the mass change.

Figure 3.3 is a schematic diagram of the theoretical behaviour of the Landau levels (spin effects excluded) as a function of magnetic field, in the presence of electron-LO phonon coupling. The dashed lines are the unperturbed ($\alpha = 0$) energy levels. The $n = 0$ plus one phonon level, possible when polaron coupling exists, is simply the sum of the lowest lying

Figure 3.3: Landau levels in InSb as a function of magnetic field. Spin effects are ignored. The effect of electron-LO phonon coupling on the unperturbed levels (dashed lines) is shown by the solid lines.

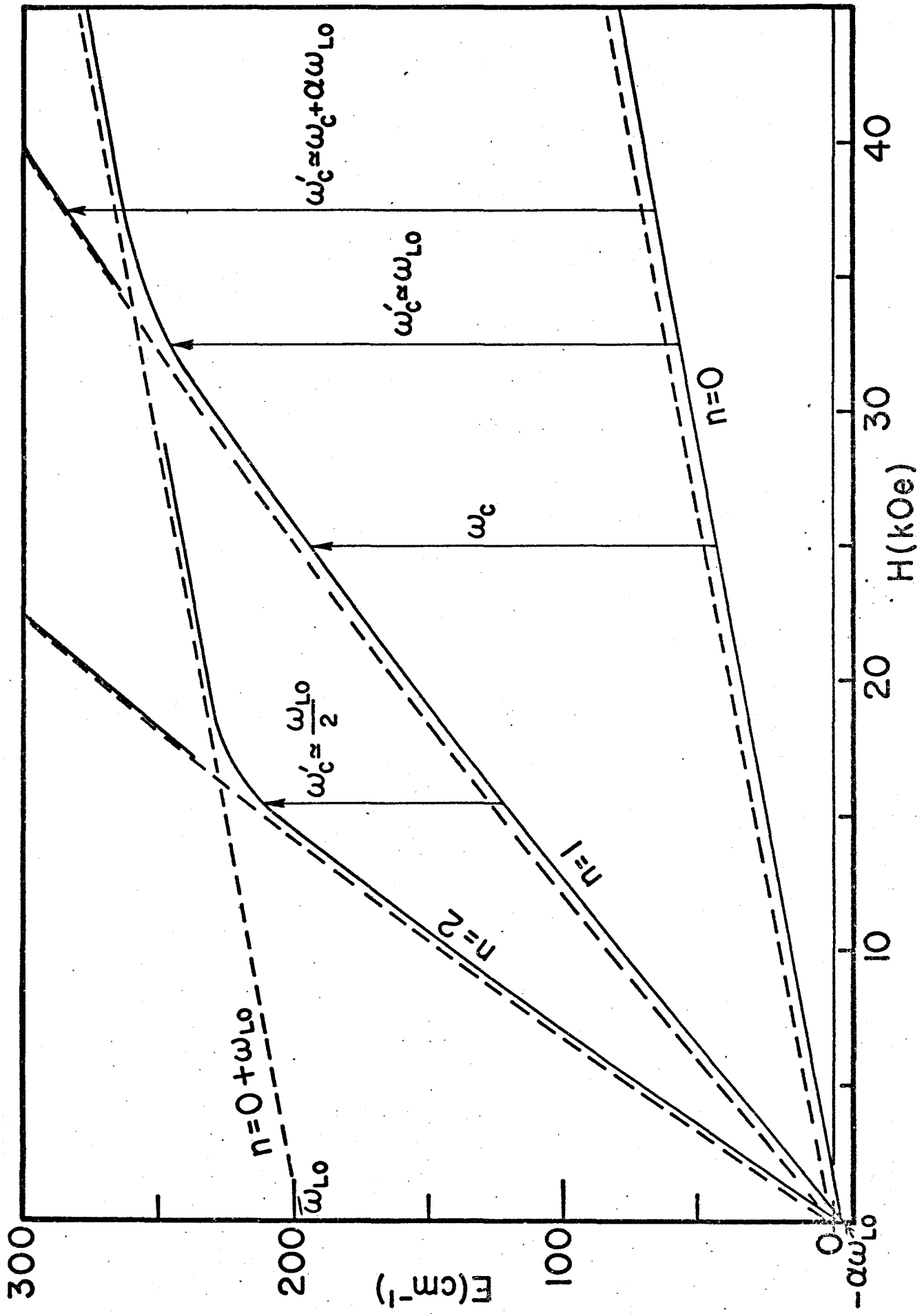
300
200
100
0
E(cm⁻¹)
10
20
30
40
H(kOe)
$\omega_c' \simeq \omega_c + \alpha\omega_{LO}$
$\omega_c' \simeq \omega_{LO}$
ω_c
$\omega_c' \simeq \frac{\omega_{LO}}{2}$
n=0
n=1
n=2
n=0+ω_{LO}
$\bar{\omega}_{LO}$
$-\alpha\omega_{LO}$

Landau level and the LO phonon energy. Consider the case of the n = 1 no phonon level. The addition of coupling reduces its energy by $\alpha h\omega_{LO}$. As H increases, the energy of this level increases in much the same manner as before except when approaching a crossing with the $n = 0 + \omega_{LO}$ level. Then the level begins to bend over and eventually to follow this latter level $\alpha\omega_{LO}$ below it. It becomes "pinned" to this level. In the same region another energy level becomes evident above $n = 0 + \omega_{LO}$ which follows, approximately, the n = 1 unperturbed level. In terms of the energy difference between levels (n = 0 to n = 1, the cyclotron resonance frequency), as H increases, ω_c becomes double valued beyond the region of the level crossing. One frequency saturates with a value of ω_{LO} and the other continues to increase with a value of approximately $\omega_c + \alpha\omega_{LO}$. The linewidths and intensities of these transitions also undergo dramatic changes in the level-crossing region. The saturating cyclotron frequency decreases rapidly in intensity in the strong coupling region while the shifted frequency $(\omega_c + \alpha\omega_{LO})$ gains in intensity. Furthermore on passing through the level-crossing region the absorption linewidth increases dramatically and then decreases as $(\omega_c - \omega_{LO})^{1/2}$ as H continues to increase (Summers et al, 1968). This change in linewidth arises from the strong coupling to the $n = 0 + \alpha\omega_{LO}$ level. The electron lifetime is shortened due to the addition of possible decay modes via a LO phonon. Scattering is therefore enhanced.

Direct attempts to observe pinning and polaron effective

mass enhancement in the region of resonant electron-LO phonon coupling are frustrated by the strength of the Reststrahl band in polar crystals (see Chapter IV). However these effects have been demonstrated indirectly by employing ingenious techniques to avoid the Reststrahl absorption band. Johnson and Larsen (1966) observed pinning in interband magnetoabsorption in InSb and McCombe and Kaplan (1968) studied resonant polaron effects in InSb using combined resonance to shift the coupling anomaly away from the Reststrahl band. No attempts were made to deduce α from these experiments. The only published experimental value of α was obtained by Summers et al (1968) by fitting theory to observed linewidth changes for $\omega_c > \omega_{LO}$ ($\alpha = 0.025 \pm .005$).

Another method of avoiding the Reststrahl problem is to study the resonant electron-LO coupling occurring when the $n = 2$ no phonon and $n = 0 + \omega_{LO}$ levels cross (Figure 3.3). This takes place at about half the magnetic field and cyclotron frequency necessary for the previous case. The polaron mass enhancement as a function of magnetic field resulting from resonant electron-LO phonon coupling of the $n = 2$ no phonon and $n = 0 + \omega_{LO}$ levels has been determined here for the first time in a semiconductor.

The total change in effective mass with magnetic field is the sum of two components; one due to the non-parabolicity of the conduction band and the other resulting from polaron effective mass enhancement. The first of these can be calculated accurately by employing Kane's theory as extended by later

workers. Explicitly, this consists of solving equations (3.13), (3.14) and (3.17) for the higher Landau level transitions (n = 1 to n = 2). Values of m_o^* and g_o^* are determined by fitting the theory to the experimental effective mass versus magnetic field curves obtained from transitions involving lower lying Landau levels (n = 0 to n = 1). These masses are expected to be affected by resonant electron-LO phonon coupling only when the n = 1 and n = 0 + ω_{LO} levels cross at about 35 k0e. For the fields used here (< 19 k0e) resonant polaron mass enhancement was negligible. The difference between the observed effective mass, determined by transitions between the n = 1 and n = 2 levels, and the calculated effective mass, determined by Kane's non-parabolic conduction band, was attributed to resonant polaron mass enhancement.

The problem of deriving a quantitative expression for the polaron coupling in the resonance region has been studied by a number of workers over the last few years. The theory is especially difficult near the crossing point but Larsen (1964, 1966) employing a perturbation theory explicitly calculated the energy shift expected in the cyclotron frequency as a function of magnetic field up to the crossing point. The result, correct to the first order in α, was numerically calculated for the n = 0 to n = 1 transition for the case of weak (α < 1) electron-LO phonon coupling at zero temperature. The energy correction was given in units of $\alpha\hbar\omega_{LO}$ as a function of ω_c/ω_{LO}. An approximation to the correction good to within 5%

over the range $0 \leq \omega_c/\omega_{LO} < 1$ is given by

$$\frac{1}{2}\left[\frac{\sin^{-1}((\omega_c/\omega_{LO})^{1/2}}{(\omega_c/\omega_{LO})^{1/2}} - \frac{1}{(1-\omega_c/\omega_{LO})^{1/2}}\right] . \qquad (3.22)$$

To adapt these results to the energy difference between the n = 1 and n = 2 levels it was necessary to scale the magnetic fields by defining a new ω_{LO}. ω_{LO}' was obtained by setting

$$\hbar\omega_{LO}' = \hbar\omega_c = E(2,s)-E(1,s) \qquad (3.23)$$

at the crossing point of the n = 2 and n = 0 + ω_{LO} Landau levels. Then $\omega_{LO}' \simeq \frac{1}{2}\omega_{LO}$ (Figure 3.3). Since α is a function of ω_{LO}, it also must be suitably redefined. $\alpha' \simeq 1.44\ \alpha$.

The energy corrections obtained in this manner were applied to the cyclotron frequencies predicted by Kane's theory to arrive at a polaron enhanced effective mass.

iv - Temperature Dependence of the Electron Effective Mass

The Kane expression for the band edge effective mass of the conduction electron in a narrow gap semiconductor, given by equation (3.11), was developed assuming a rigid lattice model.

$$\frac{m_e}{m_o^*} = 1 + \frac{2m_eP^2}{3\hbar^2}\left(\frac{2}{E_g} + \frac{1}{E_g+\Delta}\right) . \qquad (3.11)$$

For this reason and since the only parameter in equation (3.11) that is known to be highly temperature dependent is E_g, it is expected that the major effect of temperature on m_o^* will be through the change in E_g produced by lattice dilation. This idea has been expressed by a number of workers but only Stradling

and Wood (1970) have measured the temperature dependence of the effective mass. They determined that the main contribution to effective mass change was lattice dilation but the accuracy of their experimental technique (magnetophonon resonance) was not sufficient to establish whether or not it was the only contribution. The present experiments have been undertaken to help settle that question.

The effect of temperature on m_o^* can be determined by investigating, in turn, the temperature dependence of each of the parameters in equation (3.11); Δ, P and E_g. Δ, the spin-orbit splitting energy of the valence bands, since it is due to an interaction that takes place deep within the atoms, is relatively independent of temperature. Furthermore, according to equation (3.11), m_o^* is only weakly dependent on Δ so that any slight change in its value has a negligible effect on the effective mass.

Likewise P, the momentum matrix element of the interaction between the conduction and valence bands is expected to be insensitive to temperature. Smith, Pidgeon and Prosser (1972) used Faraday rotation techniques to measure electron effective masses in InSb as a function of carrier concentration at two different temperatures. Fitting theoretical curves to their m* versus concentration curves enabled them to derive values of P^2 accurate to 1%. Within experimental error they concluded that P^2 is independent of temperature between 77 and 296°K. Also, Ehrenreich (1961) has shown that P^2 is constant

to within 20% for III-V compounds with energy gaps ranging from 0.25 to 2.5 eV. It is not unreasonable, therefore, that the small change in E_g (less than 20%) experienced by InSb over the temperature range used in these experiments should have no appreciable effect on P^2. Therefore the only parameter in equation (3.11) capable of causing the electron effective mass to be temperature sensitive is the energy gap, E_g.

Through a thermodynamic derivation, it is possible to show that the change in energy gap as a function of temperature at constant pressure is the sum of two components (Fan, 1951).

$$\left(\frac{\partial E_g}{\partial T}\right)_P = \left(\frac{\partial E_g}{\partial T}\right)_V + \left[V\left(\frac{\partial P}{\partial V}\right)_T\right]\left[\frac{1}{V}\left(\frac{\partial V}{\partial T}\right)_P\right]\left(\frac{\partial E_g}{\partial P}\right)_T . \qquad (3.23)$$

The first term, the energy shift due to electron phonon interactions, has a negligible effect on the conduction electron effective mass (Frölich et al, 1950). Although producing a change in E_g of the same order of magnitude as the second term, the coupling of the electron to the total phonon field has little or no effect on the curvature of the conduction band as a function of temperature (Long, 1968 ; This effect should not be confused with the electron-LO phonon coupling which takes place in polar materials only and is relatively temperature independent. This electron-phonon coupling includes all the phonons present in the material).

The second term in equation (3.23) expresses the

change in E_g as a result of lattice dilation and is the dominent factor in the temperature dependence of the effective mass. Neglecting the first term, equation (3.23) may be re-written

$$\left(\frac{\partial E_g^*}{\partial T}\right)_P = -3\alpha_T B \left(\frac{\partial E_g}{\partial P}\right)_T , \qquad (3.24)$$

where α_T is the linear coefficient of thermal expansion and B is the bulk modulus. B can be calculated from measured elastic constants (Slutsky and Garland, 1959) and is found to be slightly temperature dependent. The rate of change of E_g with pressure at constant temperature has been measured by optical (Bradley and Gebbie, 1965) and electrical means (Long, 1955; Keyes, 1955) and again found to be only weakly temperature dependent. α_T on the other hand is strongly temperature sensitive. It has been measured as a function of temperature by a number of workers (Gibbons, 1958; Novikova, 1961; Sparks and Swenson, 1967) and found to behave anomolously at low temperatures. As the temperature of InSb increases from that of liquid helium, the crystal first contracts and then expands, with the change in sign occurring at about 55°K. This anomalous dependence will be mirrored in the change of effective mass with temperature if the dominent mechanism is the lattice dilation change of E_g with temperature. The total change in E_g due to both terms in equation (3.23) does not exhibit this behaviour (Roberts and Quarrington, 1955) as the electron-phonon term dominates at low temperatures. Thus,at finite temperatures, the conduction band curvature and therefore electron effective mass

of InSb is determined by equation (3.11) with

$$E_g(T) = E_g^*(T) = E_g(o) - \left(\frac{\partial E_g^*}{\partial T}\right)_P T \ . \qquad (3.25)$$

Ideally, equation (3.11) should be tested by measuring the band edge effective mass as a function of temperature since the equation is rigorously correct only when k = 0. In a finite magnetic field, the lowest Landau level is $\sim \frac{1}{2}\hbar\omega_c$ above the zero field energy and so the validity of equation (3.11) in these circumstances may be questioned. Measuring a large number of masses as a function of field at each temperature and then fitting these results with theoretical curves in the manner described in section A-ii above in order to obtain a band edge effective mass is a tedious solution. In an effort to preclude this necessity, the temperature dependence of the spin up and spin down n = 0 to n = 1 Landau transitions were measured at three different magnetic fields; 14.08, 16.09 and 18.05 kOe. When normalized to the maximum value of m* measured, the temperature dependences were found to be identical within experimental error. Thus it was concluded that for the sample (relatively pure with a carrier concentration of $\sim 10^{14}$ cm^{-3}) and magnetic fields employed, the use of Kane's band edge effective mass equation is justified.

There is also some question about the effects of thermal broadening on the position of the cyclotron resonance peaks. For k_H not equal to zero, the energy difference between adjacent Landau levels decreases and so the cyclotron resonance effective

mass increases. However, for these carrier concentrations and since there is a maximum in the density of electron states at $k = 0$, little shift in the peak position is expected due to thermal effects. Further, because of a reduced scattering rate from long-range ionized impurities that occurs in the quantum limit, $h\omega_c > k_B T$ (Apel et al, 1971), the cyclotron resonance lines are strongly narrowed. For example, the width at half maximum of the $n = 0$ to $n = 1$ spin up cyclotron resonance absorption line at 108°K in figure 3.9 is only about 3 cm^{-1} compared to the $k_B T \simeq 75$ cm^{-1} expected if thermal broadening was completely effective. In summary then, the fact that at finite temperatures k_H may not equal zero for all electrons, is not expected to have a significant effect on the position of the cyclotron peaks. If there is any effect at all, it will tend to decrease the cyclotron frequencies and so increase the effective masses.

B - OBSERVATIONS

i - Experimental Conditions

The sample used in all the cyclotron resonance experiments was a 75 micron, thick, 1/4 inch diameter, disc cut in a (110) plane. It was wedged to remove interference fringes.

To improve the quality of the spectra, at least two two and sometimes more, identical runs were averaged. They were then ratioed with zero field spectra to remove unwanted background. Peak positions could usually be determined to better than 0.1 cm^{-1}.

Corrections were applied to the peak position values to offset the frequency shifts caused by finite instrument aperture, polaron mass enhancement far removed from resonance and plasma coupling. The magnitude of the first two effects could be calculated in a straightforward manner and the third was estimated in two ways. ω_p was calculated by assuming a value of 10^{14} cm^{-3} for the carrier concentration. Because of the shallowness of the donor impurity levels in this material, this concentration remained constant from liquid helium temperatures until intrinsic conduction became dominant at about 170°K. Secondly, the intercept of a plot of $(\omega_c')^2$ versus $(\frac{H}{m^*})$ was found and set equal to ω_p^2 (see equation (3.7)). The plasma frequency determined using this method compared favourably with that obtained from the first ($\omega_p \simeq 6.5$ cm^{-1}) and confirmed that in most instances, the frequency shift of the cyclotron resonance peaks due to the plasma effect was small. Nevertheless, the correction was always applied.

ii - Electron Effective Mass Versus Magnetic Field

The variation of effective masses with magnetic field for spin up and spin down transitions is shown in Figure 3.4 for a sample temperature of 18°K. At this temperature impurity cyclotron resonance could be neglected and only the n=0 Landau levels were significantly occupied. Therefore only two spin split cyclotron resonance absorption peaks were present in the spectrum. Theoretical curves were calculated using equations (3.12) and (3.14). For given values of m_o^* and g_o^* these

Figure 3.4: Electron effective mass versus magnetic field in InSb at 18°K. The circles are the experimental points and the solid lines were calculated using Kane's theory. The lower curve is the effective mass associated with transitions between n = 0 and n = 1 Landau levels, with spin up and the upper curve is the effective mass associated with transitions between n = 0 and n = 1 Landau levels with spin down.

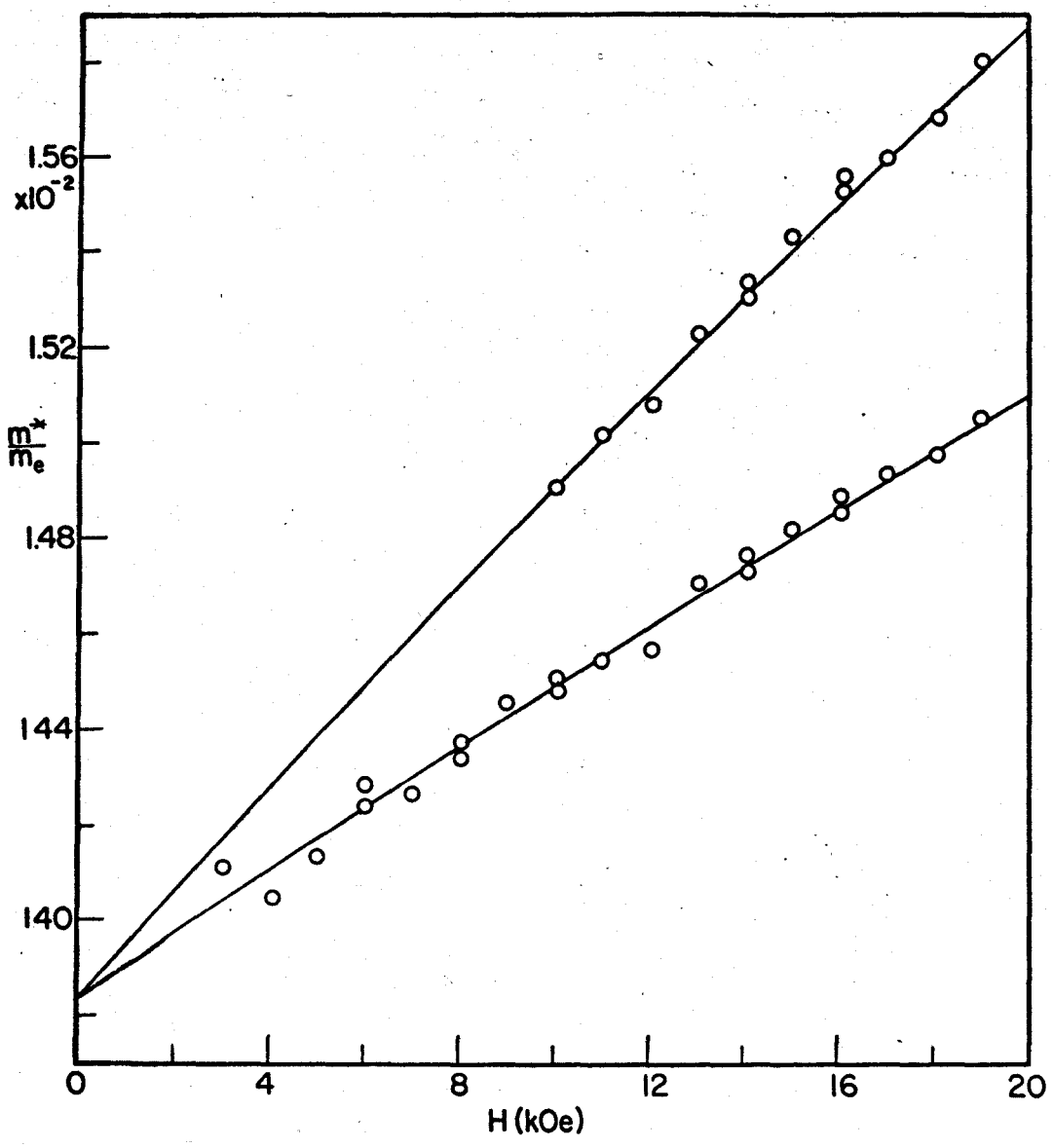
1.56
x10⁻²
1.52
m*/mₑ
1.48
144
140
0
4
8
12
16
20
H (kOe)

two equations produced practically identical m* vs H curves. The value of E_g was taken as 237.1±0.2 meV (Johnson, 1967) and Δ was 810±0.2 meV (Pidgeon, Groves and Feinleib, 1967; Aggarwal, 1967). The literature contains several other values of E_g at low temperatures (Pidgeon and Brown, 1966; Mooradian and Fan, 1966) differing by a slight amount, but since these equations are not unduly sensitive to the exact value of E_g, m* is not changed significantly by a change of E_g. The same is true of Δ.

The theoretical curves were fitted to the experimental points by independently varying m_o^* and g_o^* to get good agreement over the whole range of m*. It was found that the fit depended critically on the magnitude of m_o^* but was not nearly as sensitive to the value of g_o^*. The best fit curves for both equations (3.13) and (3.14) yielded values of $m_o^* = 0.01384\pm0.00002\ m_e$ and $g_o^* = -62\pm2$ at 18°K. Extrapolating to zero temperature according to the procedure outlined in section A-iv yielded $m_o^* = 0.01383\pm0.00002\ m_e$. The error was arrived at by taking into account the inherent precision of the spectroscopic system (the resolution was 0.2 cm^{-1} although peak positions could generally be found to within 0.1 cm^{-1}), the accuracy of the magnetic field (0.1%) and the corrections applied (plasma shift, polaron coupling shift and finite aperture effects) as well as the averaging implied by fitting theoretical curves to experimental points. Although m_o^* is commonly called the band edge effective mass it might more

properly be termed the zero-field value for this particular concentration at this temperature, since k_H is not exactly equal to zero.

Using equations (3.13) or (3.14) it was found possible to fit the experimental points over the whole range of magnetic field values. Thus Kane's theory, modified for the presence of a magnetic field as expressed in equations (3.13) and (3.14), was completely adequate within the accuracy of this experiment in predicting the curvature of the conduction band near the zone center. The value of the band edge effective mass derived from the fit compares favourably with those values determined by other authors for samples with similar concentrations (see Table 3.1). It is not certain however what corrections, if any, were applied by the other workers to account for plasma and polaron effects. The agreement of g_o^* with other measured values is not as satisfactory.

Numerous determinations of the effective g factor have been made by various workers in recent years using a variety of techniques. g_o^* values measured in electron spin resonance experiments have consistently been found equal to approximately -51 at low temperatures (McCombe and Wagner, 1971; Isaacson, 1968; Konopka, 1970). On the other hand, Dickey et al (1970) required a g_o^* of -62 in order to fit an equation similar to equation (3.14) to their spin-split cyclotron resonance results. Inaccuracies in equation (3.14) may be the cause of this discrepancy. However g* values measured by McCombe (1969)

Table 3.1 Comparison of band edge electron effective mass and effective g factor obtained by various authors

m_o^* in units of m_e	g_o^*	temperature (°K)	reference
0.01384± 0.00002	-62±2	18	this work
0.0137± 0.0001		15	Summers et al, 1968
0.0139± 0.0001		15-60	Johnson and Dickey, 1970
0.01376	-62	15-60	Dickey et al, 1967
0.0139± 0.0001			Bell and Rogers, 1969

as a function of magnetic field utilizing combined resonance absorption ($\Delta n = 1$, $\Delta s = -1$) yielded, without the aid of elaborate theory, an extrapolated zero field value of approximately -60 at liquid nitrogen temperatures. Thus it appears that g_o^* values determined in cyclotron resonance experiments are consistently smaller than those measured in spin resonance experiments. The reason for this discrepancy is not understood.

iii - Resonant Electron-LO Phonon Coupling

Infrared absorption due to cyclotron resonance transitions in InSb at 48°K is illustrated in Figure 3.5 for three different magnetic fields. At this temperature two spin-split Landau levels are significantly populated and so four relatively sharp cyclotron resonance absorptions are visible. The strongest absorptions involve transitions between Landau levels with n = 0 and n = 1 spin up (the highest frequency absorption) and spin down. The weaker, lower frequency absorptions result from transitions between n = 1 and n = 2 spin-up and spin-down levels. As the magnetic field increases to 15 k0e, this second set of absorptions was seen to decrease in intensity and to broaden slightly. At still higher fields no sharp lower frequency absorptions were observed although a broad weak absorption was evident on the low-frequency side of the main Landau level transitions. The change in electron effective mass as a function of magnetic field for these different cyclotron resonance transitions is summarized in Figure 3.6. The experimental points (circles) for the main Landau level transitions

Figure 3.5: Cyclotron resonance absorption in InSb at 48°K at three different magnetic fields. The two strongest absorptions involve transitions between n = 0 and n = 1 spin up and spin down levels. The two weaker absorptions at smaller frequencies result from transitions between n = 1 and n = 2 spin-up and spin-down levels.

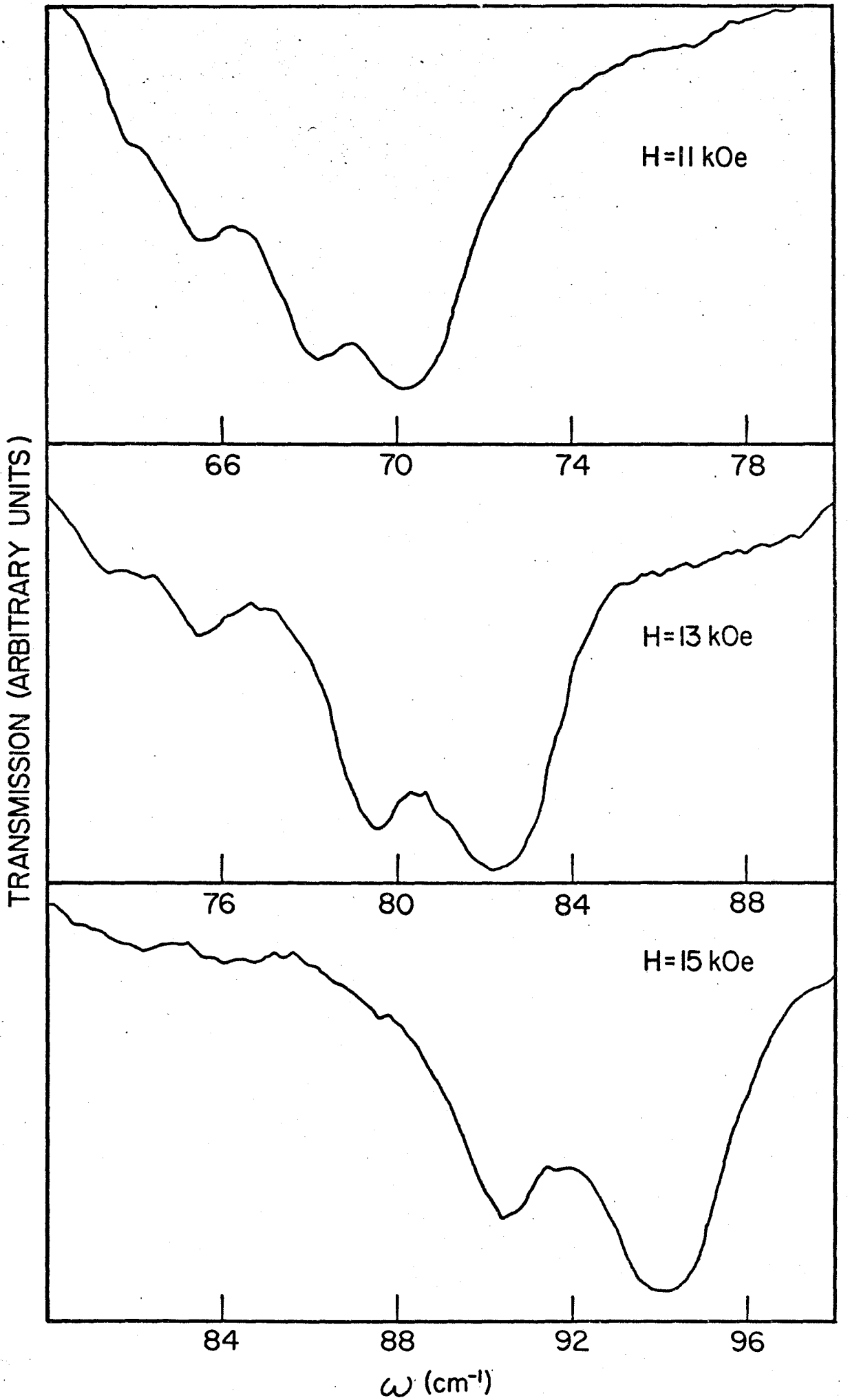
H=11 kOe
66
70
74
78
H=13 kOe
76
80
84
88
H=15 kOe
84
88
92
96
TRANSMISSION (ARBITRARY UNITS)
ω (cm⁻¹)

Figure 3.6: Electron effective mass versus magnetic field in InSb at 48°K. The circles are the experimental points and the solid lines were calculated using Kane's theory (no resonant polaron effects included). The two lower curves were derived from transitions between n = 0 and n = 1 Landau levels (spin up-lowest curve, spin down-next highest curve). The next two curves are for transitions between n = 1 and n = 2 Landau levels with spin-up and spin-down respectively. One point at 9 k0e resulting from a n = 2 to n = 3 spin up transition is also plotted. The dashed lines are Kane's theory modified to include resonant electron-LO phonon coupling.

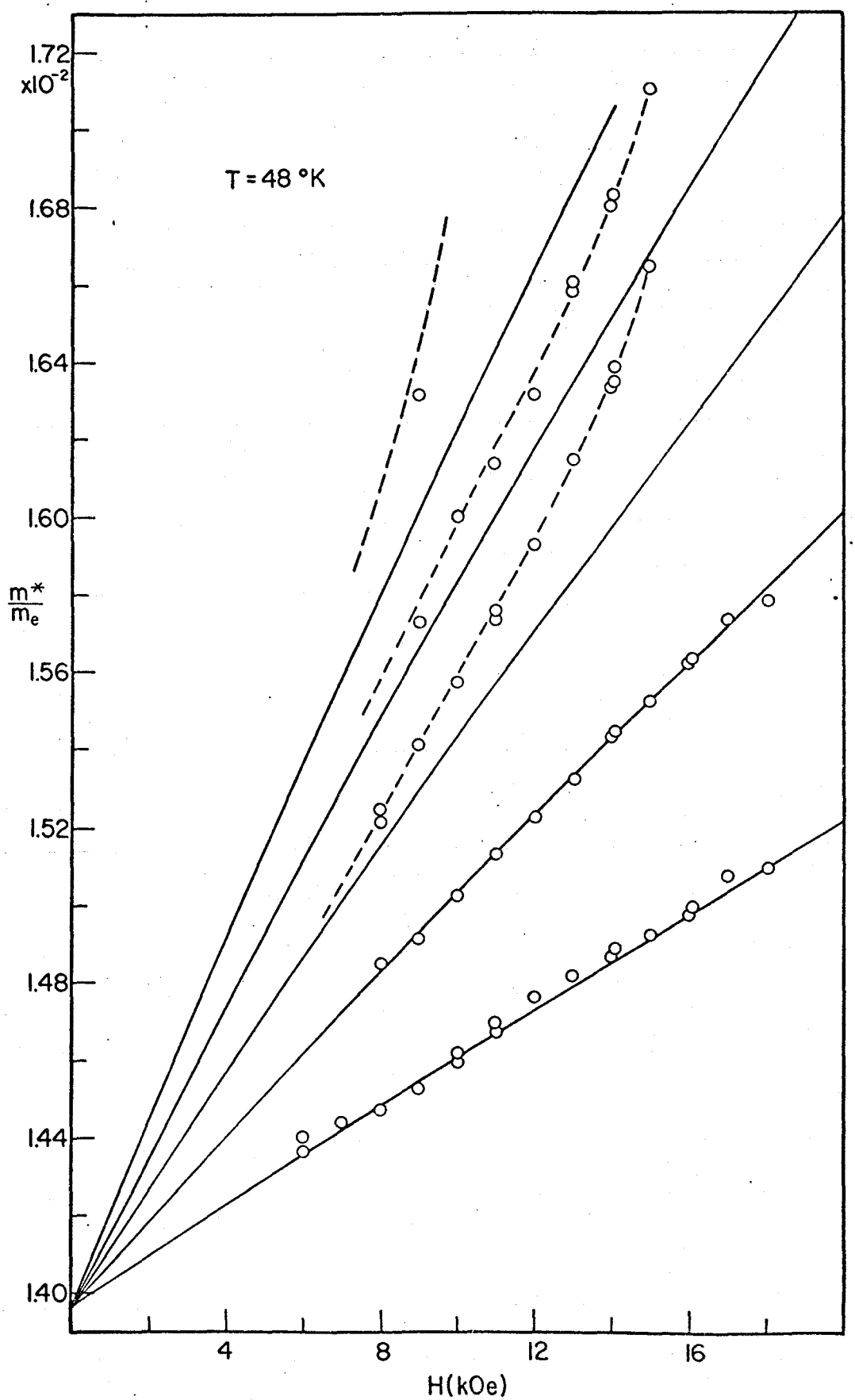
1.72
x10⁻²
1.68
1.64
1.60
m*/mₑ
1.56
1.52
1.48
1.44
1.40
T = 48 °K
4
8
12
16
H(kOe)

were fitted by Kane's theory (solid lines calculated using equation (3.14)). There is a wide discrepancy between experiment and theory for the transitions originating on the n = 1 level. This disagreement is explained in terms of resonant electron-LO phonon coupling between the n = 2 and n = 0 + ω_{LO} levels. Spin-split Landau levels in InSb as a function of magnetic field are illustrated in Figure 3.7. ω_{LO} was measured to be 198.6 cm^{-1} in phonon absorption experiments described in the next chapter. The solid lines were calculated using equation (3.14) and include resonant electron-LO phonon coupling effects. The experimental points (circles) were derived by summing the measured cyclotron resonance energies and the calculated n = 1 Landau level energies (no resonance effects) at each magnetic field. The agreement is good and it is therefore possible to understand qualitatively what is occurring.

As the n = 2 levels approach the n = 0 + ω_{LO} levels, the strength of the electron-LO phonon coupling increases and the levels change shape. The energy differences between the n = 1 and n = 2 levels decrease compared to the zero coupling case and the measured effective masses increase. The magnetic fields at the level crossings for the two spin states are not equal. Furthermore, these cyclotron frequencies, unlike the case for the pinning of the n = 1 level to the n = 0 + ω_{LO} level do not saturate at some constant value. Beyond the crossing they continue to decrease. Because the level crossings of the two-spin states occur at slightly different fields, their cyclotron resonance frequencies do not peak at the

Figure 3.7: Landau levels in InSb as a function of magnetic field at 48°K. The circles are the experimental points derived in the manner described in the text and the solid lines were calculated using Kane's theory and included resonant electron-LO phonon coupling.

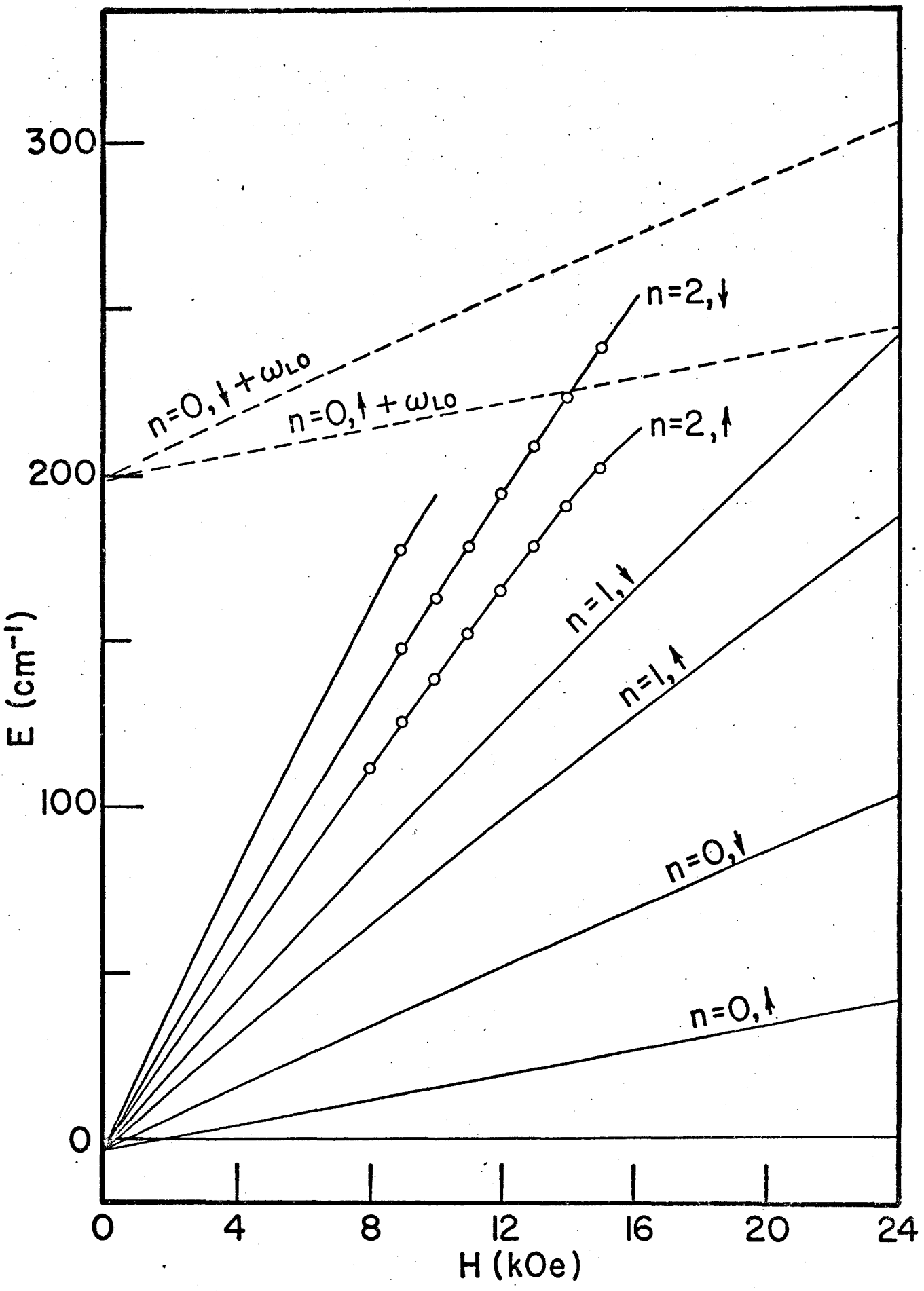
300
200
100
0
E (cm⁻¹)
0
4
8
12
16
20
24
H (kOe)
n=0,↓+ωLO
n=0,↑+ωLO
n=2,↓
n=2,↑
n=1,↓
n=1,↑
n=0,↓
n=0,↑

at the same field value but rather are expected to cross at about 17 k0e. Since each of these cyclotron resonance modes is strongly coupled to the LO phonon in this region, this accidental degeneracy leads to a strong mixing of the states and probably accounts for the premature broadening and weakening of the absorptions observed near 15 k0e. The theory of polaron coupling predicts a decrease in the intensity of these transitions in the resonant electron-LO phonon coupling region. The transition approximately equal to $\omega_c + \alpha\omega_{LO}$ increases in intensity in this region. The energy shifts of these transitions place them on or very near the n = 0 to n = 1 unperturbed transitions and, since, in addition, they are anomolously broadened near the crossing, they are very difficult to observe unambiguously. However, they probably contribute to the low energy shoulder present at large fields ($\geq$ 16 k0e).

In figure 3.7, the experimental points indicate that there is no polaron interaction between states of opposite spin (ie. between the n = 2 spin down and the n = 0 + ω_{LO} spin up levels). This would not be unexpected if only a weak magnetic interaction coupled these states.

Figure 3.8 is a plot of the mass enhancement of the electron effective mass due to resonant electron-LO phonon coupling as a function of magnetic field (in units of ω_c/ω_{LO}'). The experimental points were obtained by assuming that the difference in effective mass between experiment and Kane's

Figure 3.8: Resonant electron-LO phonon mass enhancement in InSb as a function of magnetic field (in units of ω_c/ω'_{LO}). The solid curve was calculated using Larsen's theory (1966) and $\alpha = 0.023$. The closed circles denote experimental effective mass differences for transitions between n = 1 and n = 2 spin up levels, the open circles are for transitions between n = 1 and n = 2 spin down levels and the triangles are for transitions between n = 2 and n = 3 spin up levels. ω'_{LO} was determined to be 95.1 cm^{-1}.

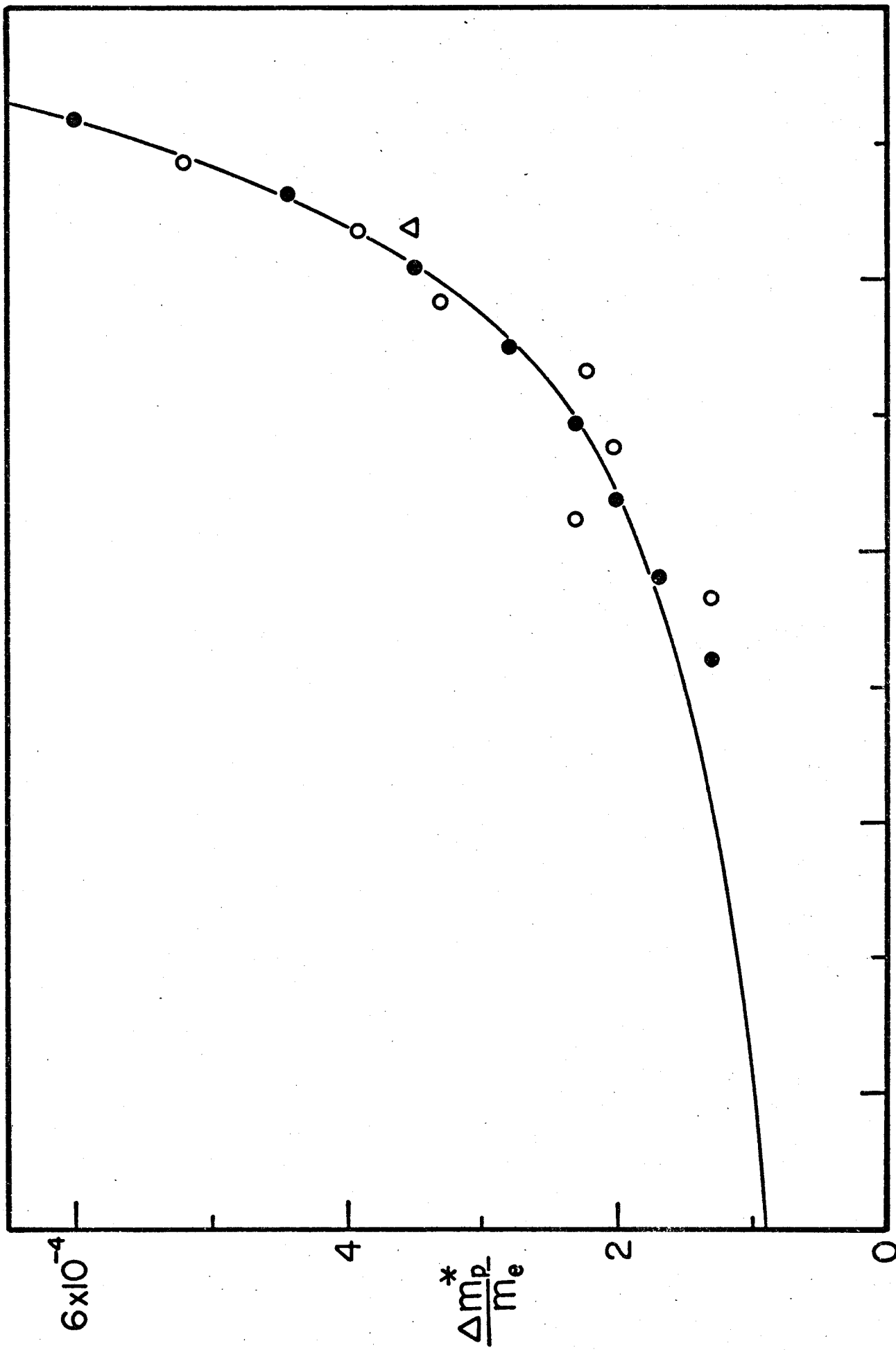
6x10⁻⁴
4
2
0
$\frac{\Delta m_p^*}{m_e}$
0.2
0.4
0.6
0.8
$\left(\frac{\omega_c}{\omega_{LO}}\right)$

theory (equation (3.14) with $\alpha = 0$ and m_o^* and g_o^* determined by fitting the main Landau level transition, $n = 0$ to $n = 1$) was due to resonant polaron coupling. The theoretical curve was calculated employing Larsen's results (1966).

The agreement between experiment and theory is very satisfactory when $\alpha = 0.023$. The fitting error in α is of the order of 1%. Due to the uncertainties in the theory (correct only to order α) the error in α is conservatively set at ± 0.001. This compares with $\alpha = 0.025 \pm .005$ determined by fitting cyclotron resonance linewidth magnitudes (Summers et al, 1968). The value of α obtained here is 15% larger than that calculated using Fröhlich's theory (equation (3.19)). Waldman et al (1969) discovered a similar discrepancy (of the order of 30%) between the measured and predicted value of α in CdTe. Furthermore Nakayama (1969), from theoretical calculations, has suggested that Fröhlich's value for α in InSb may be as much as a factor of two too small.

One experimental point due to the $n = 2$ to $n = 3$ spin-up transition is also included in figure 3.8. Considering the fact that it is a very weak absorption at these temperatures, it falls encouragingly close to the computed theoretical curve.

With the measured value of α, theoretical effective mass versus magnetic field curves were calculated which included mass changes due to both non-parabolicity and resonant electron-LO phonon coupling. These are plotted as dashed lines

in Figure 3.6. The agreement with experiment is very good.

These results effectively demonstrate the capability of this spectroscopic system and the attractiveness of this method of studying resonant-LO phonon coupling. Even in a material with a small coupling constant (such as InSb), easily observed effects permit an accurate determination of the coupling parameter. The presence of the n = 0 to n = 1 transitions, which are not near their level-crossing regions make possible unambiguous determinations of the effective mass change due to non-parabolicity effects alone. Since the level-crossing for these transitions occur at $\omega_c \simeq \frac{1}{2}\omega_{LO} \simeq \omega'_{LO} = 95.1\ cm^{-1}$, the strong Reststrahl band in polar materials may easily be avoided.

iv - Temperature Dependence of the Electron Effective Mass

Figure 3.9 is a composite diagram showing the cyclotron resonance absorptions present in a field of 16.09 kOe at several different temperatures. At the lowest temperature, there is a strong absorption peak on the high energy side of the main Landau transition (between n = 0 and n = 1 spin up levels). This is a cyclotron resonance transition experienced by carriers trapped at impurity sites. It rapidly decreases in intensity as the sample temperature is raised and the impurities are ionized. The weak peak on the low energy side of the main resonance absorption is due to n = 0 to n = 1 spin-down transitions. This absorption increases rapidly in intensity with temperature as the n = 0 spin down Landau level becomes heavily populated. For these main peaks, the absolute magni-

Figure 3.9: Cyclotron resonance absorption in InSb at 16.09 k0e at three different temperatures. The highest frequency absorption, which disappears at high temperature, is due to impurity cyclotron resonance.

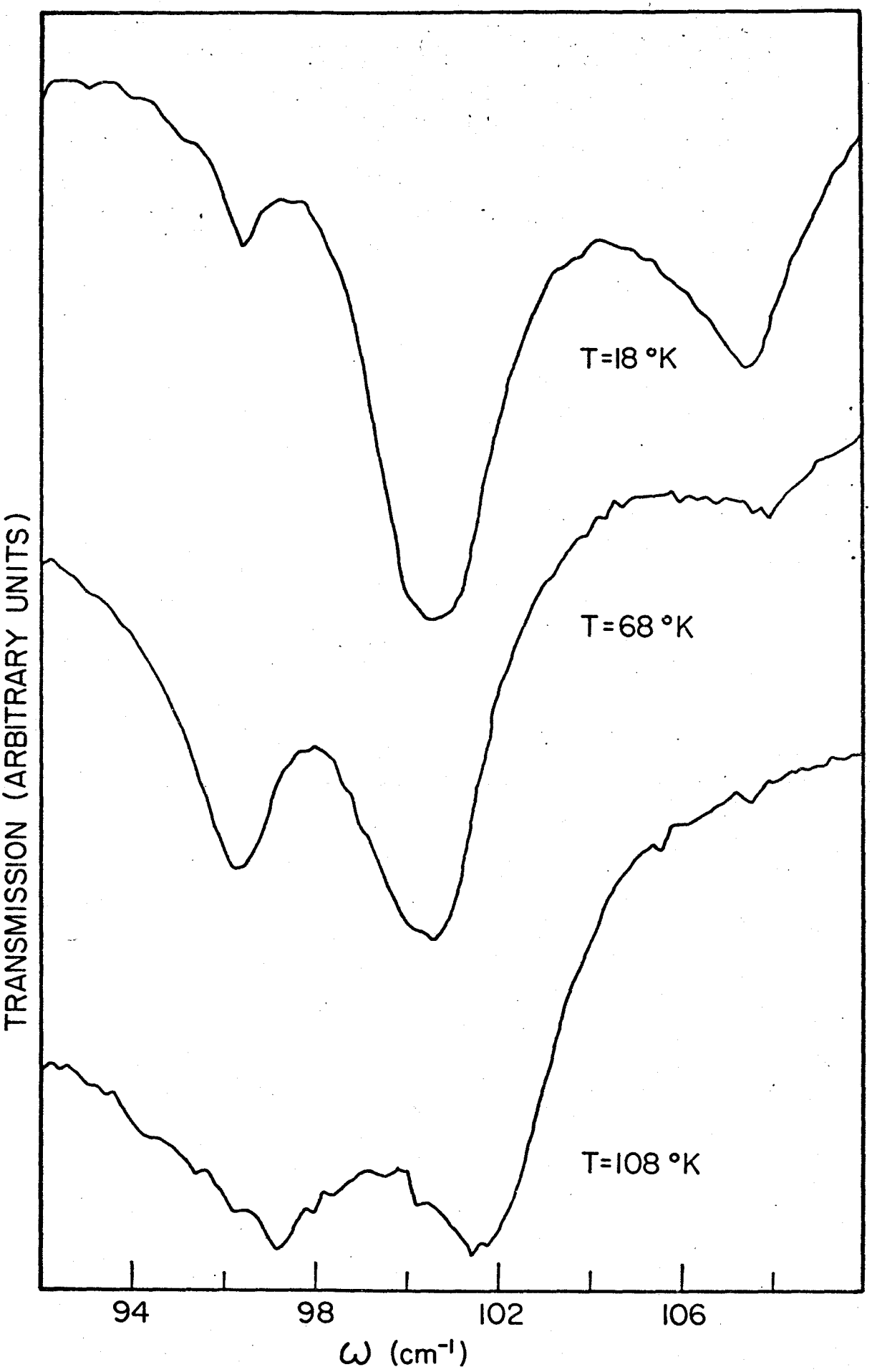
T=18 °K
T=68 °K
T=108 °K
TRANSMISSION (ARBITRARY UNITS)
94
98
102
106
ω (cm⁻¹)

tude of the frequency shifts due to temperature changes is quite small and the error in choosing the peak position increases as the temperature increases and the signal to noise ratio diminishes. To reduce the error, the frequencies of the spin up and spin down transitions at the three values of magnetic field were normalized and then averaged to produce the experimental points shown in Figure 3.10. The theoretical curve was calculated in the manner described previously. There is good agreement between experiment and theory only at low temperatures. The discrepancy at higher temperatures cannot be ascribed to the fact that $k_H \neq 0$ since this would tend to increase the measured effective masses. Neither is the absence of higher band terms in equation (3.11) the cause. Using an equation for the effective mass of the electron at the bottom of the conduction band which includes higher band terms (Kolodzieczak et al, 1966), the theoretical curve was recalculated. No significant difference was found.

The discrepancy appears to be real and so the question of its cause arises. A number of Russian workers have studied the effect of hydrostatic pressure on the electron effective mass in InSb at constant temperature. In effect, they were varying E_g not with temperature but with pressure. In this case the only change in E_g is that brought about by lattice dilation. Itskevich and Sukhoparov (1968) determined effective masses in InSb using magneto-phonon resonance and concluded that Kane's equation underestimated the change in

Figure 3.10: The electron effective mass in InSb as a function of temperature. The circles denote the experimental values and the solid line is the theoretical curve calculated in the manner described in the text. The effective masses are normalized to the largest value present. The error bars are generally 50% larger than the circle diameters unless otherwise indicated.

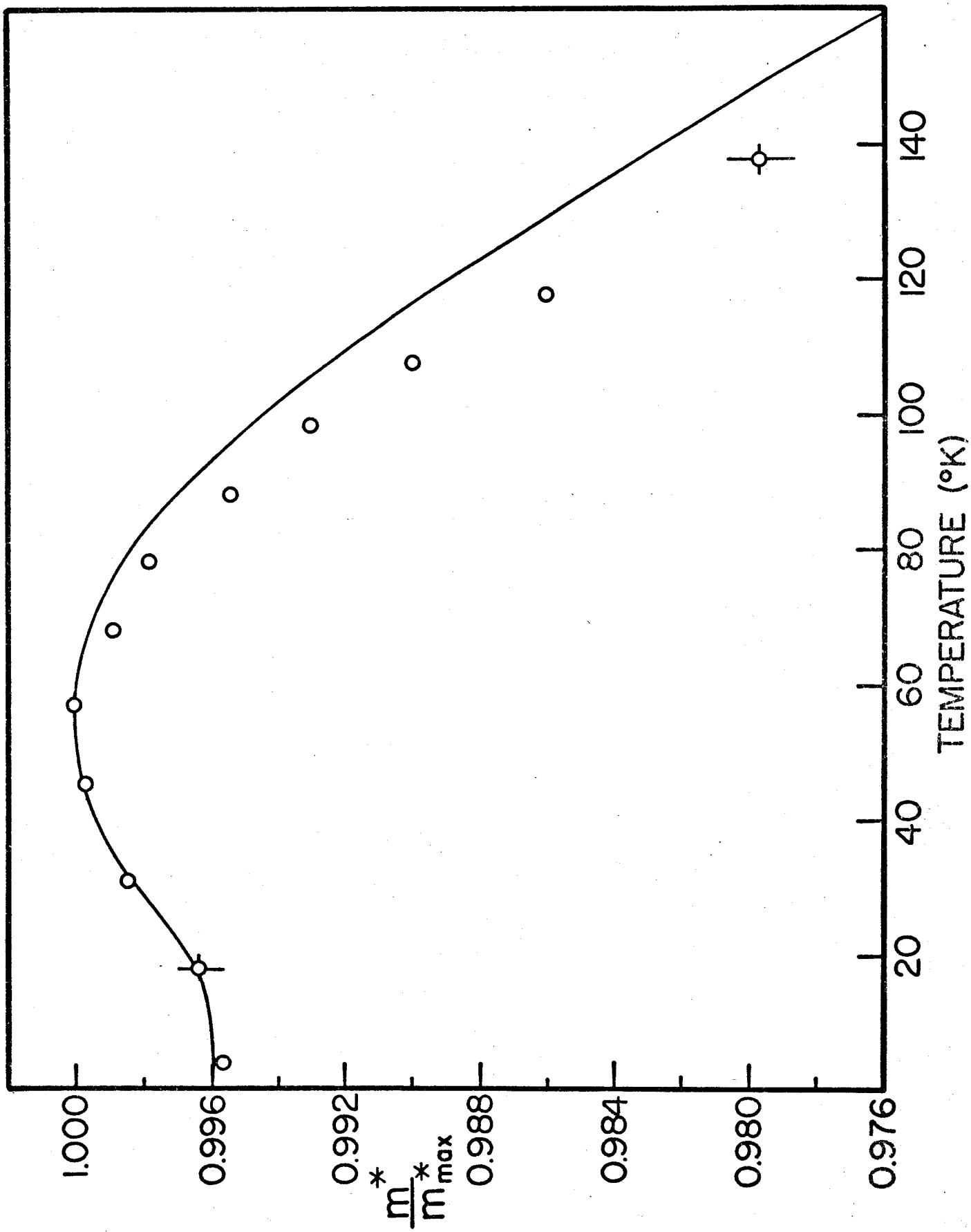
1.000
0.996
0.992
0.988
0.984
0.980
0.976
$\frac{m^*}{m^*_{max}}$
20
40
60
80
100
120
140
TEMPERATURE (°K)

mass due to a change in E_g. The discrepancy in this present experiment is in the same direction and of the same order of magnitude as that of Itskevich and Sukhoparov. However, in a later study (Akselrod et al, 1968), performed using similar but more sophisticated techniques, no discrepancy could be found between experiment and theory. If this is true and Kane's effective mass expression for a rigid lattice must be accepted as correct, then any disagreement in the present experiment must be related to temperature dependent effects. It seems natural to speak of electron-phonon coupling as being the agent by which the mass charge with temperature is enhanced. This is the first term in equation (3.23) which originally was dropped since it was assumed to have a negligible effect on the curvature of the conduction band. With the accuracy achieved in this study it may no longer be possible to neglect it. However, an adequate theory has not yet been developed and some doubt still remains as to the conclusions reached in the pressure experiments. In any case, it has been shown that the main features of the temperature dependence of the electron effective mass can be explained in terms of the dilation of the crystal lattice. This is in agreement with Stradling and Wood (1970). However, there are indications that this might not be the only mechanism.

Finally, employing equation (3.11) and the band edge effective mass measured at 48°K previously, a value of 22.7±0.1 eV was calculated for P^2, the square of the momentum matrix element. This compares favourably with other published

values for InSb (24±1 eV, Johnson and Dickey, 1970; 21.5 eV, Smith et al, 1962; 22.0 eV, Pidgeon and Brown, 1966; 23.8 eV, Bell and Rogers, 1966) determined using a variety of techniques.

CHAPTER IV

LATTICE ABSORPTION

A - THEORY

i - Background

a - Introduction

The study of the lattice modes of vibration of a crystal has a profound significance in interpreting many of the properties of solids, and assists in the deduction of inter-atomic force laws for the crystal. Two main types of interactions are utilized to investigate phonons (quantized lattice modes of vibration); neutron-phonon and photon-phonon interactions. Since thermal neutrons and phonons have energy and momentum of the same order of magnitude, the first type of interaction can be used to probe lattice vibrations over the whole range of these parameters. The limitations of this technique lie in the fact that many crystals have poor neutron scattering properties, instrumentation is expensive and resolution is limited. Photon-phonon interactions are more accurate, less sensitive to the kind of material being investigated and generally easier and faster to study. However as the momentum of the photon is negligible compared to that of a phonon, only interactions resulting in effectively zero net momentum change are possible. This limits the information that can be secured.

The interaction of a radiation field with normal modes of lattice vibrations generally results in one of two effects. There is either the absorption or emission of a photon due to the creation or annihilation of phonons or the scattering of photons by phonons. The latter effect, termed Raman scattering, is related to changes in the electric polarizability of the crystal induced by lattice vibrational modes. The scattered radiation differs from the incident light energy by the frequency of a normal lattice mode. Optical absorption, on the other hand, is attributed to first or second order electric dipole moments or to anharmonic terms in the crystal potential energy. Phonon energies in typical crystals are such that this absorption occurs mainly in the far-infrared region of the spectrum (at frequencies ranging from 50 to 500 cm^{-1} or wavelengths from 200 to 20 microns). Thus, although both Raman scattering and infrared absorption deal with photon-phonon interactions, they do not determine identical quantities and in many cases provide complementary information.

In polar crystals, the first order dipole moment produces extremely strong absorption bands associated with photon coupling with optical modes of essentially zero k-vectors (Reststrahl absorption). Second-order dipole moments and/or third order terms in the potential energy give rise to weaker, higher order optical absorption which involves the simultaneous interaction of the radiation field with two or more phonons. The relative magnitudes of these absorptions can be calculated

with a knowledge of the interactions occurring. Further, group theory can be employed to establish the selection rules for photon-phonon interactions for various symmetry points in given crystal structures.

The introduction of a large number of impurities into a pure crystal causes changes in the simple picture outlined above. The selection rule for single phonon absorption which limits infrared absorption to optical modes at k=0, is broken and the impurities are optically active at frequencies approximating the normal modes of all the vibrations of the host crystal. Depending on the impurity and crystal matrix, non-normal modes may be present which are localized in space or which produce a resonance in the quasi-normal phonon spectrum. The low concentration of impurities in the samples studied in these experiments generally preclude observation of such effects.

b - Dispersion Curves and Critical Points in InSb

Crystals with N atoms per unit cell possess 3N normal modes of vibration of which 3 are acoustic in nature. At k=0 during these latter vibrations, the atoms in each unit cell move in phase with one another, so that there is no net polarization of the lattice.For the 3N-3 other modes, the atoms move in antiphase and, if they are oppositely charged, produce an alternating electrical polarization which can couple with the electric fields of photons.

InSb condenses into a face centered cubic lattice with two atoms per unit cell in a structure called zinc blende. For each wave vector there are 3 optical and 3 acoustic normal modes.

Variations of phonon energy with wavevector are recorded in dispersion curves such as are shown in Figure 4.1 for symmetry directions in InSb. The experimental points were determined by inelastic neutron scattering (Price et al, 1971) and the theoretical curves calculated by G. Dolling (1972) using parameters derived from fitting a shell model theory to the neutron experiment. There are similar diagrams for every direction in $\underline{k}$-space but only along certain symmetry directions are lattice vibrations purely transverse or longitudinal. In addition, in some symmetry directions the transverse modes are degenerate in energy.In general optical modes are only weakly dependent on the momentum ($\underline{k}$) compared to acoustic modes. Frequencies vary with $\underline{k}$, since, as the wavelength becomes comparable to the range of interatomic forces, the restoring forces accompanying the distortions begin to change. The shapes of the dispersion curves therefore serve to determine the ranges of the interatomic forces.

The exact form of the optical spectrum produced by phonon absorption is mainly dependent upon the density of phonon states, the number of lattice modes falling within a small increment of frequency centered on the frequency concerned. It is clear from Figure 4.1 that the important features of any density of states curve must arise from phonon branches whose dispersion curve remains flat over an appreciable distance along the wavevector axis. That is, $d\omega/dk$ is zero. In three dimensions, the density of states curve for a crystal

Figure 4.1: Phonon Dispersion Curves in InSb The circles are the values determined by Price et al (1971) at 300°K by inelastic neutron scattering. The dispersion curves were measured in the $\Delta([00\zeta])$, $\Sigma([\zeta\zeta 0])$ and $\Lambda([\zeta\zeta\zeta]$ symmetry directions.Typical error bars are plotted at (.6,.6,0). The solid lines are the theoretical dispersion curves in the Δ, Σ, Λ and Q (along the (111) plane from L to to W) directions calculated by G. Dolling (1972) according to the procedure described in the text. The curves are labelled according to their vibrational nature near X; TA (transverse acoustic), LA (longitudinal acoustic), LO (longitudinal) optic and TO (transverse optic).

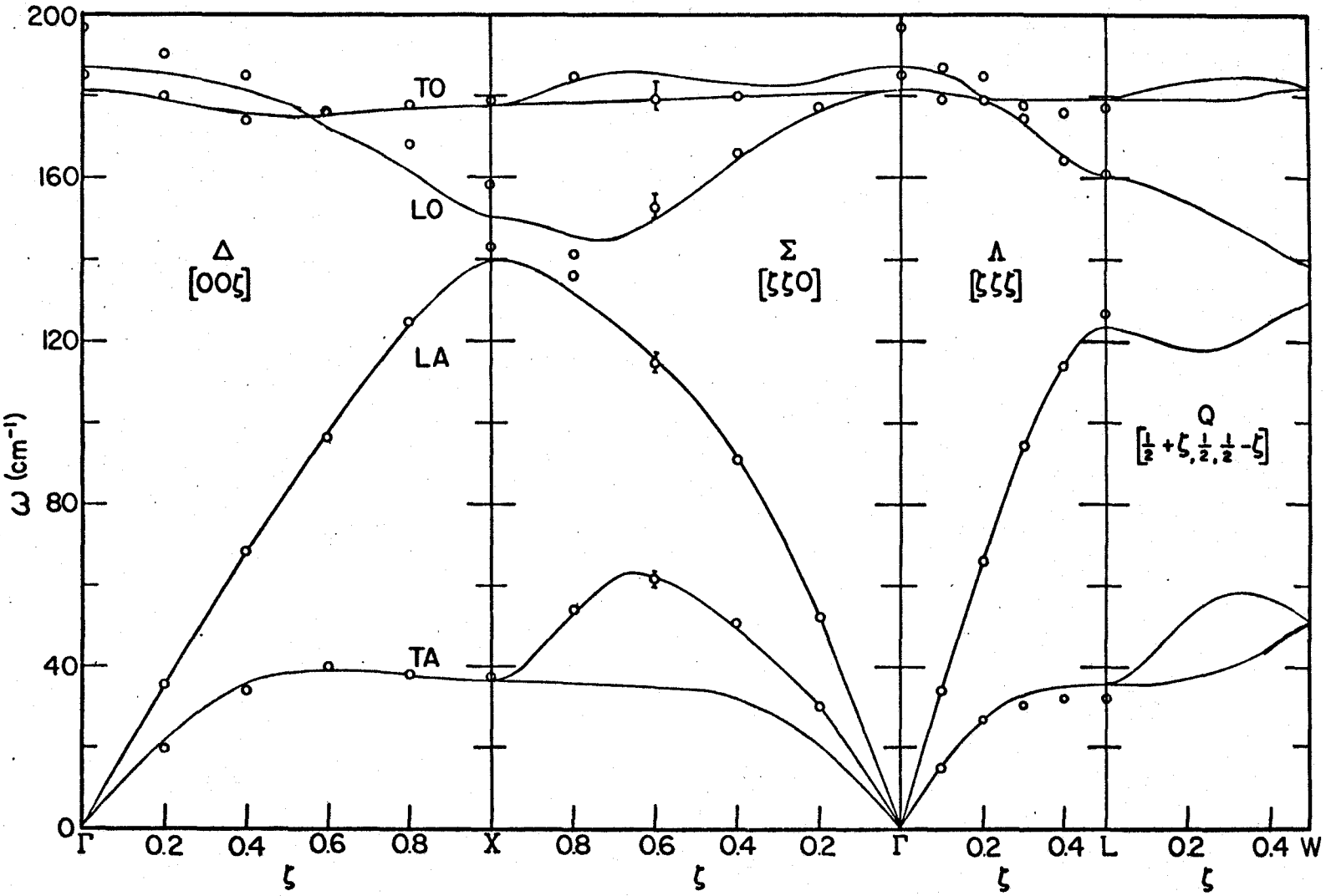
200
160
120
80
40
0
ω (cm⁻¹)
TO
LO
LA
TA
Δ
[00ζ]
Σ
[ζζ0]
Λ
[ζζζ]
Q
[½+ζ, ½, ½−ζ]
Γ
0.2
0.4
0.6
0.8
X
0.8
0.6
0.4
0.2
Γ
0.2
0.4
L
0.2
0.4
W
ζ
ζ
ζ
ζ

exhibits characteristic features at frequencies corresponding to those points in $\underline{k}$ space where grad $\omega(\underline{k})$ is zero for one branch or another. These analytical critical points and the effects they produce on the phonon spectrum were first studied by Van Hove (1953) and then later by Phillips (1956). They explained how the locations in $\underline{k}$-space of most critical points could be determined,by symmetry arguments, from a knowledge of the crystal structure alone. A few others are at places whose precise location requires a knowledge of the interatomic forces. The importance of infrared absorption of phonon modes is that it makes the accurate determination of the critical points of a crystal practical and thus the key points in the dispersion curves.

According to theoretical analysis, most critical points occur at the zone center (k=0) or at specific points on the surface of the Brillouin zone in directions of high symmetry. The Brillouin zone of InSb is a truncated octahedron (Figure 4.2a) and all the phonon branches are expected to possess critical points at the symmetry positions labelled Γ(0,0,0), X(1,0,0), L(0.5,0.5,0.5), and W(1,0.5,0). However, the high resolution experiments described here will demonstrate that some of the most prominent features of the phonon spectrum are produced by critical points at positions of lower symmetry at or near the zone boundary.

The shape of the discontinuity produced in the density of states by a constant energy volume in $\underline{k}$ space depends vitally on the

Figure 4.2(a): The Brillouin zone of InSb. The Brillouin zone of a face centered cubic lattice is a truncated octahedron. Pictured are the principal directions and the points of high symmetry; $\Gamma(0,0,0)$, $X(1,0,0)$, $L(.5,.5,.5)$ and $W(1,.5,0)$.

Figure 4.2b: Discontinuities in the phonon density of states produced by four types of critical points in the Brillouin zone: P_3, a point of maximum phonon energy; P_0, a point of minimum phonon energy; P_2, a saddle point with energy increasing in one principal direction; P_1 a saddle point with energy increasing in two principal directions.

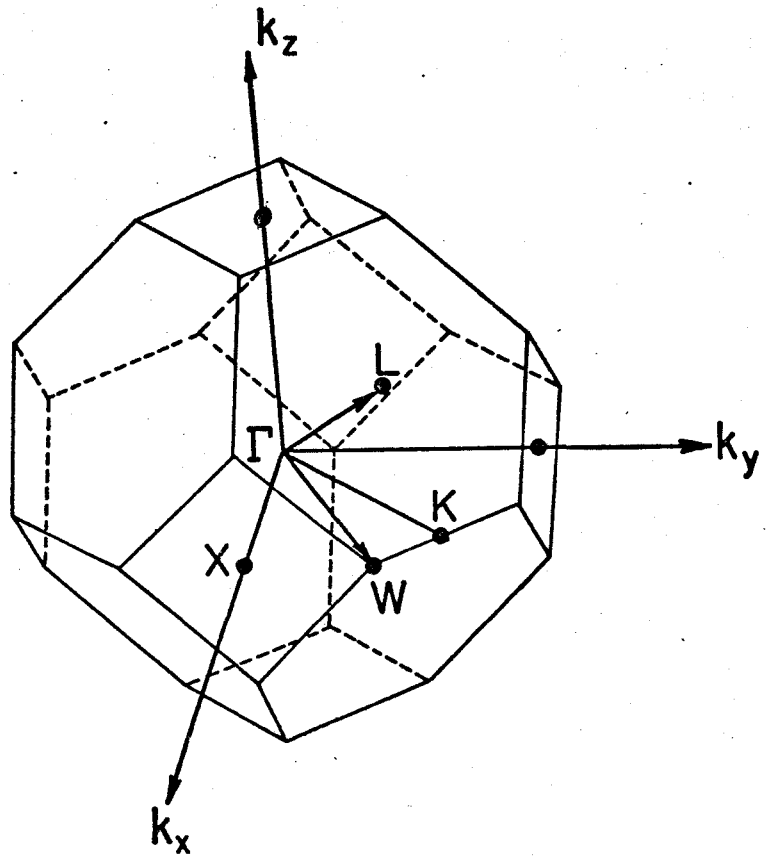

(a)

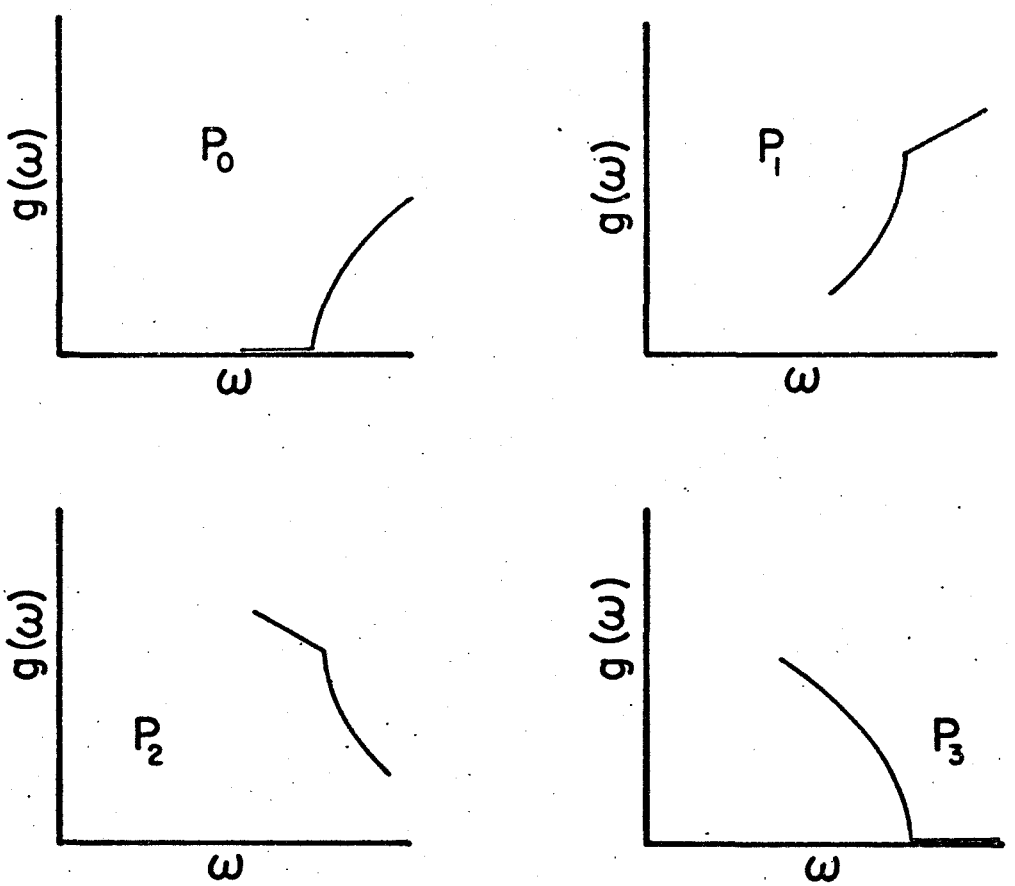

(b)

exact nature of the critical point. Grad $\omega(\underline{k})$ might equal zero at some $\underline{k}$ because $\omega(\underline{k})$ is a minimum in three, two, one or no principal directions. These situations correspond to a three dimensional minimum, two kinds of saddle points and a three dimensional maximum labelled P_0, P_1, P_2 and P_3 respectively. The discontinuities in the density of states associated with these types of critical point are illustrated in Figure 4.2b. Thus it is possible to correlate critical points in $\underline{k}$-space not only with the frequencies but also with the shapes of the resultant discontinuities in the phonon spectrum. However, shape analysis is complicated in multiphonon spectra if a great many combination branches are contributing or if two or more branches contribute simultaneously at the same frequency to produce a composite feature. For example, if one branch has a P_1 type discontinuity and another branch a P_2 type discontinuity at the same frequency, a cusp shaped peak will be present in the phonon absorption spectrum.

ii - Single Phonon Absorption

In pure, polar semiconductors, single phonon absorption is consequence of first order electric dipole moment induced coupling of the infrared photon to the transverse optical phonon at $k \approx 0$. This restriction on the wavevector is necessary in order to conserve momentum as well as energy. While the intensity of this peak is temperature independent, the width is related to the phonon's lifetime which, in turn, is a function of multiphonon decay processes. As the temperature increases

the width of the fundamental Reststrahl absorption also increases.

In transmission experiments in a thick crystal at normal incidence the only phonon mode capable of coupling to the transverse electric field of the photon is the transverse optical phonon at the zone center. However Berreman (1963) predicted that absorption by zone center longitudinal optical phonons was possible in thin crystals at oblique incidence. For samples whose thickness is comparable to optical phonon wavelengths, Berreman showed, starting with Maxwell's equations and matching boundary conditions at the surfaces, that the transmission of the component of light polarized in the plane normal to the crystal, has a minimum when the frequency of light equals the longitudinal optical phonon frequency. Such an absorption has been observed in transmission experiments performed on GaAs (Iwasa et al, 1969) and InSb (Wagner, 1965). The infrared absorption of a longitudinal optical phonon at the zone center under these conditions has been studied as a function of temperature in these experiments. More details on the temperature dependence will be given later.

iii - Multi-phonon Absorption

The weak absorption present in polar materials at frequencies removed from the Reststrahl band is attributed to multi-phonon processes. This is caused by second order electric dipole moments (Geick, 1965; Borik, 1970), the presence of anharmonic terms in the potential energy associated

with lattice vibrations (Cowley and Cowley,1965; Kleinman, 1960) or a combination of both. There is still some discussion at the present time as to the relative magnitudes of these two terms in covalent materials. Identical selection rules and temperature variations of intensities for both mechanisms increase the difficulty of experimentally separating the effects of these two complementary processes although their dependence on frequency is somewhat different. However, in interpreting phonon absorption spectra, the frequency dependence of the coupling mechanism is usually assumed to be so slight and smooth that it can be neglected. Then, any features present are attributed to discontinuities in the phonon density of states resulting from critical points in the Brillouin zone. That this is a reasonable assumption for InSb will be evident from the remarkable resemblance of the observed multiphonon absorption spectrum to the calculated two-phonon density of states. Photon-phonon interactions involving three or more phonons are much weaker than those involving two and they can be ignored in this region of the spectrum.

As with the single phonon-photon interactions, energy and momentum must be conserved in two-phonon interactions. Thus, the sum of the phonon energies and momenta must equal that of the photon.

$$\hbar\omega = \hbar\omega_1 + \hbar\omega_2 \qquad (4.1)$$

and

$$\hbar\underline{k} = \hbar\underline{k}_1 + \hbar\underline{k}_2$$

where ω and $\underline{k}$ are the frequency and wavevector of the photon and ω_1, ω_2 and $\underline{k}_1$, $\underline{k}_2$ the same quantities for the phonons. Since the momentum of a photon is negligible compared with that of typical phonons, only phonon pairs with identical wavevectors may interact simultaneously with the photon. That is,

$$\underline{k}_1 = -\underline{k}_2 \,. \qquad (4.3)$$

In other words, only phonons from equivalent points in the Brillouin zone may interact collectively with the photon. These processes may be additive, resulting in the creation of two phonons or subtractive, resulting in the destruction of one phonon and the creation of another.

Although it is theoretically involved to evaluate precisely the strength of the photon-phonon coupling mechanism for each point in the Brillouin zone, the derivation of selection rules for multiphonon processes at certain symmetry points in the Brillouin zone is relatively straightforward using group theory techniques and coupling mechanism models. The selection rules for two-phonon-photon interactions at certain symmetry points have been derived by Birman (1963) for absorption in the zinc blende structure and are listed in Table 4.1. With the exception of the second harmonics (overtones) of LO and LA modes at the X point, all of the combinations of phonon modes that are possible are allowed at Γ, X and L. Selection rules are only of limited use however because, although they specify whether or not a particular two-phonon

Table 4.1 : Two-phonon processes in far-infrared absorption in zinc blende allowed by electric-dipole selection rules

Symmetry point	Overtones	Combinations
Γ	2LO	LO±TO
(0,0,0)	2LO	
X	2TO	TO±LO
(1,0,0)	2TA	TO±LA
		TO±TA
		LO±LA
		LO±TA
		LA±TA
L	2TO	TO±LO
(.5,.5,.5)	2LO	TO±LA
	2LA	TO±TA
	2TA	LO±LA
		LO±TA
		LA±TA

process is permitted, they provide no information on the strength of the interaction. Further, they have been calculated only at high symmetry points in the Brillouin zone.

The total two-phonon absorption intensity is dependent not only upon the strength of the two-phonon-photon interaction and the two-phonon density of states, but also upon the thermal population of these states. The number, n_i, of phonons of frequency, ω_i, as a function of temperature is given by the Bose-Einstein distribution function.

$$n_i = [\exp(\frac{\hbar\omega_i}{k_B T}) - 1]^{-1} \qquad (4.4)$$

where k_B is Boltzmann's constant. The probability of absorption or emission of one of these phonons is proportional to the square of the matrix element of the phonon creation, a^+ or annihilation, a^-, operator which are given by (Ziman, 1960),

$$\langle\psi(n_i)|a^+|\psi(n_i+1)\rangle = (n_i+1)^{1/2} \quad \text{emission} \qquad (4.5)$$

$$\langle\psi(n_i)|a^-|\psi(n_i-1)\rangle = n_i^{1/2} \quad \text{absorption} \qquad (4.6)$$

where the $\psi(n_i)$ are the phonon wave functions. Therefore the probability of a two-phonon summation process (the absorption of a photon leads to the creation and emission of two phonons) is proportional to $(1+n_1)(1+n_2)$. This must be corrected by subtracting the probability of the reverse process, $n_1 n_2$, the spontaneous emission of a photon and the annihilation of two phonons. The temperature dependence of the net absorption is

then proportional to $(1+n_1)(1+n_2)-n_1n_2 = 1+n_1+n_2$. In a similar manner the temperature dependence of the intensity of the difference process can be shown to be $(1+n_1)n_2 - (1+n_2)n_1 = n_2-n_1$. (Using such an analysis it is obvious that all single phonon processes have a temperature independent absorption.) Thus, the temperature dependence of absorption strengths provides a good method of discriminating between two-phonon sum and difference processes. Summation bands are present at low temperatures and their intensities show a small increase with increasing temperature. Difference bands are absent at very low temperature but are evident at higher temperatures with a strong temperature dependent absorption. Absorption resulting from two-phonon difference processes will be present only at photon frequencies less than the maximum phonon frequency of the crystal ($\sim$ Reststrahl frequency) while absorption due to two-phonon summation processes can occur at all frequencies up to twice the maximum phonon frequency.

Summarizing,the total two-phonon absorption in a crystal is the product of three terms; the strength of the coupling mechanism, the probability of photon-phonon interaction (related to the thermal phonon population) and the two-phonon density of states. In interpreting these absorption spectra, the first term will be assumed to be a slowly and smoothly varying function of frequency. The second can be calculated in a straightforward manner using Bose-Einstein statistics. Thus all of the features on the absorption spectra will be attributed

to discontinuities on the two-phonon density of states. The usual procedure in analysing multiphonon spectra has been to assign, more or less arbitrarily, combinations of symmetry-point phonon energies to these features with the aid of theoretical selection rules, generally without the aid of experimental dispersion curves (see Johnson, 1965, and Spitzer, 1967 for reviews). The validity of this method of analysis is in some doubt. As Spitzer (1963) pointed out, the set of symmetry-point phonon frequencies derived in this manner is not necessarily unique.

The multiphonon spectrum of InSb has been analyzed in this manner by Johnson (1965) and Stierwalt (1966). There is some disagreement between these studies on the values of phonon energies at the symmetry points and indeed some derived energies disagree with the values determined by inelastic neutron scattering (Price et al, 1971). The two-phonon absorption experiments described here were undertaken to help resolve these difficulties. The high resolution spectra measured made it possible not only to locate the positions of features with greater precision than before but also, through shape analysis, to identify the type of critical points that caused them. In addition, phonon density of states curves calculated by G. Dolling (1972) were of great value in the analysis and were used to locate the critical points in the Brillouin zone contributing most of the features of the phonon spectra. Dolling's calculation was based on a shell model,

incorporating second-neighbour short range forces, (Dolling and Cowley,1966) and employed parameters determined by Price et al (1971) from fits to the experimental phonon dispersion curves of InSb.

iv - Anharmonic Effects

When discussed previously, temperature was assumed to affect only the intensity of multi-phonon absorption. This is strictly true only if the lattice potential is purely harmonic. Anharmonic terms lead to important properties of crystals. Examples are thermal expansion and temperature dependent phonon frequencies. The total shift of phonon energy with temperature can be considered the sum of two contributions: lattice dilation and phonon-phonon interactions (Mitra, 1969).

The first term is called "quasi-harmonic" since it depends on temperature only through its effect on the crystal volume or interatomic lattice spacing. In effect, the lattice potential is assumed to remain harmonic although the force constants are modified because of a change in the lattice parameter. This frequency shift could, just as easily, be determined by subjecting the crystal to hydrostatic pressure at a constant temperature. The mode Grüneisen constant, γ_i, which has been defined to characterize this volume dependence of phonon frequencies (Slater, 1939), is given by

$$\gamma_i = -\left(\frac{\partial(\ell n \omega_i)}{\partial(\ell n\ V)}\right)_T \qquad (4.7)$$

where γ_i is the Grüneisen parameter for the phonon mode with frequency ω_i and V is the volume. In the quasi-harmonic

approximation γ_i is constant. By manipulating equation 4.7, it is possible to derive an expression for the temperature dependence of a phonon frequency due to the thermal expansion of a cubic crystal.

$$\omega_i(T) = \omega_i(o)\exp(-3\gamma_i \int_o^T \alpha_T dT) \quad . \qquad (4.8)$$

α_T is the linear coefficient of thermal expansion and $\omega_i(T)$ and $\omega_i(o)$ are the phonon frequencies of the i-th mode at temperatures T and 0°K respectively. To make practical use of equation (4.8), γ_i for the normal modes of vibration must be known. Values of this constant for optical modes at the zone center for some crystals have been measured by various workers employing Raman scattering techniques and pressure (eg. Mitra et al, 1969). Little or no work has been performed, so far, determining the Grüneisen parameters for other modes, such as those at zone boundaries (see Payne, 1964, for an exception). In many cases these are of much more theoretical and experimental interest. For example, the Grüneisen parameter of a TA mode at the zone boundary is expected to be negative in diamond-like materials to which InSb belongs. It has been associated with the anomalous volume coefficient of thermal expansion found in many of these substances (Blackman, 1958; Daniels, 1962).

The second term affecting the temperature dependence of a phonon frequency arises from the interaction of the phonon with all the other phonons present. This is called the anharmonic

term although, in reality, thermal expansion also occurs because of anharmonicity in the lattice potential. The effect of the second term could be isolated from the effect of the first if the phonon frequency shift were measured as a function of temperature at pressures adjusted to keep the crystal volume constant. The mechanism of this interaction involves coupling between vibrational modes through the cubic and quartic anharmonic terms in the lattice potential. The frequency shift is temperature dependent since the interaction probability is sensitive to thermal phonon populations. The cubic and quartic components contribute factors to the energy shift of the same order of magnitude but of opposite sign (Lowndes, 1972). Whether the net effect of these anharmonic lattice potential terms is to increase or decrease the phonon frequency is a function, not only of the frequency and the temperature, but also of the strength of the interaction in the particular crystal involved. Ideally this frequency shift could be determined by measuring both the isothermal pressure dependence and the isobaric temperature dependence of the phonon modes. The contribution of the dilation term to the total shift could then be calculated from the results of the first experiment using equation (4.8) and subtracted from the results of the second experiment. This procedure has been followed in a number of experiments performed mainly on the zone center optical modes in ionic crystals (Chang and Mitra, 1972; Borer et al, 1971;

Anastassakis et al, 1971; Postmus et al, 1968; Jasperse et al, 1966). In most of these crystals the frequency shift attributed to the anharmonic term was found to go through a maximum at low temperatures (about half the Debye temperature) and then to change sign and become increasingly negative for temperatures of the order of and greater than the Debye temperature. No explanation has been given as to why many different materials exhibit the same anomalous behaviour.

Little experimental or theoretical work has been performed in determining or interpreting the temperature dependence of non zone center lattice modes in semiconductors. High resolution multiphonon absorption is an ideal method of studying these modes provided that there is a good deal of confidence in the phonon assignments of the features. The first two steps of a study of the anharmonic effects on phonon modes in InSb have been accomplished. High resolution two-phonon spectra have been obtained and combination phonon modes at specific critical points in the Brillouin zone have been assigned to prominent features with the aid of the detailed two-phonon density of states calculation. Secondly, the temperature dependences of many of these features have been determined over the temperature range, 4°K to 170°K. The final step requires a high pressure system for far infrared optical studies, which will be developed later, to determine the isothermal mode Grüneisen constants for these phonon modes near the zone boundary.

B - OBSERVATIONS

i - Experimental Conditions

As in the cyclotron resonance experiments, two or more absorption spectra taken under identical conditions were averaged to improve the signal-to-noise ratio. Background was eliminated by ratioing with spectra taken with no sample in the beam. Typically, the resolution was 0.2 cm^{-1}. Wedge - shaped samples with an average thickness varying from 50 to 1800 microns were used in the phonon absorption experiments. The thickest was used to observe the weak two-phonon absorption peaks. For the temperature dependence experiments, usable spectra were obtained at temperatures up to 170°K. It was increasingly more difficult to work at higher temperatures since the amplitude of the detector signal deteriorated rapidly with temperature. This was due to a combination of increased absorption by the samples and the effect of heat transfer to the bolometer which degraded its sensitivity.

ii - Single-phonon Absorption

Far-infrared absorption at 20°K by single phonons is illustrated in Figure 4.3 for a thin, wedge sample with a thickness varying between 0 and 75 microns from side to side. The broad absorption centered on 186 cm^{-1} is the Reststrahl band due to the first order dipole coupling of the TO mode at the zone center (Γ) to the infrared photon. The strength of this interaction is evident. It has been estimated that in order to observe a sharp Reststrahl absorption in this material, a sample

Figure 4.3: Infrared transmission in the Reststrahl region. The sample thickness was 50 microns and its temperature was 20°K. Absorption at 208, 214 and 220 cm^{-1} is attributed to two-phonon processes. The general decrease in intensity with frequency is due to a slowly varying background produced by interference in the 12 microns thick beamsplitter.

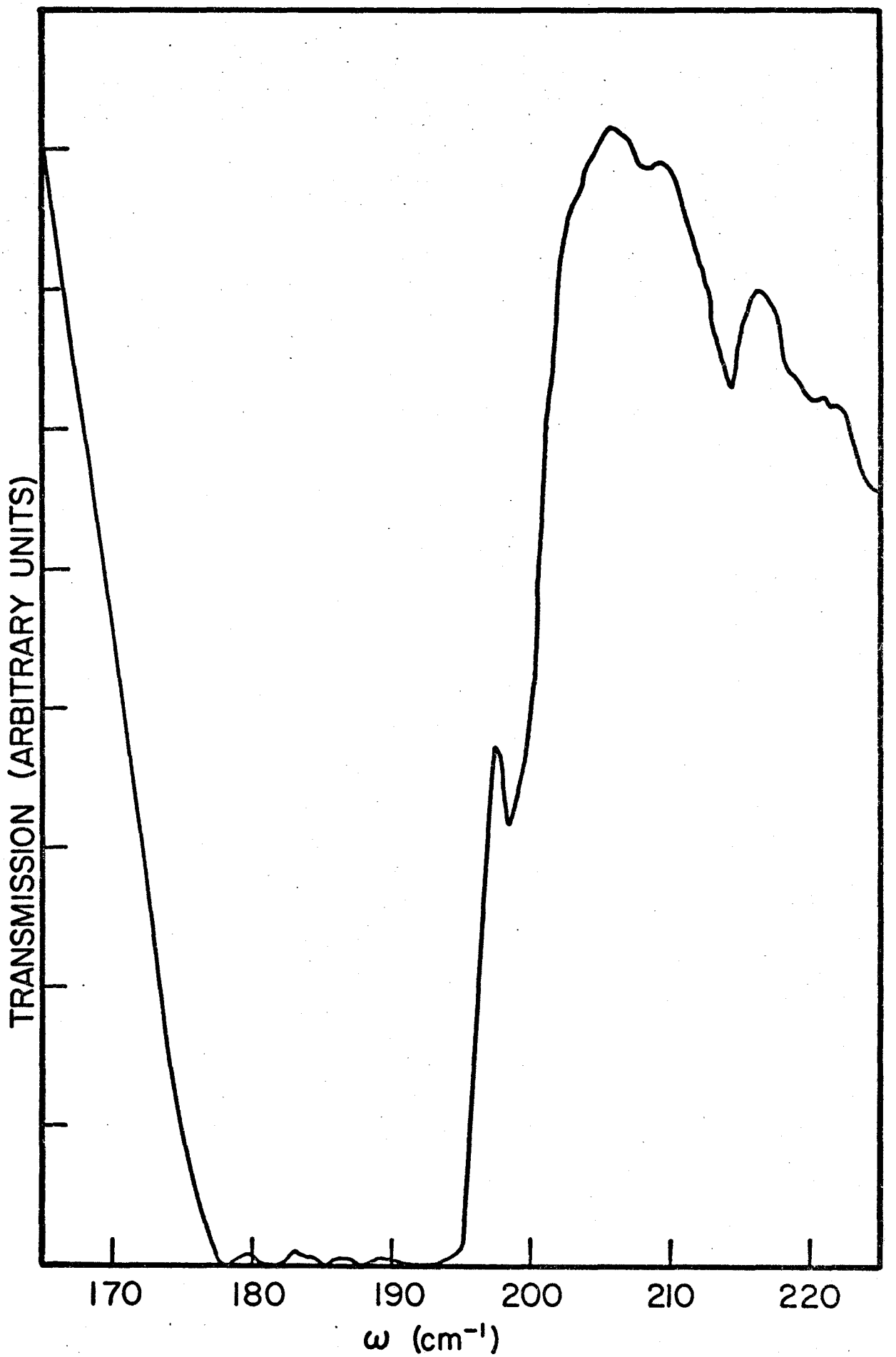
TRANSMISSION (ARBITRARY UNITS)
170
180
190
200
210
220
ω (cm⁻¹)

thickness of one micron is required. Obviously the temperature dependence of the intensity or frequency of such an absorption is impossible to study but it is observed that its width increases with temperature as expected. The asymmetry of this absorption is attributable to anharmonic terms in the lattice potential. A second, relatively sharp and intense (compared to two phonon processes) absorption is seen at 198.6 cm^{-1}. Coupling of the photon to the LO phonon at Γ is considered to be responsible for this feature for the following reasons. The face of the wedge sample was at an angle to the incident light and the sample was thin enough over most of its area so that Berreman's criteria for longitudinal optical phonon absorption was fulfilled. As a function of temperature, this absorption exhibited a behaviour typical of single-phonons. It broadened slightly but did not increase in intensity. (Its slight frequency decrease with increasing temperature will be discussed later.) No strong two-phonon absorption is expected in this frequency region according to the calculated density of states.

These measurements of the values of the frequencies of the optical phonon modes at the Γ point agree well with those obtained from inelastic neutron scattering and most other optical experiments (see Table 4.2)

Another weak absorption peak was observed at 49.6 cm^{-1} with a width of 1 cm^{-1}. Its low frequency and temperature dependence preclude identification of it as a two-phonon mode.

Table 4.2: Values of zone center optic phonon energies determined in various experiments

TO(Γ) (cm^{-1})	LO(Γ) (cm^{-1})	Temperature (°K)	Type of Experiment	Reference
186	198.6±0.1	20	infrared transmission	this work
185±2	197 ±8	296	inelastic neutron scattering	Price et al, 1971
184.7±3	197.2±2	4.2	infrared reflection	Hass and Henvis,1962
180.2±0.1	189.2	300	infrared transmission	Wagner, 1965
180	191	296	Raman scattering	Pinczuk et al 1968
183	194	140		
189.5	205.7	4.2-90	infrared transmission	Johnson, 1965

As a function of temperature, it exhibited little or no frequency shift and no appreciable change in width or intensity. Its origin is still open to speculation but there are indications that it may be a resonance absorption due to neutral impurities in the crystal. The exact number or type of these impurities is unknown but the major impurity present in high grade (99.9997%) antimony is arsenic (about 2 parts per million-Cominco product data sheet). In the absence of a precise theory, unambiguous identifications would require the measurement of absorption spectra of samples doped with various concentrations of a known type of impurity.

iii - Two-phonon Absorption

a - Analytical Procedure

The density of states for single and two-phonon processes was calculated by G. Dolling (1972). The secular lattice equation was solved at a large number of uniformly distributed points in a forty-eighth of the Brillouin zone (at 874 points) and an interpolation scheme was used to determine extra values for phonon energies between these points (Gilat and Dolling, 1964). A total of 139,968,000 frequencies for all the phonon branches in the whole zone were obtained using this procedure. The single phonon density of states was derived in a straightforward manner by counting the total number of frequencies present in each frequency interval. To determine the two-phonon density of states, two-phonon combination energies were formed by adding or subtracting the frequencies

of phonons from different branches but with the same wave-vector, Then, the density of states was calculated in the same manner as in the single phonon case. The second harmonic phonon density of states spectrum (ie. summing phonons on the same branch) is identical to the first with the frequency scale doubled. No selection rules or frequency dependent coupling mechanisms were applied in these calculations.

Dolling's calculations were used to pinpoint the location of critical points in the Brillouin zone. It was assumed that most important critical points were situated on or near symmetry planes. Phonon energies for a particular branch or combination of branches were plotted as a function of wave-vector on a specific symmetry plane and contours of constant energy were drawn (see Figure 4.6). Critical points were located by searching for areas where the energy was a maximum, a minimum or exhibited saddle point behaviour. This critical point analysis was used to investigate 21 two-phonon sum modes and 15 two-phonon difference modes on the (100), (111) and (110) planes.

In agreement with theoretical predictions, critical points for most of the two-phonon branches were discovered at the major symmetry points of the crystal structure; Γ, X, L and W. However, many of these were very weak (the energy was constant only over a small volume of $\underline{k}$-space) and produced no significant features in the density of states. On the other hand, some of the most prominent features resulted from critical points at locations of lower symmetry at or near the zone boundary. In addition, some strong density of states peaks that

were predicted were either very weak or absent in the absorption spectra and some strong absorption peaks that were observed were absent in the calculated curve. In order to clarify this situation, the experimental dispersion curves were utilized. Sum and difference dispersion curves were formed by combining the frequencies of phonons from different branches but with the same wavevector. Several ambiguities involving optic modes were clarified with the aid of these curves. It is evident from a comparison of experimental and theoretical dispersion curves (Figure 4.1) that the overall agreement of the phonon energies in the symmetry directions is good but that the optical modes are generally calculated to be too flat. This would have a tendency to over emphasize combinations of these modes in the computed density of states and lead to a narrowing of overtone peaks.

Another point that should be noted is that the experimental dispersion curves were measured at room temperature. This restricts the validity of the calculated density of states curves somewhat at other temperatures. At low temperatures, where the infrared absorption curves were measured, all the phonon frequencies are slightly larger (about 1 to 2% - see section B-iv).

Finally, although it is strictly correct to speak of transverse and longitudinal modes only in certain symmetry directions, for convenience the phonons will be labelled TO_1, TO_2, LO, LA, TA_1 and TA_2 in order of decreasing frequency

near the zone center.

b - Observations and Discussion

The overall agreement between the observed two-phonon absorption and the calculated two-phonon density of states is remarkably good (Figure 4.4) considering that no use was made of absorption data in the calculations. Not only do the energies of the features generally agree but also their shapes and intensities are in good accord. For the purposes of discussion, the total absorption spectrum will be divided into four sum regions and one difference region and each will be described in detail.

1 - Acoustic Sum Modes

At frequencies less than the Reststrahl frequency ($\sim$ 186 cm^{-1}) the prominent two-phonon sum bands are combinations of TA and LA modes; $2TA_1$, $2TA_2$, $TA_1 + TA_2$, 2LA, LA+TA, and $LA+TA_2$. To make feasible the observation of these weak absorptions a thick sample was required. This had the side effect of producing a strong, wide Reststrahl band on the side of which the combination bands were observed.

The agreement between theory and experiment is less satisfactory in this region than in any other part of the spectrum. This is especially surprising in view of the fact that the fit of the theoretical dispersion curves to the experimental for the acoustic modes in the symmetry directions is exceptionally good (Figure 4.1). In Figure 4.5 the theoretical two phonon density of states curve and the infrared absorp-

Figure 4.4: Comparison of the calculated two-phonon density of states for summation processes with the observed absorption in the frequency range 60 to 380 cm^{-1}. The sample thickness was 1800 microns in the regions 60-200 cm^{-1} and 250 to 380 cm^{-1} and was 250 microns from 200 to 250 cm^{-1}. The temperature was 20°K.

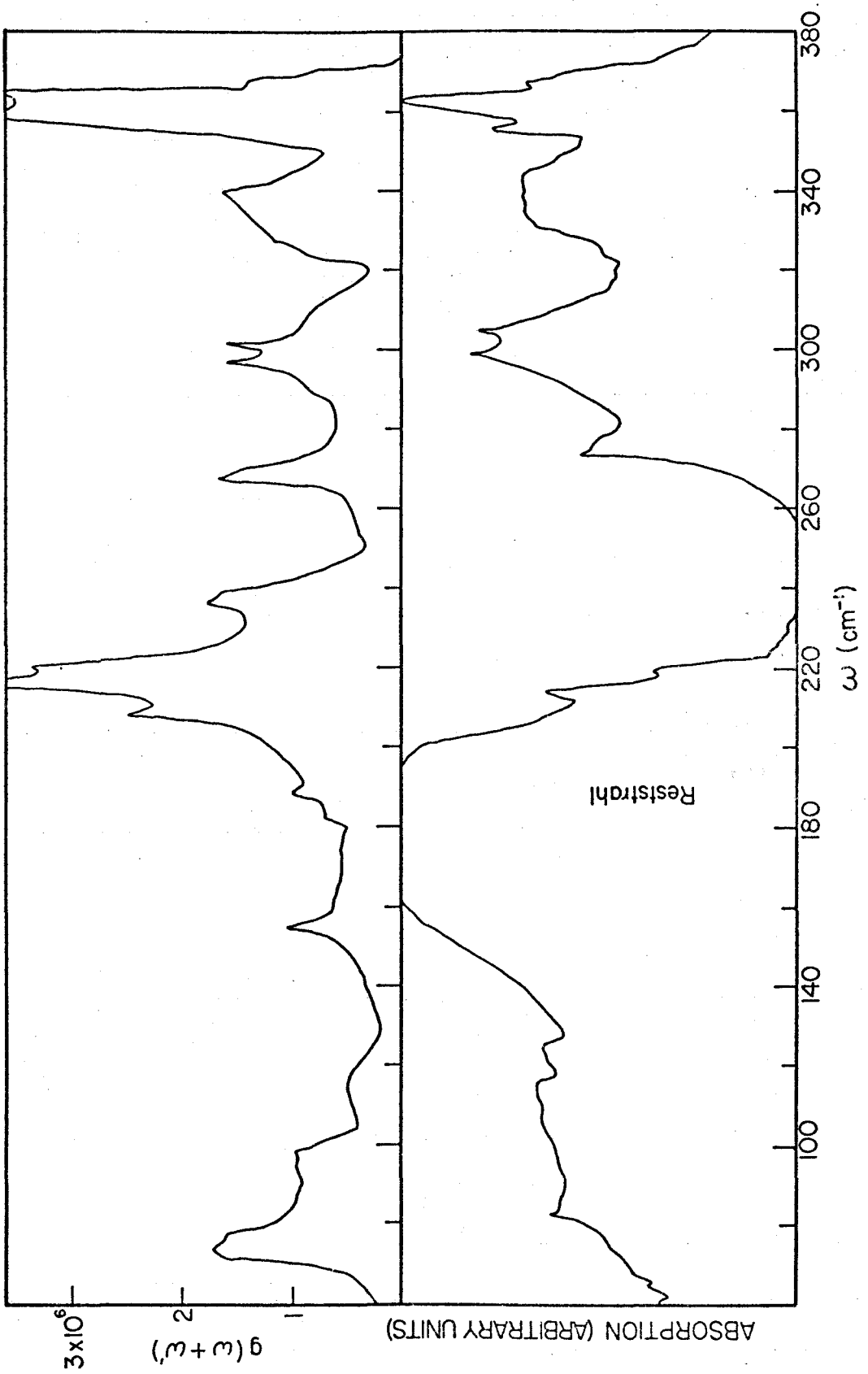
ABSORPTION (ARBITRARY UNITS)
Reistrahl
100
140
180
220
260
300
340
380
ω (cm⁻¹)
g(ω+ω')
1
2
3x10⁶

Figure 4.5: Calculated density of states for two-phonon summation processes compared with the observed absorption in an 1800 micron thick sample at 20°K in the frequency range 50 to 170 cm^{-1}. The two-phonon absorption is modified by the tail of the strong Reststrahl band centered on 186 cm^{-1}. The insert shows absorption in a 250 micron sample due to the $LA+TA_2$ branch.

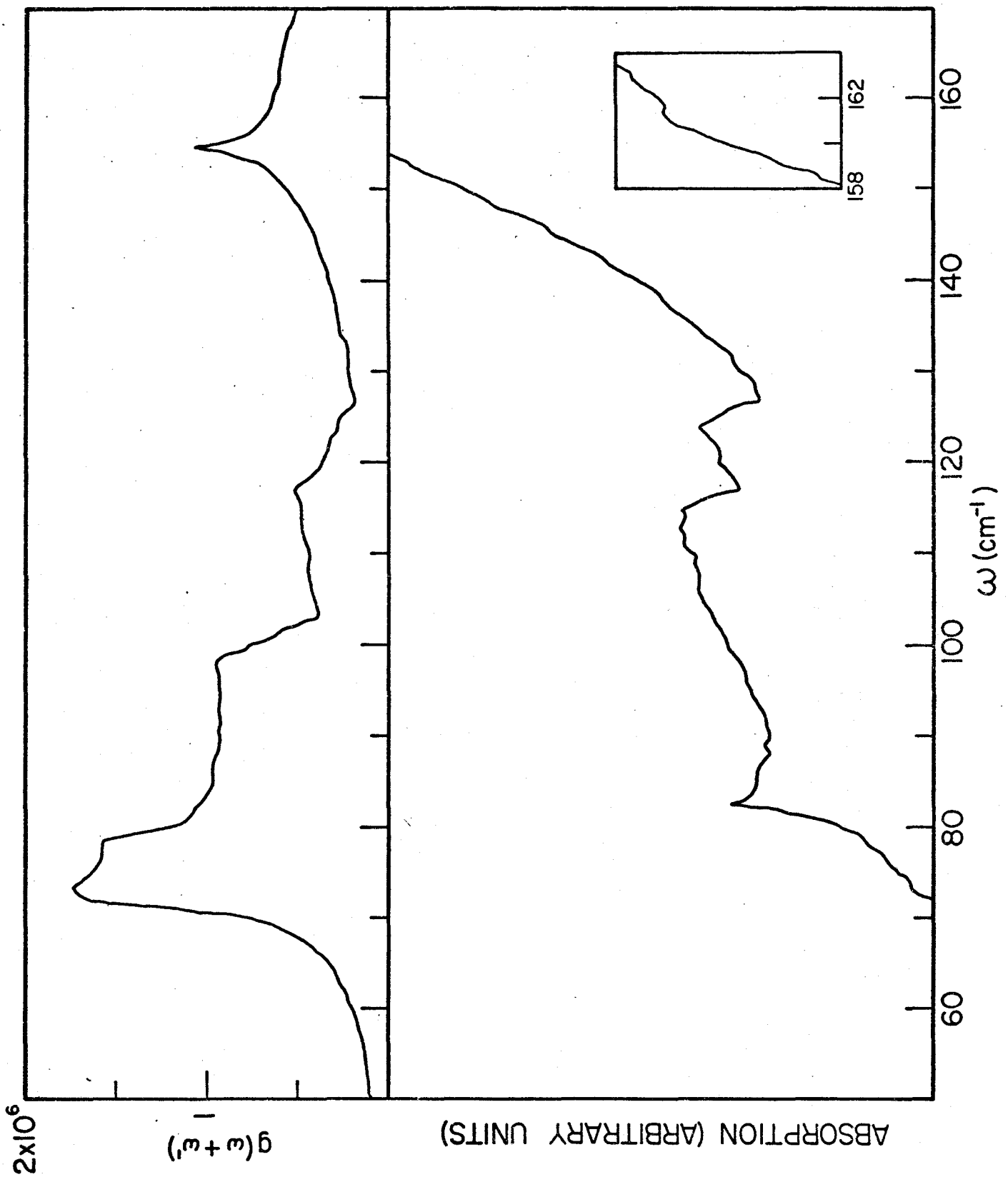
ABSORPTION (ARBITRARY UNITS)
ω (cm⁻¹)
60
80
100
120
140
160
158
162
g(ω + ω')
2x10⁶

tion of a 1800 micron thick sample at 20°K are compared in this region. The agreement of the overall shapes is reasonable. However, the frequencies of the observed features, with the exception of the sudden decrease in absorption at 127 cm^{-1} (attributed to a maximum, P_3, in $2TA_1$ at (.6,.6,0)) are too large. By comparison with the density of states curve, the peak at 124 cm^{-1} is attributed to a $2TA_1$ overtone mode at a critical point (P_2) halfway between L and W on the hexagonal face (111) of the Brillouin zone. Similarly the shoulder that occurs at 115 cm^{-1} is due to a P_2 type critical point in the TA_1+TA_2 combination mode near K (.75,.75,0) and the cut-off that occurs at 117 cm^{-1} is ascribed to a P_3 critical point in the same mode at W (1,.5,0).

The most puzzling feature of the spectrum is the absence of strong absorption bands due to 2TA modes at the L and the X points which the theory predicts should occur at 68-78 cm^{-1}. All that is observed is a small but extremely sharp, peak at 82.6 cm^{-1}, a broad weak shoulder on the high energy side of this peak and a weaker peak on the low energy side (about 75 cm^{-1}). Use of the experimental dispersion curves makes it evident that the sharp peak must be related to the maximum in the transverse acoustic branch located at (.6,0,0). The critical point analysis indicates that one of the degenerate TA modes at this point contributes a type P_1 discontinuity to the phonon density of states and the other a type P_2. The sum of these produces a weak cusp in the density of states at 79 cm^{-1}.

The lack of a strong 2TA absorption attributable to critical points at X and/or L is interesting in that, the TA dispersion curve is relatively flat near these points, the calculated density of states predicts a strong absorption and the selection rules do not forbid it. However, a similar situation has been reported in GaAs (Stolen, 1969) and confirmed in preliminary studies undertaken here. Again there is a strong broad peak predicted in the density of states due to 2TA processes at X and L but only a weak, relatively sharp absorption is observed in the spectrum.

Most of the LA+TA features are predicted to occur at frequencies such that they are hidden by the strong Reststrahl absorption. However, a relatively strong, narrow ($\sim$ 2 cm^{-1}) line is expected at 155 cm^{-1} on the edge of the strong absorption. This is the result of degenerate P_1 and P_2 critical points in the LA+TA_2 branch on the hexagonal face of the Brillouin zone. The energy contours on the (111) and (110) symmetry planes for this phonon combination are illustrated in Figure 4.6. The most interesting feature is a circular valley centered on the L point on the hexagonal face. This is the result of points which have differing wavevectors but similar phonon energies (the minumum values in this plane).

The general shape of this feature conforms to that of the LA mode in this area. The cross section of this type of circular valley may be seen on the theoretical dispersion curve

Figure 4.6: Contours of constant energy for the $LA+TA_2$ combination in the (111) and (110) planes. The (110) plane is pictured in the extended zone scheme. Areas of maximum energy are located at X, L and W. A circularly shaped area of minimum energy is centered on L on the (111) plane. In three dimensions this area consists of saddle points of the first and second type degenerate in frequency but not in position. The frequencies are in cm^{-1}.

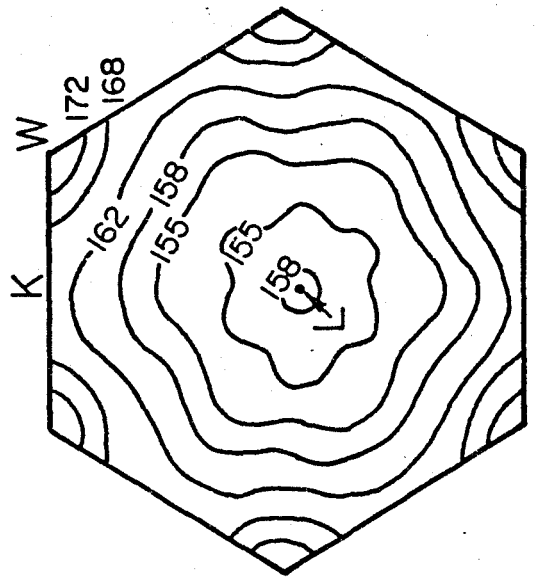
W
K
172
168
162
158
155
155
158
Γ

(111)

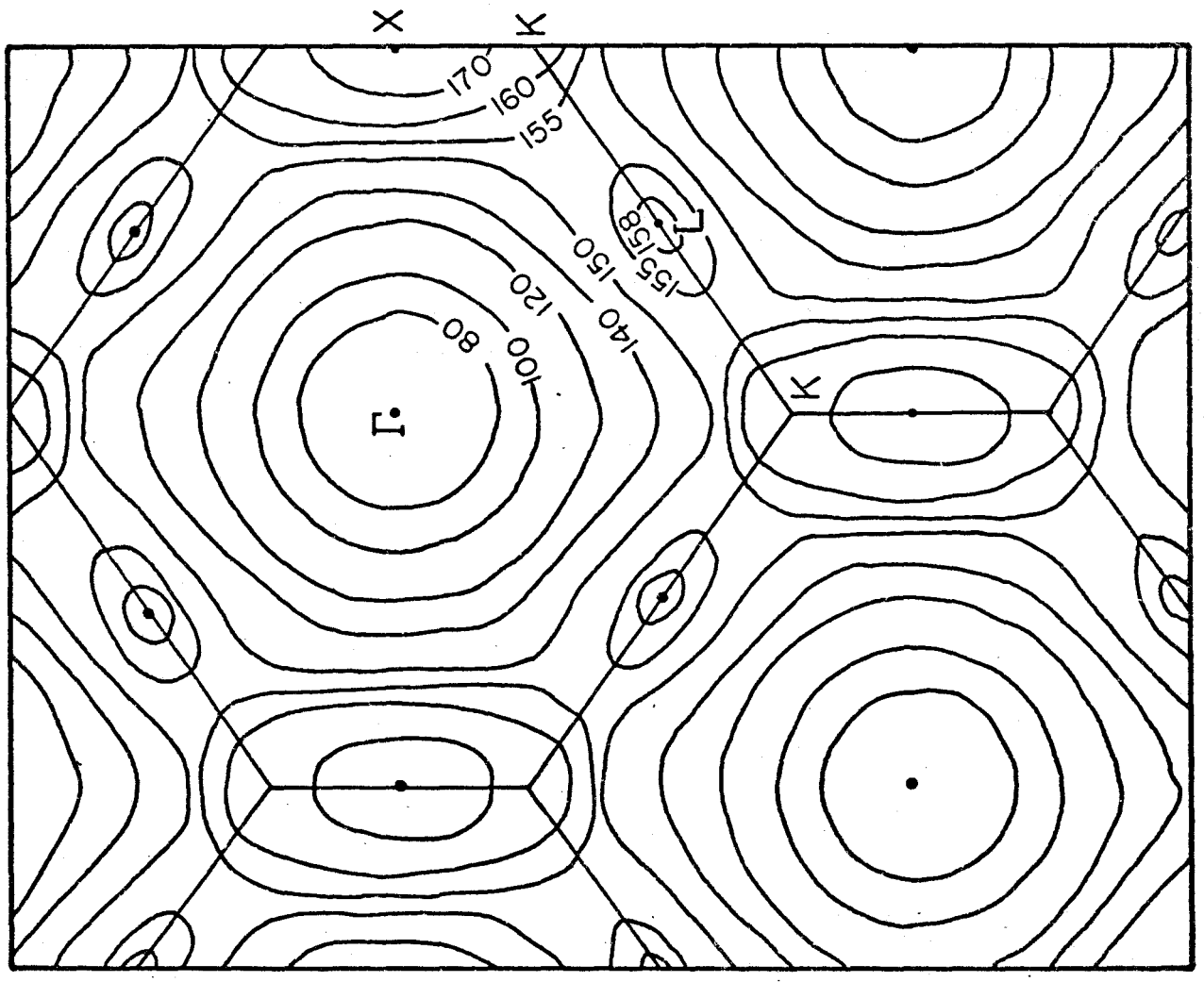
X
K
170
160
155
155158
150
140
120
100
80
Γ
K

(011)

for the LA mode in the Q direction (across the hexagonal face from the L to the W point) (Figure 4.1). From a consideration of the (110) plane in Figure 4.6, it is obvious that movement away from this valley toward L, K or W on the (111) plane results in an increase in phonon energy while movement at right angles to the (111) plane (toward the center of the zone) produces a decrease in energy. Thus the valley is composed of critical points of the saddle point type. Since not all portions of this valley have identical energies, this leads to the following interesting situation. If one moves along this valley from one place to another, a move upward in energy indicates a saddle point of the first type, P_1, while a move downwards in energy identifies a P_2 critical point. Both are equally likely. The cusp-like shape at 155 cm^{-1} is thus formed by critical points in the LA+TA_2 branch that are degenerate in energy but not necessarily in momentum. Several other sharp features at higher and lower frequencies result from similar situations. The search for this feature in the experimental spectrum was complicated by the strength of the Reststrahl absorption but by averaging eight runs for a slightly thinner sample it was finally discovered at 161 cm^{-1} (see insert, Figure 4.5). By subtracting the sloping Reststrahl absorption it was possible to ascertain that the peak was of the expected width ($\sim$ 1.5 cm^{-1}) and strength.

Table 4.3 contains a summary of the features in this region of the spectrum and their assignments.

Table 4.3: Assignment of two-phonon summation processes in the region 50 to 170 cm^{-1}

Experimental Feature			Assignment		
				Critical point location	
position (cm^{-1})	shape	strength	Combination	theory	experimental dispersion curves
75	peak	weak	2TA	X and/or L	L
82.6	P_1+P_2	sharp medium	2TA	(.6,0,0)	(.6,0,0)
84.5	peak	broad weak			
115	P_2	medium	TA_1+TA_2	K	
117	P_3	medium	TA_1+TA_2	W	
124	P_2	medium	$2TA_1$	hexagonal face	
127	P_3	medium	$2TA_1$	(.6,.6,0)	(.6,.6,0)
161	P_1+P_2	medium	$LA+TA_2$	hexagonal face	

2 - Transverse Acoustic Plus Optic Sum Modes

The Reststrahl absorption also hinders the observation of the transverse acoustic plus optic sum modes but, as these are relatively strong the effect is not as serious as in the case of the $LA+TA_2$ mode. Figure 4.7 shows this portion of the absorption spectrum (extending from about 200 to 250 cm^{-1}) and the calculated two phonon density of states due to TO_1+TA_1, TO_1+TA_2, TO_2+TA_1, TO_2+TA_2, $LO+TA_1$, $LO+TA_2$ and 2LA modes. As most of the prominent features result from critical points which occur at symmetry points or along symmetry axes, the transverse modes are degenerate and it is possible to speak principally of TO+TA modes. Most of the features will be assigned with reference to the measured dispersion curves when dealing with optic mode combinations (see section B-ii-b4). However many of the assignments are confirmed by critical point analysis. The strongest peaks, visible even in the 50 micron sample (see Fig. 4.5) occur at 213.5 cm^{-1} and 218.6 cm^{-1} and are due to critical points in the TO+TA branch at the L point and (.6,0,0) respectively. There are shoulders present in both of these peaks due to a $LO+TA_1$ mode (214.4 cm^{-1} from (.2,.2,.2)) and a TO+TA mode (220 cm^{-1} from the X point) respectively. Other weaker features occur at 225 cm^{-1} and 240 cm^{-1}. Also contributing is a weak 2LA mode at 246.2 cm^{-1} due to degenerate P_1 and P_2 critical points on the (111) plane resulting from a situation similar to the one described above for the $LA+TA_2$ branch. In fact, most of the combination modes

Figure 4.7: Calculated density of states for two-phonon summation processes compared with the observed absorption in an 1800 micron thick (a) and a 250 micron thick sample (b) at 20°K in the frequency range 200 to 250 cm^{-1}. The two-phonon absorption is modified by the strong Reststrahl band centered on 186 cm^{-1}.

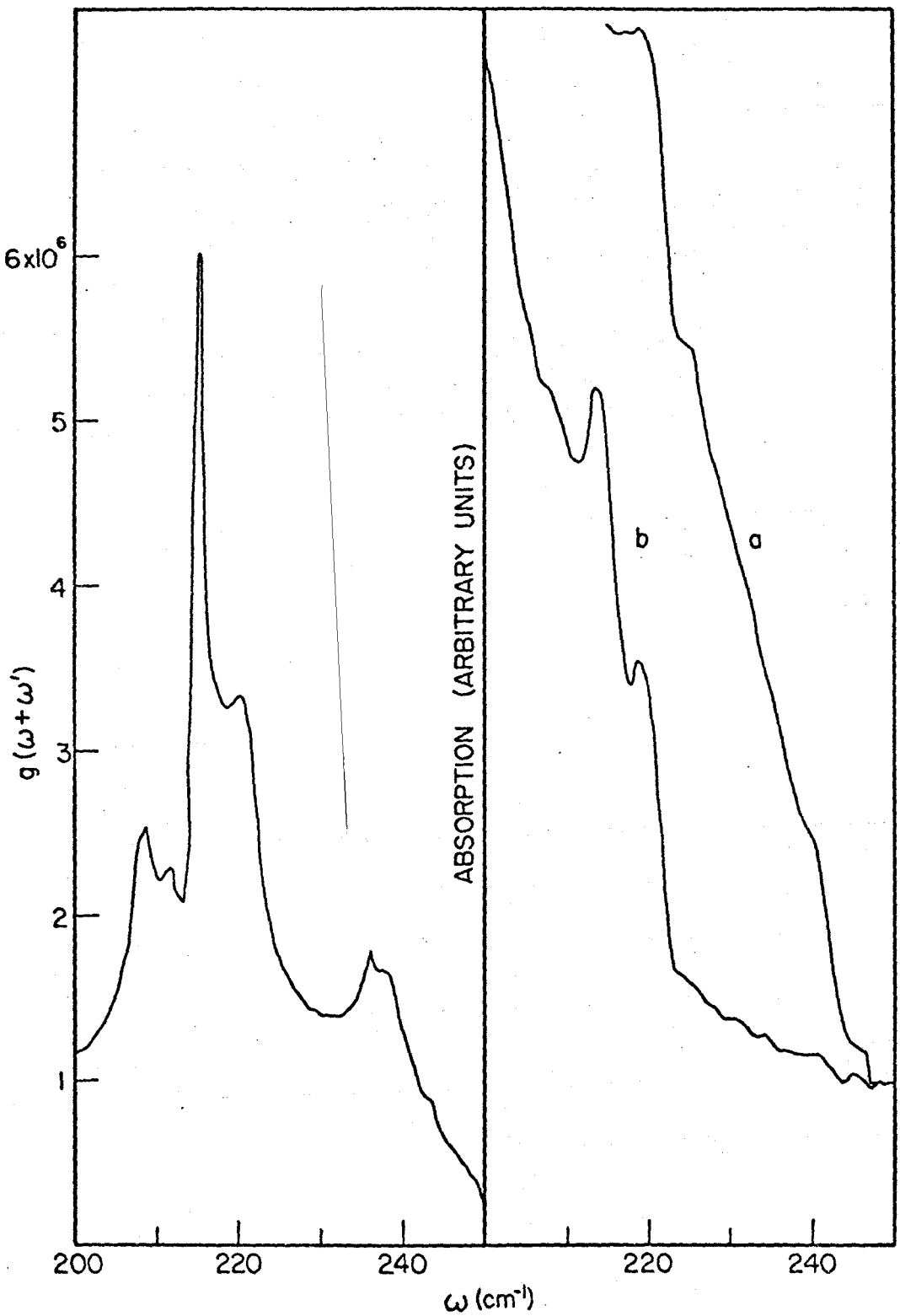
6x10^6
5
4
3
2
1
g (ω+ω')
200
220
240
ω (cm⁻¹)
ABSORPTION (ARBITRARY UNITS)
b
a
220
240

Table 4.4: Assignments of two-phonon summation processes in the region 200 to 250 cm^{-1}

Experimental Feature			Assignment		
				Critical point location	
position (cm^{-1})	shape	strength	Combination	theory	experimental dispersion curves
208.1	P_1+P_2	medium			
211.2	P_1+P_2	weak			
213.5	P_1+P_2	strong	TO+TA	X	L
214.4	P_1+P_2	strong	$LO+TA_1$	near K and (.25,.25,.25)	(.2,.2,.2)
218.6	P_1+P_2	strong	TO+TA	(.6,0,0)	(.6,0.0)
220	P_1+P_2	strong	TO+TA	L	X
225		weak	$LO+TA_1$		(.4,0,0)
					(.5,.5,0)
240		very weak	$TO_{1,2}+TA_1$	near K and W	K
246.2	P_1+P_2	weak	2LA	hexagonal face	

to which LA contributes have this same feature and it is evident that the LA mode imposes its behaviour on the combination mode (see next section).

A complete listing of the features and their assignments is given in Table 4.4.

3 - Longitudinal Acoustic Plus Optic Sum Modes

The features due to the LO+LA, TO_1+LA and TO_2+LA sum modes are shown, in Figure 4.8, to occur in the region from 250 to 320 cm^{-1}. The LA mode, which is a strong function of $\underline{k}$, imposes its behaviour on the weakly varying optic modes to produce the sharp peak visible at 273.2 cm^{-1} and the narrow twin peaks centered on 300 cm^{-1}. A study of the energy contours on the (111) plane of the TO_1+LA and TO_2+LA branches reveals a situation analogous to that for the LA+TA_2 mode. A circular valley is formed on the hexagonal face and this results in degenerate P_1 and P_2 critical points. The transverse optic modes are not degenerate on the (111) plane and so two peaks, equally sharp, are produced.

In the case of the LO+LA branch, a large volume of $\underline{k}$-space near the zone boundary, was found to be relatively stable in frequency. It appears that two-thirds along a line joining the L and W points on the hexagonal face there is a P_1 type critical point which produces the dramatic onset of absorption observed at 273 cm^{-1}. The overall shape of the peak is the result of an averaging process over a great many points in this region of $\underline{k}$-space.

Table 4.5 contains the summary of this analysis.

Figure 4.8: Calculated density of states for two-phonon summation processes compared with the observed absorption in an 1800 micron thick sample at 20°K in the frequency range 250 to 330 cm^{-1}.

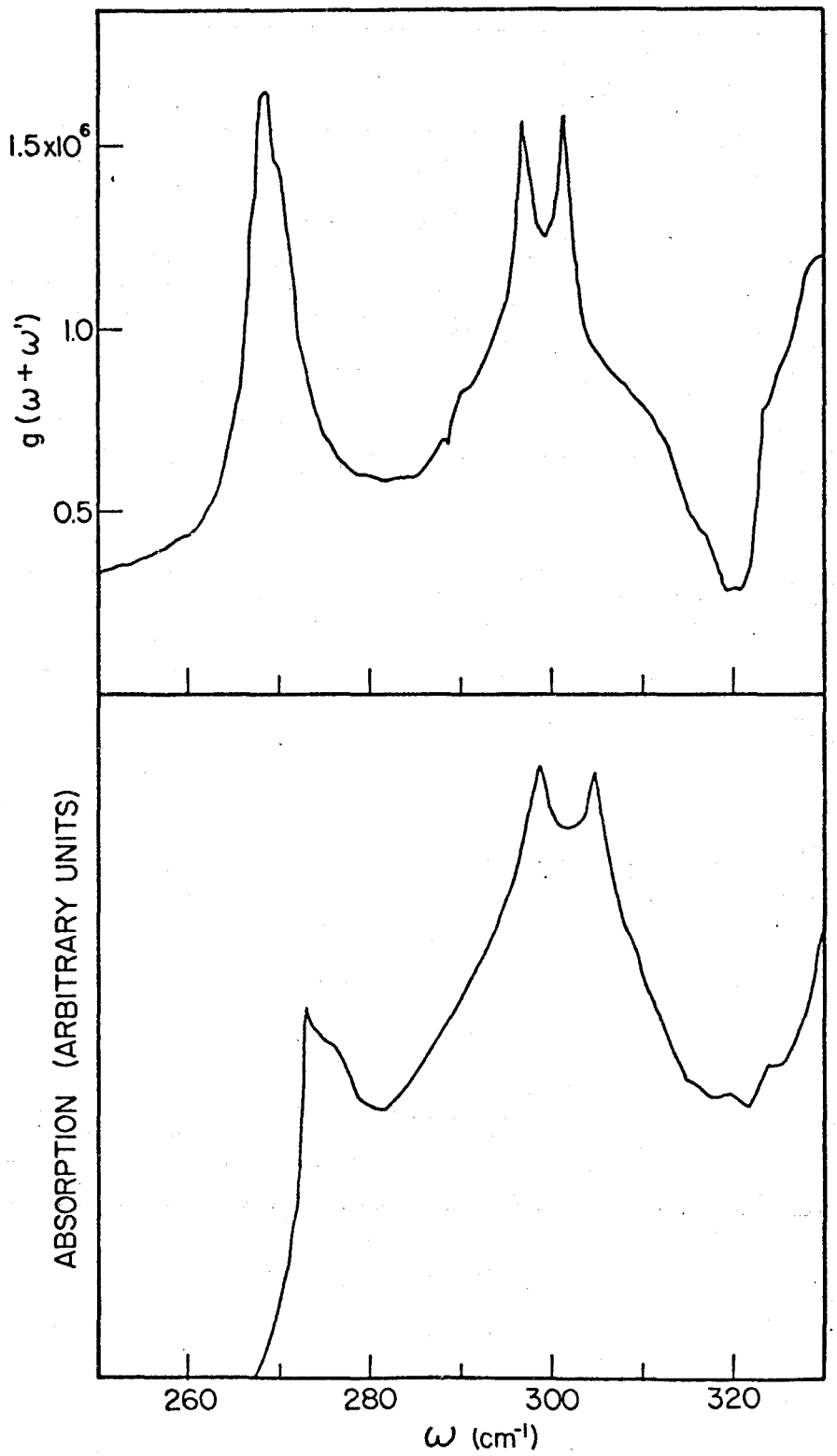
1.5x10^6
1.0
0.5
g (ω + ω')
ABSORPTION (ARBITRARY UNITS)
260
280
300
320
ω (cm⁻¹)

Table 4.5: Assignment of two-phonon summation processes in the region 250 to 320 cm^{-1}

Experimental Feature			Assignment		
position (cm^{-1})	shape	strength	combination	Critical point location: theory	Critical point location: experimental dispersion curves
273.2	P_1	very strong sharp	LO+LA	hexagonal face	
273.2	P_2	strong	LO+LA	near W	
277.6	P_2	medium	LO+LA	near K	
298.8	P_1+P_2	strong sharp	TO_2+LA	hexagonal face	
305	P_1+P_2	strong sharp	TO_1+LA	hexagonal face	

4 - Optic Sum Modes

Combinations of TO and LO modes produce infrared absorption bands at frequencies ranging from 320 to 400 cm^{-1} (Figure 4.9). The discrepancy between experiment and theory expected in this region because of the flattening of the optic modes in the calculation is not as serious as was feared. The principal difference appears to be the absence, in the calculated density of states, of a strong subsidiary peak (at 355.5 cm^{-1}) of the main peak at 362.7 cm^{-1}. The broad mesa-like absorption, ranging from about 330 to 345 cm^{-1} is the result of combinations of LO and TO modes at various places throughout the zone. The cut-off in absorption at 344.8 cm^{-1} is due to a P_2 critical point at L according to critical point analysis. Overtones of TO branches produce the absorption present at 350 to 380 cm^{-1}. Again, according to the critical point analysis, the hexagonal face is an important region of the Brillouin zone for it produces the main peak at 362.7 cm^{-1} and a weak shoulder at 370 cm^{-1}. The subsidiary peak at 367 cm^{-1} can be attributed to critical points at W and K. However, the overall picture is complicated and some doubts exist as to its validity because of the theoretical problem related to the flattening of the optic modes. Therefore the experimental dispersion curves were studied in an attempt to clarify the situation. All the important directions in $\underline{k}$ space could be investigated except the hexagonal face. This analysis identifies the main peak at 362.7 cm^{-1} as due to 2TO modes at the X point, the low energy shoulder (noticeable

Figure 4.9: Calculated density of states for two-phonon summation processes compared with the observed absorption in an 1800 micron thick sample at 20°K in the frequency range 320 to 380 cm^{-1}.

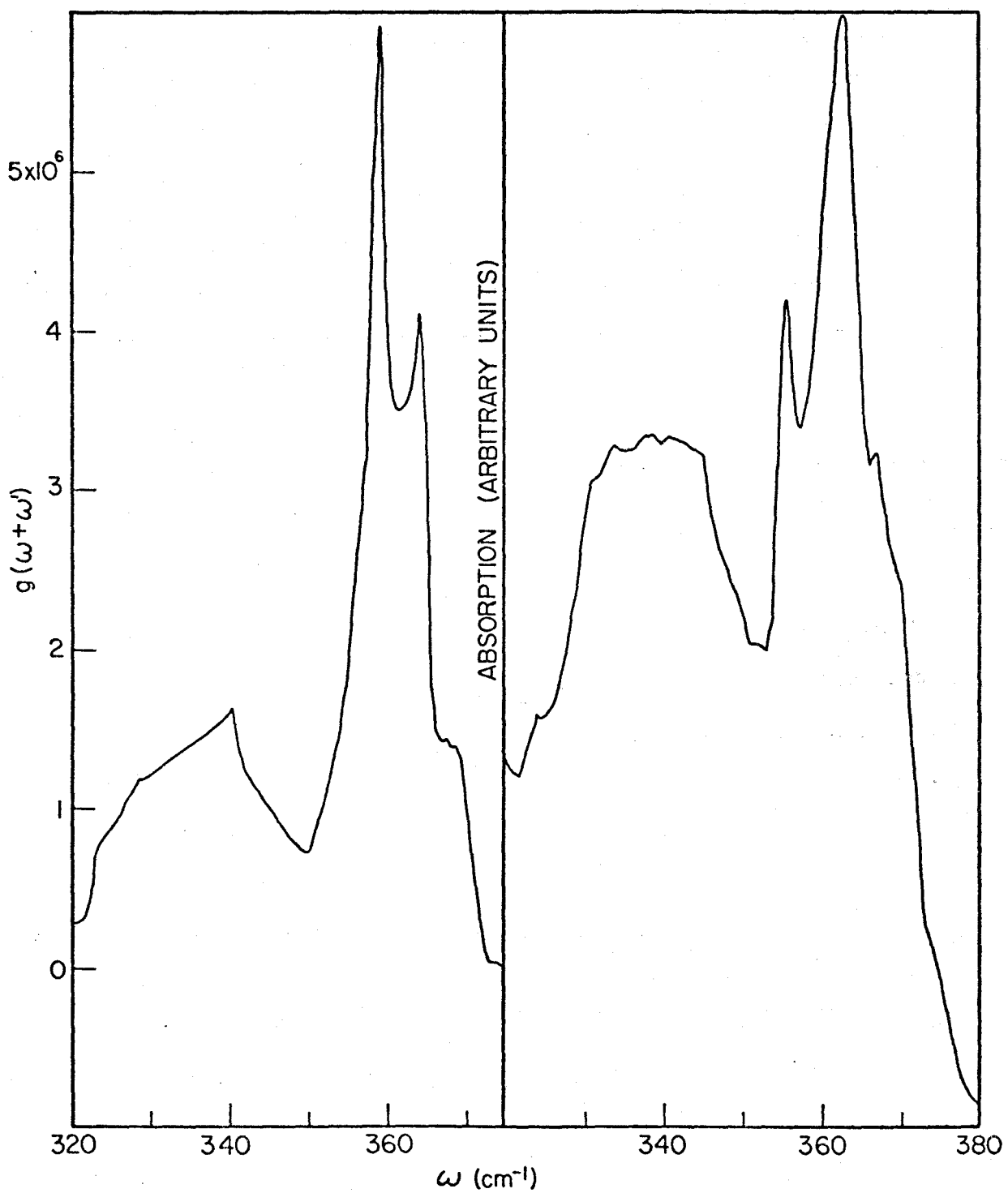
5x10^6
4
3
2
1
0
g(ω+ω')
ABSORPTION (ARBITRARY UNITS)
320
340
360
340
360
380
ω (cm^-1)

as an asymmetry of the main peak) as due to 2TO at L and the subsidiary peak at 355.5 cm^{-1} as due to 2TO at (.6,0,0). (.6,0,0) is a point in the [100] direction at which the LO and TO branches are degenerate and the TA branches exhibit a maximum. It is curious that this location in the zone produces so many prominent features in the two phonon spectrum (at 82.6 cm^{-1} (2TA), 218.6 cm^{-1} (TO+TA) and now 355.5 cm^{-1} (2TO)) although they are absent in the theoretical density of states. It would not be unexpected then if the TO-TA difference mode at this point made a strong contribution to the absorption - and it does (see the next section). This anomaly may be a consequence of the inadequate treatment of the optical modes by the theory. For this reason, in the identification of the critical points of 2TO overtones, more reliance is placed on the interpretation provided by studying the experimental dispersion curves than the theoretical critical point analysis. With this in mind, the shoulder at 375 cm^{-1} is attributed to 2TO modes at Γ and the weak broad peak at 384 to 388 cm^{-1} to TO+LO modes at and near Γ.

Table 4.6 contains a complete listing of these features and their assignments.

5 - Difference Modes

The most sensitive test of the theoretical calculation occurs when absorption bands due to differences processes are investigated. The theory survives this test relatively intact.

Table 4.6: Assignments of two-phonon summation processes in the region 320 to 390 cm^{-1}

Experimental Feature			Assignment		
				Critical point location	
position (cm^{-1})	shape	strength	combination	theory	experimental dispersion curves
320	P_2	weak	2LO	L	L
324	P_0+P_2	weak	2LO,2TO,TO+LO		(.4,0,0)
326	P_0	medium	$TO_{1,2}$+LO	W	(.8,.8,0)
344.8	P_2	medium	TO+LO	L	X,L
349	P_0+P_2	weak	2TO,2LO,TO+L)		(.4,0,0)
355.5	P_0+P_3	strong	optic overtone		(.6,0,0)
358.9	P_1	medium	2TO	X	L
362.7	$P_1+P_3+P_2$	strong	2TO	hexagonal face and L	X
367	P_1+P_2	medium	TO+LO	W	(.2,0,0)
370	P_1+P_2	weak	2TO	W and hexagonal face	
375	P_3	weak	2TO		Γ
381.5		weak			
385	P_3	weak	TO+LO		Γ
388		weak			

The very rapid increase of absorption with temperature for the difference bands is utilized to distinguish them from summation bands which are present in the same region of the spectrum (from zero up to the Reststrahl frequency). A spectrum at 78°K, in which the difference bands are already fairly strong is ratioed with one at 20°K in which they are essentially absent, to accentuate the bands rapidly increasing with temperature. The sum bands are not completely cancelled however as they do possess some temperature dependence.

The experimental two-phonon difference absorption spectrum and the calculated two-phonon difference density of states are presented in Figure 4.10. The principal feature, a strong, relatively sharp peak at 136 cm^{-1} results from a TO-TA difference mode at (.6,0,0). This is not predicted by theory. The weak subsidiary peaks on the high energy side of the 136 cm^{-1} absorption are due to TO-TA processes at the X(142.5 cm^{-1}) and L(146 cm^{-1}) points. These are predicted by the theory although in the calculated density of states they are merged into one peak at 141.5 cm^{-1}. The theoretical curve also predicts a peak at 127 cm^{-1} which is the result of a number of critical points in the TO-TA branches on or near the hexagonal face. This is observed as a low energy shoulder on the 136 cm^{-1} peak.

At much lower energies a sharp peak is present at 61.5 cm^{-1} which the critical point analysis indicates is due to

Figure 4.10: Calculated density of states for two-phonon difference processes compared with the observed absorption in an 1800 micron thick sample at 78°K in the frequency range 50 to 160 cm^{-1}. The spectrum was ratioed with one measured at 20°K in an attempt to cancel features due to summation processes.

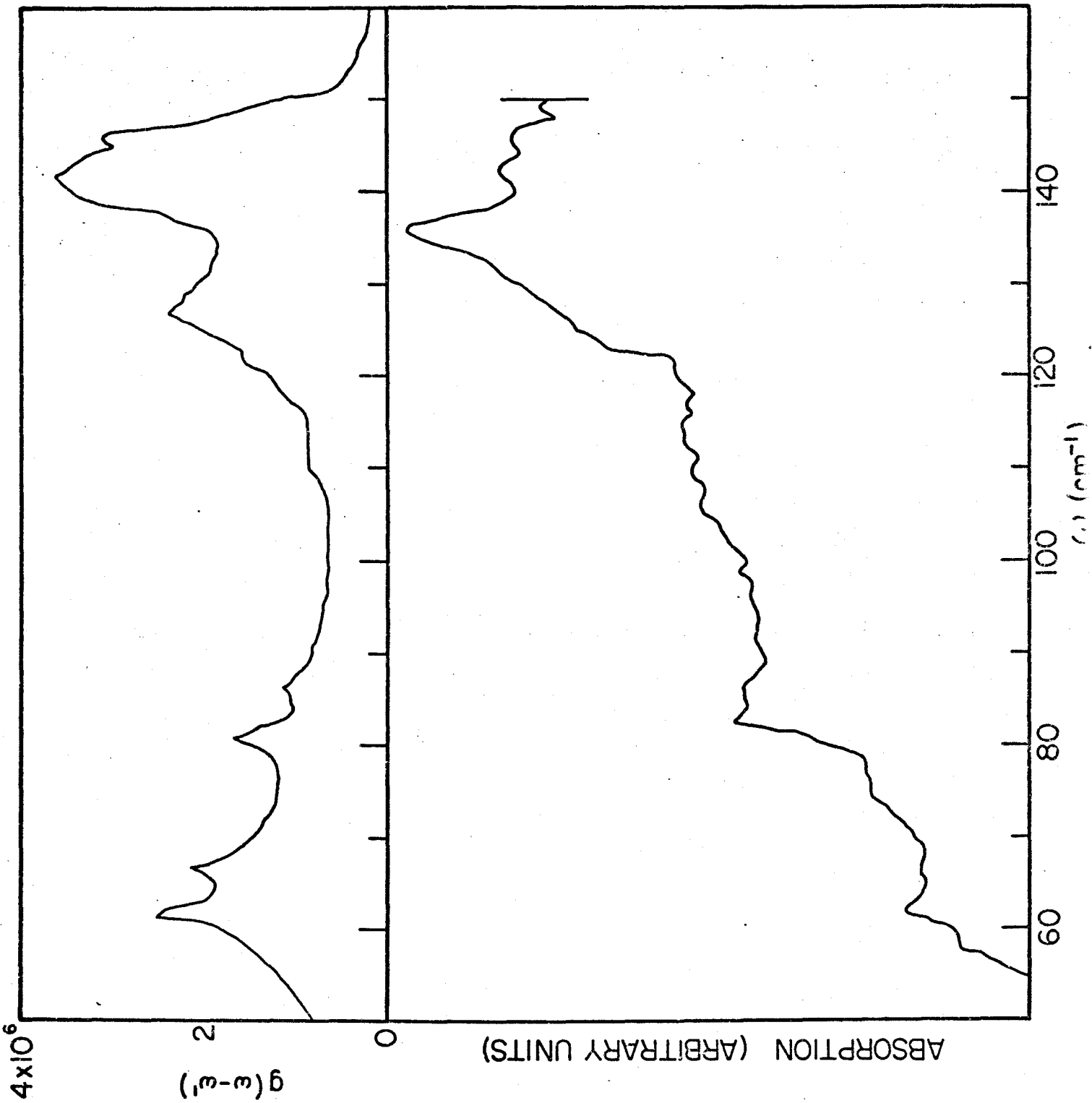
4x10^6
2
0
g(ω-ω')
ABSORPTION (ARBITRARY UNITS)
60
80
100
120
140

a sum of TO_2-LA and LA-TA_1 modes. The critical points for both of these processes are similar to the valley type on the hexagonal face described previously. For the TO_2-LA case however, instead of a valley a low circular mound is present on the (111) plane. There is a similar mound for the TO_1-LA mode and this produces a sharp peak in the difference density of states at 66.8 cm^{-1}. This is not observed in the absorption spectrum. However, if the assignment of the 2LA mode on the (111) plane is correct, then, using the known values of TO_1+LA and TO_2+LA on the hexagonal face, TO_1-LA and TO_2-LA become 59 cm^{-1} and 53 cm^{-1} respectively. The situation could be clarified by inelastic neutron scattering experiments performed in the Q direction.

Finally, the theory predicts relatively sharp but weak peaks near 81 and 86 cm^{-1} due to LA-TA_2 (due to critical points on the hexagonal face) and LO-TA_1 (due to critical points at K and W) modes respectively. This is a spectral region in which the sharp peak due to the 2TA mode at (.6,0,0) occurs and so these difference bands are difficult to observe unambiguously. However, judging from the temperature dependence of the absorption in this region it is likely that difference bands do underly the prominent summation peaks. Table 4.7 contains a summary of these results.

C. Summary

Having analysed the two-photon absorption spectra in some detail, it is now possible to draw general conclusions.

Table 4.7: Assignment of two-phonon difference processes in the region 50 to 170 cm^{-1}

Experimental Feature			Assignment		
				Critical point location	
position (cm^{-1})	shape	strength	Combination	theory	experimental dispersion curves
61.5	P_1+P_2	weak	$LA-TA_1$	hexagonal face	
82-83	P_1+P_2	weak	$LA-TA_2$	hexagonal face	
86	P_0+P_2	weak	$LO-TA_1$	K	K
122	P_0		$TO_{1,2}-TA_1$	K	(.6,.6,0)
127	P_1+P_2	medium	TO-TA	hexagonal face	
136	P_1+P_2	strong	TO-TA		(.6,0,0)
142.5	P_1+P_2	weak	TO-TA	X	X
146	P_1+P_2	weak	TO-TA	L	L

The overall shapes, positions and intensities of the two-phonon spectra agree well with the calculated two-phonon density of states curve. This confirms the initial assumption that the exact nature and frequency dependence of the photon-phonon coupling mechanism that makes possible the absorption has, in general, slight effect on the shape of the multi-phonon absorption bands. At the X and L points only phonon combinations involving transverse modes have critical points that lead to prominent peaks in the spectrum. The other strong features are attributable to critical points on the hexagonal face of the Brillouin zone and at (.6,0,0). This latter point is a location in the zone where the TO_1, TO_2 and LO lattice modes are simultaneously degenerate and the degenerate TA modes experience a maximum. It is easy to see then, why critical points at this location contribute so strongly but difficult to understand why the theory does not reflect this situation. Once more, it may be ascribed to the relatively poor theoretical treatment of the optic modes.

The absence of a strong absorption resulting from 2TA modes at the X and L points as predicted by the theory is more difficult to comprehend. It suggests a failing of the theoretical dispersion curves in off-symmetry axis directions (this hardly seems likely) or of the selection rules. Up to now the selection rules, or the frequency dependent coupling mechanism, have been ignored. Perhaps this is not possible in all cases. Then (since the selection rules derived from

group theory allow these interactions) the transition probability for the 2TA modes at X and L must be extremely small. This might also account for the weakness of the TO-TA modes at these same points but would not necessarily rule out strong TO+TA modes.

In general , then , the most prominent features of the two-phonon spectrum can be attributed to critical points in the Brillouin zone at (.6,0,0), X and L for phonon combinations incorporating only transverse modes and on the hexagonal face, the (111) plane, for two-phonon modes containing the longitudinal acoustic phonon. This latter observation confirms Borik's (1970) comments in a theoretical paper, on the significance of the hexagonal face for the distribution of combined phonon frequencies in GaAs.

It is ironic that early work on the interpretation of the multi-phonon spectra of III-V compound semi-conductors was more nearly correct than later, more detailed, analyses. In the case of InSb, Fray, Johnson and Jones (1960) first correlated the absorption peaks with only four phonon frequencies described as averages over the Brillouin zone boundary. This relatively crude picture agrees well with the detailed analysis outlined here. The position and the assignments of the absorption peaks are compared with those of the present work in Table 4.8. Later attempts were made to identify the fine structure of the spectrum with critical points at the symmetry points X and L without the benefit of experimental dispersion

Table 4.8: Comparison of the two-phonon assignments of Fray, Johnson and Jones and the present work

Fray et al (1960)		This work		
positions of features (cm^{-1})	Assignments	Assignments	Critical point location	Positions of features (cm^{-1})
360.5	2TO	2TO	X	362.7
336	TO+LA	TO+LO		330-345
297	TO+LA	TO_1+LA	hexagonal	305
		TO_2+LA	face	298.8
274	LO+LA	LO+LA	on and near hexagonal face	283.2
136	TO-TA	TO-TA	(.6,0,0)	136
85.5	2TA	2TA	(.6,0,0)	82.6

curves (Johnson, 1965; Stienwalt, 1966). These were much less successful as is evident in Table 4.9.

Utilizing the values of combination modes determined, from this analysis, to arise from critical points at X, L and (0.6,0,0) it is possible to derive explicit frequency values for some of the phonon modes at these points. These are presented in Table 4.10 along with the results of Price et al (1971) (inelastic neutron scattering), Johnson (1965) infrared absorption) and Stierwalt (1966)(infrared emission). The agreement between the values derived from this work and those measured directly by inelastic neutron scattering is good, especially when account is taken of the temperature shift of the absorption peaks.

Finally it should be mentioned that the general shapes of the two-phonon absorption spectra of other III-V compound semiconductors (such as GaAs and InAs) bear a striking resemblance to that of InSb. Thus it should be possible, using the analyzed InSb spectrum as a guide, to identify peaks in the multiphonon absorption spectra of these compounds with some confidence, even in the absence of experimental dispersion curves.

The general conclusion to be drawn from this experiment that is valid for other materials besides InSb is that interpreting multiphonon spectra in detail without the aid of experimental dispersion curves is an extremely risky undertaking.

Table 4.9: Comparison of two-phonon assignments by various workers

Previous work			This work	
Position of feature (cm^{-1})	Assignment		Position of feature (cm^{-1})	Assignments
	Johnson	Stierwalt		
83		2TA(X)	82.6	2TA(.6,0,0)
98		TO(Γ)-2TA(X)		
111		2TA(L)+TA(X)		
124		3TA(X)	124	$2TA_1$ (hexagonal face)
136	TO(L)-TA(L)	TO(L)-TA(L)	136	TO(.6,0,0)-TA(.6,0,0)
159		LA(W)+TA(W)	161	$LA+TA_2$ (hexagonal face
205		2LA(L)		
		TO(L)+TA(L)		
			213.5	TO(L)+TA(L)
			214.4	LO(.2,.2,.2)+TA(.2,.2,.2)
			218.6	TO(.6,0,0)+TA(.6,0,0)
			220	TO(X)+TA(X)
			246.2	2LA (hexagonal face)
273	2LA(L)		273.2	LO+LA (hexagonal face)
297	LO(L)+LA(L)		298.8	TO_2+LA (hexagonal face)
302	LO(X)+LA(X)		305	TO_1+LA (hexagonal face)
337	TO(X)+LO(X)		344.8	TO(L)+LO(L) TO(X)+LO(X)
353	2TO(X)		355.5	2TO(.6,0,0)
			358.9	2TO(L)
361	2TO(L)		362.7	2TO(X)
			375	2TO(Γ)
			385	TO(Γ)+LO(Γ)
400	LO(Γ)+TO(Γ)			
412	2LO(Γ)			

Table 4.10: Comparison of frequencies of phonon modes at X, L and (.6,0,0) determined by various workers

Location	Phonon mode	Price et al (1971) (300°K)	Johnson,1965 1.2-90°K	Stierwalt 1966 4.2-77°K	This Work (20°K)
X (1,0,0)	TO	179.5±5.7	176.6	176	181.4±.2
	LO	158.4±6.7	159.7	129	163.4±.2
	LA	143.4±3.3	142.8	121	
	TA	37.4±1.7		41.5	38.6±.2
L (.5,.5,.5)	TO	177.1±2.0	179.9	171	179.8±.2
	LO	160.8±3.3	160.5	160	165.0±.2
	LA	127.1±2.0	136.3	102	
	TA	32.7±1.7	43.6	34	33.8±.2
(.6,0,0)	TO	176.1±2.7			177.7±.5
	TA	40.0±1.3			41.3±.1

And, unless the dispersion curves include the Q direction, some assignments still may be in doubt. A good method for a detailed analysis is the one employed here for the first time in semiconductors. Theoretical density of state curves are compared with observed absorption spectra. If the agreement is satisfactory, a critical point analysis of the various multiphonon branches on the symmetry planes of the crystal may then be carried out. This reveals the locations in the Brillouin zone from which the principal features to the multiphonon absorption spectra arise.

iv - Temperature Dependence of Phonon Energies

The maximum frequency shift of the two-phonon modes was about a factor of three smaller than that experienced by the electron cyclotron mass over the same temperature range. That fact, together with the observation that many of the features of the two-phonon spectrum were weak or not very sharp, limited the number of two-phonon modes whose temperature dependence could accurately be determined.

The results for some of these features are given in Figure 4.11. The phonon frequencies have been normalized to the frequency measured at low temperature to facilitate comparison of the temperature dependences of different two-phonon modes. Also plotted on this diagram is the temperature dependence of the longitudinal optical mode at Γ.

The peculiarity of these curves is the fact that they all exhibit a similar behaviour with temperature. Even the

Figure 4.11: Frequencies of phonon features as a function of temperature. All are two-phonon modes with the exception of LO(Γ). The frequencies are normalized to the largest value measured.

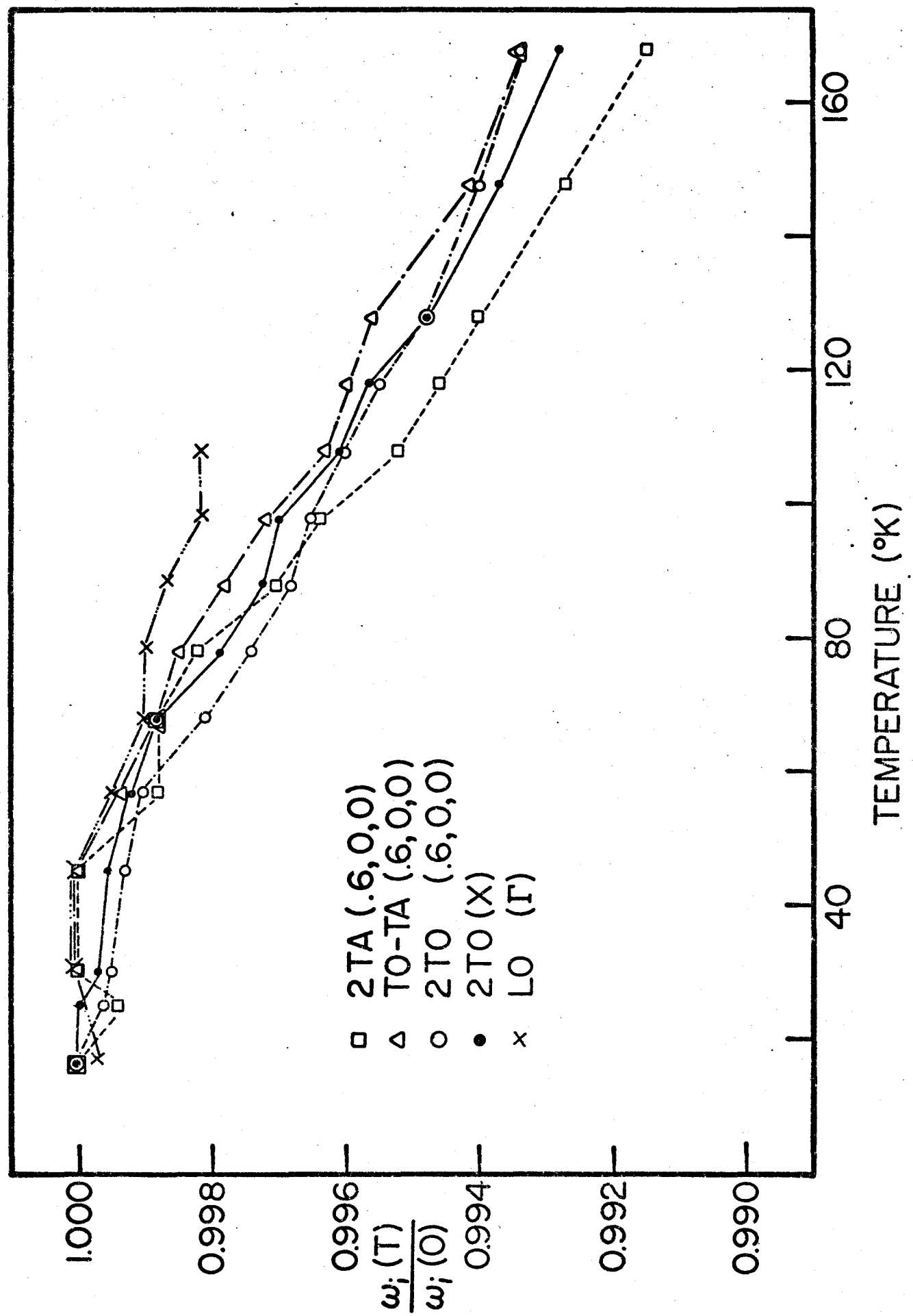
1.000
0.998
0.996
0.994
0.992
0.990
$\frac{\omega_i(T)}{\omega_i(0)}$
40
80
120
160
TEMPERATURE (°K)
2TA (.6,0,0)
TO-TA (.6,0,0)
2TO (.6,0,0)
2TO (X)
LO (Γ)

2TA mode, whose Grüneisen constant is expected to be negative, follows the general trend. Without a knowledge of the mode Grüneisen constants for these various lattice vibrations, it is impossible to proceed further. These have yet to be determined for InSb. Nevertheless relatively reliable estimates can be obtained for the Grüneisen constants of the optical modes. Mitra et al (1969) have measured these for the zone center optical modes in a number of semiconductors (not including InSb) by pressure dependent Raman scattering experiments. They concluded that γ_i for LO(Γ) is constant and equal to 1.0, within experimental limits, for all the materials tested. γ_i for TO(Γ) is larger than that for LO(Γ) and approximately a linear function of the effective charge per valence electron, e*. Using the known value of e* for InSb, γ_i for TO(Γ) is found to be approximately 1.2. It is also expected from theoretical studies, that the γ_i of the TO branches will not change much with the wavevector (Vetelino et al, 1970). Assuming then that the zone center γ_i for the TO mode is applicable to the zone edge, the anharmonic contribution to the frequency shift of TO(X) and LO(Γ) can be calculated using the procedure of Mitra (see, for example, Chang and Mitra, 1972). The observed frequency shift is expressed as

$$\Delta\omega_i^{obs}(T) = \omega_i(0) - \omega_i(T) \qquad (4.9)$$

$$= \Delta\omega_i^{vol}(T) + \Delta\omega_i^{anh}(T) \qquad (4.10)$$

where $\omega_i(0)$ and $\omega_i(T)$ refer to the observed TO or LO frequency

at O and T°K respectively. The terms in equation (4.10) are defined by

$$\Delta\omega_i^{vol}(T) = \omega_i(O) - \omega_i^{vol}(T) \qquad (4.11)$$

$$\Delta\omega_i^{anh}(T) = \omega_i(O) - \omega_i^{anh}(T) \qquad (4.12$$

$\omega_i^{vol}(T)$ can be calculated from equation (4.8) if γ_i and the linear coefficient of thermal expansion are known. Then from equations (4.11) and (4.10), $\Delta\omega_i^{anh}(T)$ can be obtained. This procedure was followed for TO(X) and LO(Γ) and $\Delta\omega_i^{obs}(T)$, $\Delta\omega_i^{vol}(T)$ and $\Delta\omega_i^{anh}(T)$ for these modes is shown in Figures 4.12 and 4.13 respectively.

The general behaviour of the anharmonicity component follows that reported by Mitra and co-workers for a number of materials ranging from highly ionic alkali halides to diamond. The fact that $\Delta\omega_i^{anh}(T)$ mirrors $\Delta\omega_i^{vol}(T)$ introduces some doubt as to the physical significance of this analysis. The change in sign of the anharmonic shift implies that at low temperatures the negative cubic term (decreasing frequency with increasing temperature) dominates whereas at higher temperatures the quadratic term becomes the most important. Moreover, the temperature dependence of the magnitude of these competing terms is such that their sum just cancels the anomalous temperature dependence (due to the volume coefficient of thermal expansion) of the dilation term to produce the smooth, virtually monotonic variation of frequency with temperature that is observed. This is difficult to understand. Obviously

Figure 4.12: Frequency shifts of TO(X) as a function of temperature. $\Delta\omega^{obs}(T)$ is the observed change in frequency; $\Delta\omega^{vol}(T)$ is the calculated frequency change due to lattice dilation; and $\Delta\omega^{anh}(T)$ is the difference between the first two terms and is called the anharmonic frequency shift.

$\Delta\omega^{obs}(T)$ - closed circles

$\Delta\omega^{vol}(T)$ - crosses

$\Delta\omega^{anh}(T)$ - triangles

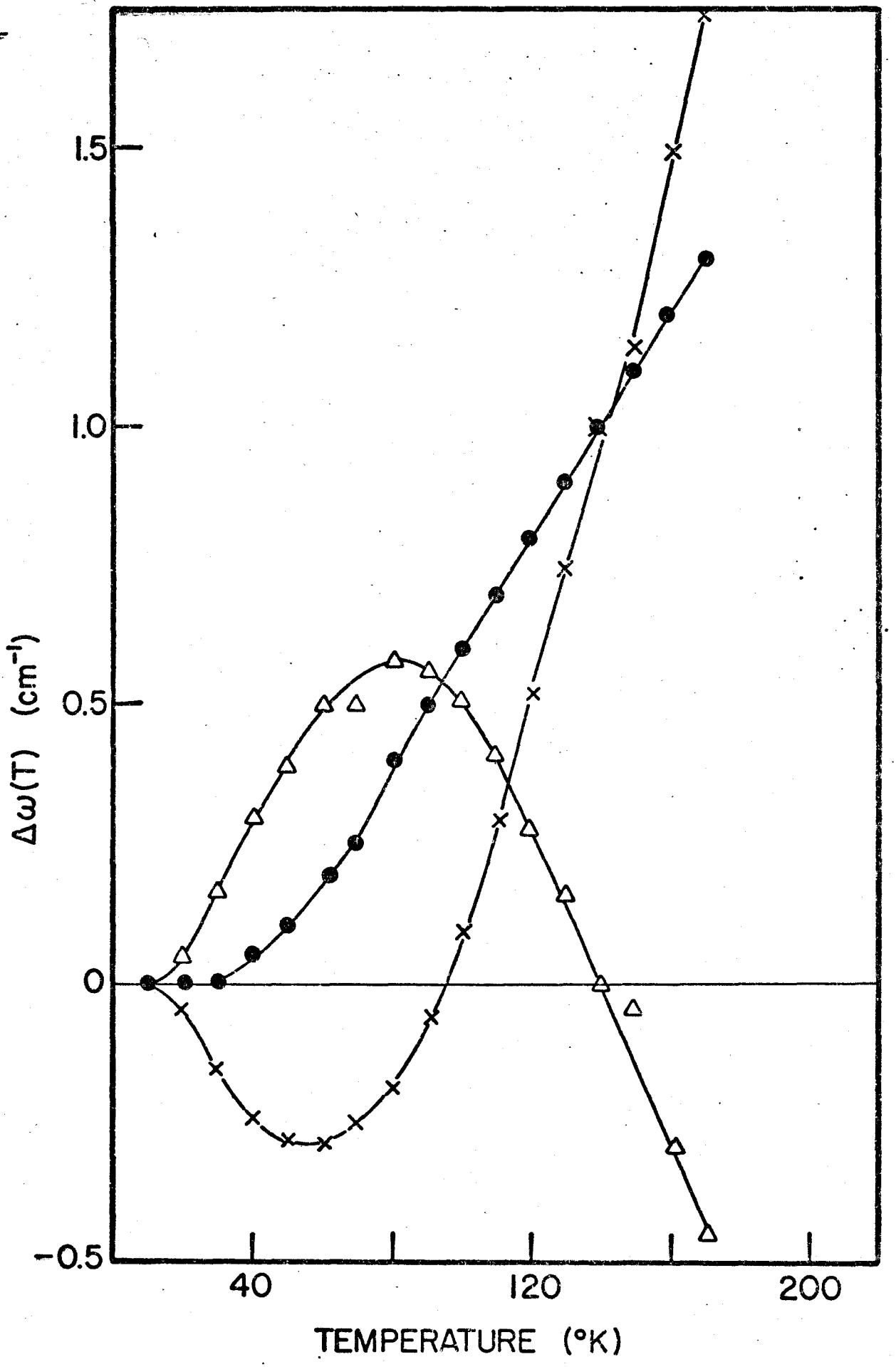
1.5
1.0
0.5
0
-0.5
Δω(T) (cm⁻¹)
40
120
200
TEMPERATURE (°K)

Figure 4.13: Frequency shifts of LO(Γ) as a function of temperature. $\Delta\omega^{obs}(T)$ is the observed change in frequency; $\Delta\omega^{vol}(T)$ is the calculated frequency change due to lattice dilation; and $\Delta\omega^{anh}(T)$ is the difference between the first two terms and is called the anharmonic frequency shift.

$\Delta\omega^{obs}(T)$ - closed circles

$\Delta\omega^{vol}(T)$ - crosses

$\Delta\omega^{anh}(T)$ - triangles

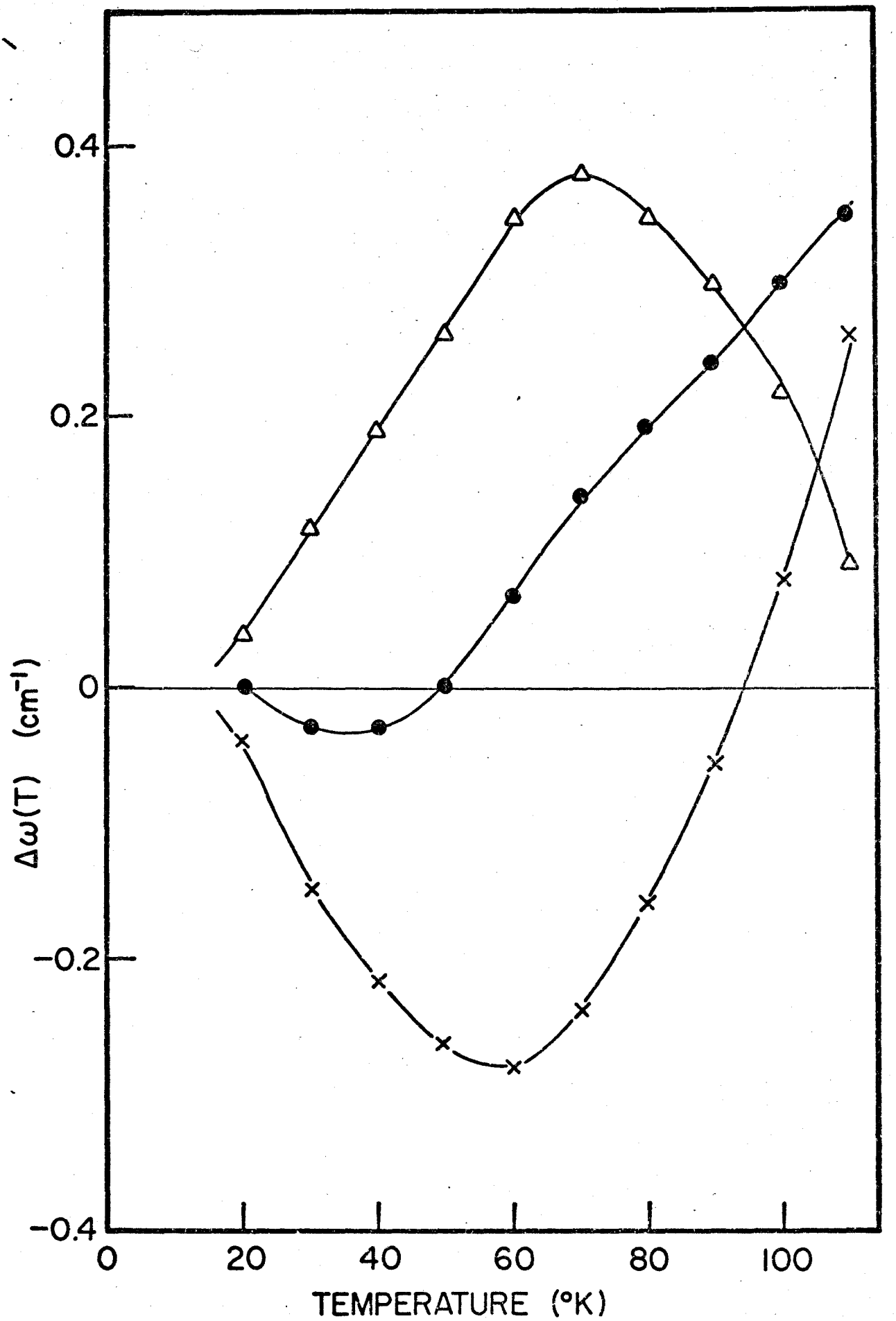
0.4
0.2
0
-0.2
-0.4
0
20
40
60
80
100
Δω(T) (cm⁻¹)
TEMPERATURE (°K)

this reflects the fact that the separation of the total energy shift into quasi-harmonic and anharmonic components is not complete since both terms can be related to the anharmonicity of the lattice potential. Thus the physical significance of the dilation and anharmonic terms is difficult to ascertain. More studies are necessary to clarify this situation. Especially interesting would be measurements of the mode Grüneisen constants, determined from pressure experiments, at a number of different temperatures.

It should be noted in passing that a study of the anharmonic behaviour of lattice vibrations in CuCl and CuBr, both of which possess anomalous thermal expansion at low temperatures, has produced results similar to those observed here (Plendl and Mansur, 1972). The anharmonicity factor, defined in a different way as the degree of asymmetry of the TO(Γ) mode was discovered, as a function of temperature, to mirror the thermal expansion.

CHAPTER V

CONCLUSIONS

A high-resolution far-infrared Fourier transform spectrometer system was developed and utilized to study absorption in the III-V compound semiconductor InSb. Optimization of the individual components in the system resulted in a quality factor of from 10^5 to 10^6 with the major noise attributable to arc fluctuations in the high pressure mercury lamp source.

The variation of the electron effective mass in InSb with magnetic field as determined by cyclotron resonance absorption experiments was compared with a theory originated by E. O. Kane (1957). Good agreement was found over the magnetic field range studied and more accurate values of the band edge effective mass ($m_o^* = 0.01383 \pm 0.00002\ m_e$) and the band edge effective g factor at 0°K ($g_o^* = -62 \pm 2$) were determined.

Resonant electron-LO phonon coupling between the $n = 2$ and the $n \cong 0 + \omega_{LO}$ Landau levels as a function of magnetic field was observed for the first time for free electrons in a semiconductor as a function of magnetic field. Comparison with theory permitted an accurate determination of the electron-LO phonon coupling constant in InSb. $\alpha = 0.023 \pm 0.001$ which is 15% larger than the value predicted by Frölich's theory. This

is in agreement with a result ($\alpha = 0.025 \pm .005$) obtained earlier using a different technique. The avoidance of the Reststrahl problem implicit in the present determination makes this method advantageous for the study of polaron effects in semiconductors.

The temperature dependence of the effective mass in InSb was studied employing cyclotron resonance absorption for the first time. The contention, by previous workers, that only the dilation of the crystal lattice affected the effective mass was confirmed although some discrepancy was found to exist between experiment and theory. The origin of the disagreement is speculative pending unambiguous pressure experiments or a higher order theory for electron-phonon interactions.

Far-infrared absorption attributable to single phonon and two-phonon processes was studied in InSb under high resolution . Single phonon absorption by the longitudinal-optical phonon mode at the center of the Brillouin zone was observed and its frequency (198.6 ± 0.1 cm^{-1} at 20°K) compared with other determinations. The agreement with inelastic neutron scattering data is good.

Two-phonon absorption spectra were compared with a two-phonon density of states calculation by G. Dolling (1972) which used parameters derived from inelastic neutron scattering experiments (Price et al, 1971). The overall agreement was very good. By investigating the phonon energy contours on symmetry planes the phonon combinations and their locations in

the Brillouin zone that give rise to the major features in the two-phonon density of states were identified. Combination modes at the high-symmetry points X and L are not responsible for all of these as previously suggested. Off symmetry axis locations on or near the Brillouin zone boundary produce many of the strong features. Such an analysis is possible for other semiconductors and indications are that it will lead to a similar result.

The frequency shift of many of the strong two-phonon features was investigated as a function of temperature. Analysis was accomplished by dividing the shift into two parts related to lattice dilation and anharmonic effects. The mirror relationship of these two processes complicates physical interpretation. More experimentation in the form of pressure experiments is required to interpret these results.

BIBLIOGRAPHY

Aggarwal, R. L., 1967, Bull. Amer. Phys. Soc. 12, 100.

Akselrod, M., Demchuk, K., Tsidilkovski, L., Broyda, E. and Radionov, K., 1968, Phys. Stat. Sol. 27, 249.

Anastassakis, E., Hwang, H. and Perry, C. 1971, Phys. Rev. B4, 2493.

Apel, J.R., Poehler, T. O., Westgate, C.R. and Joseph, R.I., 1971, Phys. Rev. B4, 436.

Bell, R.L. and Rogers, K.T., 1966, Phys. Rev. 152, 746.

Berreman, D., 1963, Phys. Rev. 130, 2193.

Birman, J., 1963, Phys. Rev. 131, 1489.

Blackman, M., 1958, Phil. Mag. 3, 831.

Borer, W., Mitra, S. and Namjoshi, K., 1971, Solid State Commun. 9, 1377.

Borik, H., 1970, Phys. Stat. Sol. 39, 145.

Bowers, R. and Yafet, Y., 1959, Phys. Rev. 115, 1165.

Bradley, C. and Gebbie, H., 1965, Phys. Lett. 16, 109.

Cano, R. and Mattioli, M. 1967, Infrared Phys. 7, 25.

Chang, I. and Mitra, S., 1972, Phys. Rev. B5, 4094.

Cooley, J.W. and Tukey, J.W., 1965, Mathematics of Computation 19, 296.

Connes, J. and Connes, P., 1966, J. Opt. Soc. Amer. 56, 896.

Cowley, E. and Cowley, R., 1965, Proc. Roy. Soc. A287, 259.

Daniels, W., 1962, Proc. Int. Conf. Phys. Semiconductors, Exeter, (The Institute of Physics and the Royal Society), London, p. 482.

Dickey, D.H., Johnson, E.J. and Larsen, D.M., 1967, Phys. Rev. Letters 18, 599.

Dolling, G., 1972, private communication.

Dolling, G. and Cowley, R.A., 1966, Proc. Phys. Soc. (London) 88, 463.

Douglas, R. and Timusk, T. 1970, private communication.

Dresselhaus, G., Kip, A.F. and Kittel, C., 1953, Phys. Rev. 92, 827.

Dresselhaus, G., Kip, A.F. and Kittel, C., 1955, Phys. Rev. 100, 618.

Ehrenreich, H., 1961, J. Appl. Phys. 32, suppl., 2155.

Fan , H., 1951, Phys. Rev. 82, 900.

Fellgett, P.B., 1951, thesis, University of Cambridge.

Fizeau, H., 1962, Ann. Chim. Phys. 66, 429.

Forman, M.J., Steel, W.H. and Vanasse, G.A., 1966, J. Opt. Soc. Amer. 56, 59.

Fray , S., Johnson, F.A. and Jones, R., 1960, Proc. Phys. Soc. (London) 76, 939.

Fröhlich, H., Pelzer, H. and Zienau, S., 1950, Phil. Mag. 41, 221.

Fröhlich, H., 1954, Advances in Physics, Vol. 3, (Taylor and Francis), London, p. 325.

Geick, R., 1965, Phys. Rev. 138, A1495.

Gibbons, D., 1958, Phys. Rev. 112, 136.

Gilat, G. and Dolling, G., 1964, Phys. Letters 8, 304.

Goldman, S., 1953, Information Theory (Prentice-Hall), New Jersey, p. 67.

Harper, P.G., Hodby, J.W. and Stradling, R.A., 1973, Reports on Progress in Physics 36, 1.

Hass, M. and Henvis, B., 1962, J. Phys. Chem. Solids 23,1099.

Isaacson, R.A., 1968, Phys. Rev. 169, 312.

Itskevich, E. and Sukhoparov, V., 1968, Sov. Phys. Solid State 10, 264.

Iwasa, S., Balslev, I. and Burstein, E., 1964, Physics of Semiconductors, Proc. of the Seventh Int. Conf., (Academic Press), New York, p. 1077.

Jacquinot, P. and Dufour, C., 1948, J. Rech. du Centre Mat. Rech. Sci. Lab., Bellevue (Paris) 6, 91.

Jacquinot, P., 1960, Rep. Prog. Phys. 23, 267.

Jacquinot, P. and Roizen Dossier, B., 1964, Progress in Optics, Vol. III ed. by E. Wolf, (North-Holland), Amsterdam, p. 31.

Jasperse, J., Kahan, A., Plendl, J. and Mitra, S., 1966, Phys. Rev. 146, 526.

Johnson, E.J., 1967, Solid State Research Report No. 4, Lincoln Laboratory, M.I.T., 33.

Johnson, E.J. and Dickey, D.H., 1970, Phys. Rev. B1, 2676.

Johnson, E.J. and Larsen, D.M., 1966, Phys. Rev. Letters 16, 655.

Johnson, F.A., 1965, Progress in Semiconductors, 9, 179.

Jones, R.C., 1953, J. Opt. Soc. Amer. 43, 1.

Kane, E.O., 1957, J. Phys. Chem. Solids 1, 249.

Keyes, R., 1955, Phys. Rev. 99, 490.

Kittel, C., 1968, Intro. to Solid State Physics, third edition, (John Wiley and Sons), New York, p. 277.

Kleinman, D., 1960, Phys. Rev. 118, 118.

Kolodziejczak, J., Zukotynski, S. and Stramska, H., 1966, Phys. Stat. Sol. 14, 471.

Konopka, J., 1970, Phys. Rev. Letters 24, 666.

Larsen, D.,1964, Phys. Rev. 135, A419

Larsen, D., 1966, Phys. Rev. 142, 428.

Lax, B., Mavroides, J.G., Zeiger, H.J. and Keyes, R.J., 1961, Phys. Rev. 122, 31.

Loewenstein, E., 1966, Appl. Opt. 5, 845.

Long, D., 1955, Phys. Rev. 99, 388.

Long, D., 1968, Energy Bands in Semiconductors , (Interscience), New York.

Lowndes, R., 1972, Phys. Rev. B6, 1490.

Mertz, L., 1967, Infrared Phys. 7, 17.

McCombe, B., 1969, Phys. Rev. 181, 1206.

McCombe, B.D. and Kaplan, R., 1968, Phys. Rev. Letters 21, 756.

McCombe, B. D. and Wagner, R.J., 1971, Phys. Rev. B4, 1285.

Michelson, A.A., 1891, Phil. Mag. 31, 256.

Mitra, S., 1969, Optical Properties of Solids, ed. by S. Nudelman and S. Mitra, (Plenum Press), New York, p. 388.

Mitra, S., Brafman, O., Daniels, W. and Crawford, R., 1969, Phys. Rev. 186, 942.

Mooradian, A. and Fan, H.Y., 1966, Phys. Rev. 148, 873.

Nakayama, M., 1969, J. Phys. Soc. Japan 27, 636.

Novikova, S., 1961, Sov. Phys. Solid State 2, 2087.

Palik, E.D., Picus, G.S., Teitler, S. and Wallis, R.F., 1961, Phys. Rev. 122, 475.

Payne, R., 1964, Phys. Rev. Letters 13, 53.

Phillips, J., 1956, Phys. Rev. 104, 1263.

Pidgeon, C.R. and Brown, R.N., 1966, Phys. Rev. 146, 575.

Pidgeon, C.R., Groves, S.H. and Feinleib, J.,1967, Solid State Commun. 5, 677.

Pidgeon, C.R., Mitchell, D.L. and Brown, R.W., 1967, Phys. Rev. 154, 737.

Pinczuk, A. and Burstein, E., 1968, Phys. Rev. Letters 21, 1073.

Plendl, J. and Mansur, L., 1972, Appl. Optics 11, 1195.

Postmus, C., Ferraro, J. and Mitra, S., 1968, Phys. Rev. 174, 983.

Price, D., Rowe, J., and Nicklow, R., 1971, Phys. Rev. B3, 1268.

Richards, P. L., 1964, J. Opt. Soc. Amer. 54, 1474.

Roberts, V. and Quarrington, J., 1955, J. Electron. 1, 152.

Rubens, H. and Wood, R.W., 1911, Phil. Mag. 21, 249.

Slater, J., 1939, Introduction to Chemical Physics (McGraw-Hill), New York, Chap. 13, Sec. 4.

Slutsky, L. and Garland, C., 1959, Phys. Rev. 113, 167.

Smith, S.D., Pidgeon, C.R., and Prosser, V., 1962, Proceedings of the International Conference on the Physics of Semiconductors Exeter, (The Institute of Physics and the Physical Society),

London, p. 301.

Sparks, P. and Swenson, C., 1967, Phys. Rev. 163, 779.

Spitzer, W., 1963, J. Appl. Phys. 34, 792.

Spitzer, W., 1967, Semiconductors and Semimetals, Vol. 3, (Academic Press), New York, Chap. 2.

Stierwalt, D., 1966, Proc. Int. Conf. Phys. Semiconductors, Kyoto, J. Phys. Soc. Japan 21, Suppl. pp. 58.

Stolen, R., 1969, Appl. Phys. Letters 15, 74.

Stradling, R. and Wood, R., 1970, J. Phys. C., Solid State Phys. 3, L94.

Summers, C.J., Dennis, R.B., Wherrett, B.S., Harper, P.G. and Smith, S.D., 1968, Phys. Rev. 170, 755.

Tumber, A., 1968, M. Sc. thesis, McMaster University.

Van Hove, L., 1953, Phys. Rev. 89, 1189.

Vetelino, J., Namjoshi, K. and Mitra, S., 1970, J. Appl. Phys. 41, 5141.

Wagner, V., 1965, Thesis, University of Freiburg, Germany.

Waldman, J., Larsen, D., Tannenwald, P., Bradley, C., Cohn, D. and Lax, B., 1969, Phys. Rev. Letters 23, 1033.

Yafet, Y.,1959, Phys. Rev. 115, 1172.

Ziman, J.M., 1960, Electrons and Phonons, (Clarendon Press), Oxford, Chapter 3.

Ziman, J.M. 1964, Principles of the Theory of Solids, (Cambridge University Press), Cambridge, p. 269.

Zwerdling, S., Smith, R.A., Theriault, J.P., 1968, Infrared Phys. 8, 271.

Zwerdling, S., Theriault, J.P. and Reichard, H.S., 1968, Infrared Phys. 8, 135.